

UC Santa Cruz

UC Santa Cruz Electronic Theses and Dissertations

Title

From Models to Management: Oceanographic Processes Shaping the Spatial Patterns and Progression of Ocean Acidification and Hypoxia in the California Current System

Permalink

<https://escholarship.org/uc/item/9r00154r>

Author

Cheresh, Julia

Publication Date

2023

Copyright Information

This work is made available under the terms of a Creative Commons Attribution License, available at <https://creativecommons.org/licenses/by/4.0/>

Peer reviewed|Thesis/dissertation

UNIVERSITY OF CALIFORNIA

SANTA CRUZ

**FROM MODELS TO MANAGEMENT: OCEANOGRAPHIC PROCESSES  
SHAPING THE SPATIAL PATTERNS AND PROGRESSSION OF OCEAN  
ACIDIFICATION AND HYPOXIA IN THE CALIFORNIA CURRENT  
SYSTEM**

A dissertation submitted in partial satisfaction

of the requirements for the degree of

DOCTOR OF PHILOSOPHY

in

OCEAN SCIENCES

with an emphasis in COASTAL SCIENCE AND POLICY

by

Julia Cheresh

December 2023

The Dissertation of Julia Cheresh is approved:

---

Professor Jerome Fiechter, chair

---

Professor Kristy Kroeker

---

Professor Chris Edwards

---

Steven Bograd, Ph.D.

---

Peter Biehl

Vice Provost and Dean of Graduate Studies

Copyright © by  
Julia Cheres  
2023

## Table of Contents

List of Tables .....	v
List of Figures .....	vi
Abstract .....	ix
Introduction.....	1
Acknowledgements.....	xi
Published material.....	xii
Chapter 1 - Physical and biogeochemical drivers of alongshore pH and oxygen variability in the California Current System.....	9
1.1 Abstract.....	9
1.2 Introduction.....	9
1.3 Methods.....	12
1.4 Results.....	15
1.5 Discussion.....	22
1.6 Acknowledgements.....	26
1.7 References.....	26
1.8 Supplementary information .....	34
Chapter 2 - Upwelling intensity and source water properties drive high interannual variability of corrosive events in the California Current .....	42
2.1 Abstract.....	42
2.2 Introduction.....	43
2.3 Methods.....	46
2.3.1 Model Configuration.....	46
2.3.2 Model evaluation .....	47
2.3.3 Event analysis .....	48
2.4 Results.....	50
2.4.1 Model Evaluation.....	50
2.4.2 Spatiotemporal variability of undersaturation events .....	54
2.4.3 Drivers of undersaturation events .....	59

2.5 Discussion.....	63
2.6 Acknowledgments.....	71
2.7 Data Availability Statement.....	71
2.8 References.....	72
2.9 Supplementary information .....	79
2.10 Supplementary References.....	88
Chapter 3 - Future evolution of OAH hot spots and refugia in the central California	
Current System.....	89
3.1 Abstract.....	89
3.2 Introduction.....	90
3.3 Methods.....	94
3.3.1 Coupled physical-biogeochemical model .....	94
3.2.2 Earth System Models .....	95
3.2.3 Analysis method.....	95
3.4 Results.....	97
3.5 Discussion.....	102
3.6 References.....	106
Chapter 4 - Development of an interactive web-based management tool for ocean acidification and hypoxia.....	
4.1 Introduction.....	113
4.2 Methods.....	114
4.2.1 Technical Development .....	114
4.2.2 OAH community engagement .....	115
4.3 Tool description .....	115
4.4 Incorporation of feedback from OAH community .....	123
4.4 Lessons learned.....	129
4.5 References.....	130
Conclusion .....	131

## List of Tables

Table S2.1. Summary of model-comparison statistics for the Taylor diagrams presented in Fig. 2.1.....	79
Table S2.2. Sensitivity analysis for aragonite saturation state.....	80
Table S2.3. Summary statistics of linear regressions.....	80
Table 3.1 $R^2$ values from regressions between climatological time of emergence ( $ToE_{clim}$ ) and 2000-2020 mean values, 2000-2020 standard deviation values, 2000-2100 trend values for surface and bottom pH and oxygen, and between threshold time of emergence ( $ToE_{thresh}$ ) and 2000-2020 mean values, 2000-2020 standard deviation values, 2000-2100 trend values for surface and bottom pH .....	102

## List of Figures

Figure 1.1 Spatiotemporal variability of simulated pH (top) and oxygen (mL/L) (bottom) at 10m depth in the central CCS during 1988-2010 .....	15
Figure 1.2 Simulated mean nearshore pH and oxygen, and their drivers, during peak upwelling season as a function of latitude for 1988-2010 .....	19
Figure 1.3 Simulated annual trends in nearshore pH and oxygen, and in their drivers, during peak upwelling season as a function of latitude for 1988-2010. ....	21
Figure 1.4 Processes controlling nearshore pH and oxygen in the central CCS.....	23
Figure S1.1 Map of in-situ observations used for model evaluation.....	34
Figure S1.2 Springtime simulated and observed climatological profiles of temperature, nitrate, chlorophyll, dissolved oxygen and pH along CalCOFI line 67..	35
Figure S1.3 Springtime simulated and observed climatological profiles of temperature, nitrate, chlorophyll, dissolved oxygen and pH along CalCOFI line 77..	36
Figure S1.4 Simulated and observed profiles of temperature, nitrate, pH and dissolved oxygen during May-Jun 2007 along WCOA Cruise transect near 42°N.....	37
Figure S1.5 Springtime simulated and observed climatological profiles of temperature, nitrate, pH and dissolved oxygen during May-Jun 2007 along WCOA Cruise transect near 40°N.....	38
Figure S1.6 Springtime simulated and observed climatological profiles of temperature, nitrate, pH and dissolved oxygen during May-Jun 2007 along WCOA Cruise transect near 38°N.....	39
Figure S1.7 Springtime simulated and observed climatological profiles of temperature, nitrate, pH and dissolved oxygen (mL/L) during May-Jun 2007 along WCOA Cruise transect near 36°N.....	40
Figure S1.8 Springtime simulated and observed climatological profiles of temperature, nitrate, pH and dissolved oxygen during May-Jun 2007 along WCOA Cruise transect near 34°N.....	41
Figure 2.1 Simulated and observed conditions during the 2007 WCOA Cruise .....	52

Figure 2.2 Simulated (1988-2010) and observed (2017-2019) pH at nearshore moorings .....	53
Figure 2.3 Simulated aragonite undersaturation ( $\Omega_{\text{arag}} < 1$ ) event properties during the upwelling season (May-September) along the bottom of the 100-m isobath. ....	55
Figure 2.4 Upwelling-season mean (black lines) and standard deviation (red dashed lines) of event properties and associated water mass characteristics during events (i.e. when $\Omega_{\text{arag}} < 1$ ).....	56
Figure 2.5 Relationships between event severity and water mass properties during undersaturated conditions ( $\Omega_{\text{arag}} < 1$ ) along the bottom of the 100-m isobath based on upwelling season means.....	58
Figure 2.6 Leading EOF mode of interannual variability for the DIC content and depth of $\sigma_{26}$ based on upwelling season averages and restricted to 0-200km offshore .....	60
Figure 2.7 Environmental conditions during periods of increased DIC content on $\sigma_{26}$ .....	62
Figure 2.8 Conceptual flow diagram of undersaturation ( $\Omega_{\text{arag}} < 1$ ) event severity and its drivers in the central California Current System.....	70
Figure S2.1. Simulated (1988-2010) and observed (2017-2019) dissolved oxygen and temperature at nearshore moorings.....	81
Figure S2.2. Simulated (1988-2010) and observed (2017-2019) intensity and duration of low pH events ( $\text{pH} < 7.7$ ).....	82
Figure S2.3. Climatological properties of undersaturation events ( $\Omega_{\text{arag}} < 1$ ).....	83
Figure S2.4. Fraction of the variability in $\Omega_{\text{arag}}$ attributed to changes in DIC, total alkalinity, temperature and salinity.....	84
Figure S2.5. Dissolved inorganic (DIC) and total alkalinity (TAlk) budget terms along the bottom of the 100m isobath.....	85
Figure S2.6. Mean depth (m) of 26.0 kg/m <sup>3</sup> isopycnal ( $\sigma_{26}$ ) on the 100m isobath during the upwelling season (May-Sept.).....	86
Figure S2.7. Top: Upwelling-season mean alkalinity and DIC <sub>REM</sub> . Upwelling-season mean alkalinity and DIC <sub>REM</sub> differences between positive and negative phases of the first EOF mode for DIC.....	87



Figure S2.8. Multiple linear regression model for event severity.....	88
Figure 3.1 Projected changes in temperature, pH, aragonite saturation state, and dissolved oxygen along the surface and bottom of the 100m isobath .....	97
Figure 3.2 Alongshore properties influencing climatological and threshold time of emergence ( $ToE_{clim}$ and $ToE_{thresh}$ ) for pH .....	100
Figure 3.3 Alongshore properties influencing climatological time of emergence ( $ToE_{clim}$ ) for dissolved oxygen .....	116
Figure 4.2 “OAH Change” tab.....	117
Figure 4.3 “Thresholds” tab in “isobath view”.....	119
Figure 4.4 “Thresholds” tab in “map view”.....	120
Figure 4.5 “Sanctuaries” tab .....	121
Figure 4.6 “Methods and data” tab. ....	122
Figure 4.7 Venn diagram summarizing feedback from OAH community .....	124
Figure 4.8 Changes made to “OAH Change” tab .....	125
Figure 4.9 Changes made to "Thresholds" tab .....	126
Figure 4.10 Changes made to “Sanctuaries” tab.....	128

## Abstract

From models to management: oceanographic processes shaping the progression of ocean acidification and hypoxia in the California Current System

by  
Julia Cheresch

The California Current System, situated off the US West Coast, experiences natural exposure to acidified and oxygen-poor conditions due to coastal upwelling, which brings low pH, low oxygen water from depth to the nearshore environment. The addition of anthropogenic ocean acidification and hypoxia (OAH) is therefore pushing conditions below biological thresholds, resulting in a variety of harmful effects ranging from behavior impacts to shell dissolution and mortality. It is therefore important to characterize the progression of ocean acidification and hypoxia in the California Current, where exposure to corrosive and hypoxic conditions is spatially variable and episodic in nature, making it a challenge to describe these patterns and their biophysical drivers through observational data alone. Here, a high resolution (~3 km) coupled physical-biogeochemical model is used to characterize the recent and projected spatial and temporal patterns in exposure to reduced pH and oxygen conditions, along with their physical and biogeochemical drivers. Results from Chapter 1 demonstrate that historical (1988-2010) alongshore variability in pH and oxygen is driven by a complex interplay of upwelling and primary production, modulated by the alongshore and cross-shore regional circulation. Results from Chapter 2 establish that historical variability in the interannual severity of exposure to

corrosive conditions is driven by combined changes in source water properties and upwelling intensity, respectively associated with decadal basin scale variability and interannual regional scale forcing. Chapters 3 and 4 utilize downscaled regional climate projections to investigate the future (2000-2100) progression of ocean acidification and hypoxia hot spots, the emergence of these features, and their implications for marine resource management. Results from Chapter 3 highlight that where and when hot spots and refugia for pH and oxygen emerge depends on the metrics used to quantify them. If one is managing for OAH and cares about where and when conditions become distinct from their historical range, the projections suggest hot spots will be located in areas of historically weaker upwelling due to their narrow range of variability. In contrast, if one is managing for OAH and cares about where and when conditions will drop below specific biological thresholds, the projections suggest hot spots will be located in areas of historically stronger upwelling due to their lower baseline pH and oxygen conditions. Chapter 4 synthesizes information from the projections and displays it in an online interactive management tool, where users can explore future OAH change based on their species or region of interest. As a whole, these four chapters provide the first comprehensive mechanistic description of the physical and biogeochemical drivers shaping historical and future alongshore and interannual OAH variability in the central California Current region, while disseminating this information to marine resource managers in an accessible format.

## Acknowledgements

I am deeply grateful for the mentorship of my advisor, Jerome Fiechter, who took me on as one of his first students and devoted countless hours and unquantifiable energy to ensuring my success as a graduate student. From teaching several of my first-year courses, to deciphering data and figures with me, helping me apply to fellowships, and going through slides in preparation for talks, Jerome has walked with me every step of the way. Thank you for enthusiastically supporting my ambitions, whether they be to add a designated emphasis in Coastal Science and Policy, or to take time off in the summer to climb and backpack. I am also grateful to my committee members Kristy Kroeker, Chris Edwards and Steven Bograd, who have offered valuable insight and guidance throughout my PhD, and have encouraged me in all my academic and career interests.

I would like to thank my office mates for sharing many laughs, snacks, pots of coffee and coding tips. Thank you to my fellow Ocean Sciences graduate students for enduring classes and exams as a team, for spending many days studying and collaborating together, and for the past 5 years of friendship.

To my parents, Linda and Matt, and my brother Elliott, thank you for your love and support, for teaching me at a young age to always cite my sources (even at the dinner table), and most of all for always believing in and cheering for me, no matter what I'm doing. Lastly, Spencer —thank you for your enduring faith in me, and for choosing to do life together.

- Julia

## Published material

This dissertation includes reprints of previously published work:

Cheresh, J., & Fiechter, J. (2020). Physical and Biogeochemical Drivers of Alongshore pH and Oxygen Variability in the California Current System.

*Geophysical Research Letters*, 47(19), e2020GL089553.

<https://doi.org/10.1029/2020GL089553>

Cheresh, J., Kroeker, K. J., & Fiechter, J. (2023). Upwelling intensity and source water properties drive high interannual variability of corrosive events in the California Current. *Scientific Reports*, 13(1), Article 1.

<https://doi.org/10.1038/s41598-023-39691-5>

The co-author Fiechter, J. listed in these publications supervised the research which forms the basis for this dissertation. The co-author Kroeker, K.J. provided observational data and reviewed the manuscript.

## Introduction

Ocean acidification and global oxygen decline are among the most concerning anthropogenic climate change-related threats to marine life. On average, surface ocean pH has dropped approximately 0.017-0.027 units per decade since the late 1980s, and oxygen has decreased by about 3-8% from 1000m to the surface between 1970 and 2010 (IPCC Special Report on the Ocean and Cryosphere in a Changing Climate, Ch. 5). In the California Current System (CCS), where environmental variability is dominated by upwelling, the impacts of ocean acidification and hypoxia (OAH) are particularly pronounced due to natural exposure to low pH and decreased oxygen water (Hauri et al., 2009). In the spring and summer months, alongshore winds drive upwelling, whereby deep, nutrient-rich water is delivered to the surface (Huyer, 1983; Jacox et al., 2014). This process fertilizes the sunlit waters, and supports highly productive food webs, making CCS ecosystems environmentally, economically, and culturally important. Upwelled water is also more corrosive and oxygen-poor, and the addition of anthropogenic ocean acidification and deoxygenation is already pushing conditions beyond biological thresholds of important species. Observed and projected reductions in pH and aragonite saturation state conditions resulting from anthropogenic ocean acidification may cause a variety of deleterious responses ranging from increased metabolic demands and shell dissolution, to mortality (Kroeker et al., 2013; Bednarsek et al., 2019; Bednarsek et al., 2020). These impacts can be difficult to quantify, given that tolerance thresholds are often species and life-stage specific. However, observations suggest that the

impacts of reduced pH and oxygen conditions have already begun impacting ecologically, commercially, and culturally important marine resources. Shell dissolution of pteropods — a holoplanktonic marine snail which plays an important role in pelagic food webs — has been documented in the CCS (Bednarsek et al., 2014). Damage to mechanoreceptors and carapace dissolution has also been observed in larvae of Dungeness Crab, one of California's most lucrative species (Bednarsek et al., 2020). Fish and crab die-offs have been recorded as the result of hypoxic events in nearshore rocky reef habitats off the coast of Oregon, and shoaling of the oxygen minimum zone is compressing viable habitat for forage fish (Gratham et al., 2004; Bograd et al., 2008; Howard et al., 2020). As anthropogenic climate change continues to unfold, it is important to understand how ocean acidification and hypoxia will progress in coastal CCS ecosystems.

The strength of upwelling, as well as its source water properties, exhibit high spatial and temporal variability (Feely et al., 2008; Chan et al., 2018). Coastline morphology influences atmospheric and oceanic circulation, and has been shown to shape the spatial pattern of biogeochemical properties such as phytoplankton biomass (Pickett and Paduan 2003; Kudela et al., 2008; Fiechter et al. 2018). Alongshore equatorward winds that drive upwelling will persist for days to weeks, followed by periods of relaxation, making exposure to corrosive and low-oxygen conditions intermittent in nature (Chan et al., 2018). Temporal variability in upwelling intensity and the biogeochemical properties of its source waters are additionally influenced by year-to-year variability in the strength of upwelling-favorable winds, along with

interannual and decadal modes of basin scale variability, such as the El Niño Southern Oscillation (ENSO) (Schwing et al., 2002; Jacox et al., 2015) , Pacific Decadal Oscillation (PDO) (Mantua et al., 2002; Chavez et al., 2003), and North Pacific Gyre Oscillation (NPGO) (Di Lorenzo et al., 2008; Chenillat et al., 2012).

Synoptic surveys and long-term stationary time series have shed light onto the spatiotemporal variability of pH and oxygen in the CCS. However, the complex dynamics influencing pH and oxygen, spanning scales of days to decades and capes to basin makes characterizing their drivers challenging from observations alone. Therefore, a mechanistic understanding of the oceanographic drivers of low pH and oxygen exposure at the spatial and temporal scales relevant to marine ecosystem management in the CCS is lacking to this day.

Here, a high-resolution coupled physical-biogeochemical model is employed to characterize the drivers of spatial and temporal variability in nearshore pH and oxygen along the central CCS. In Chapter 1, a model solution spanning 1988-2010 is used to characterize long-term mean spatial patterns of nearshore pH and oxygen, along with their drivers. The results demonstrate that pH and oxygen exhibit a heterogeneous alongshore pattern, expressed as a succession of minima and maxima corresponding to local enhancements in upwelling, primary production, and onshore geostrophic flow. This analysis serves as the first comprehensive mechanistic understanding of the drivers of spatial variability in pH and oxygen, and provides a historical baseline against which future change may be compared.



Chapter 2 focuses on corrosive events occurring on daily time scales, and the oceanographic drivers of the year-to-year variability in these events. The historical model simulation indicates that the majority of the variability in the severity of corrosive events can be explained by the combination of high-frequency (interannual) variability in the strength of upwelling-favorable winds, and low-frequency (decadal) variability in the dissolved inorganic carbon (DIC) content of upwelled source waters in response to changes in the subtropical gyre circulation. In general, high-severity events occur when average or above-average upwelling favorable wind stress coincide with higher dissolved inorganic carbon (DIC) content in upwelled source waters, but only for exceptionally strong upwelling-favorable wind stress during periods of lower DIC content.

Chapter 3 uses downscaled regional climate projections forced under the RCP8.5 high emissions scenario through the end of the 21st century to examine the future evolution of OAH by focusing on the “time of emergence” of pH and oxygen. The projections indicate that pH and oxygen both emerge from their historical ranges of variability soonest in locations with weak interannual variability, predominantly outside of upwelling centers, and within regions of elevated primary productivity. However, regions of enhanced upwelling historically experience exposure to more corrosive conditions due to the acidified content of upwelled water, making them the first to cross biologically-relevant thresholds.

Chapter 4 presents and describes the process of creating an online tool where users can explore OAH output from the downscaled projections for particular

biological thresholds and regions of interest. Targeted towards management, observing, and research sectors, the process of developing the online tool included meetings with members of the OAH community to gather feedback on user experience with the web interface and improve its relevance for real-world applications.

These four chapters provide a novel understanding of the physical and biogeochemical mechanisms responsible for the spatiotemporal variability of exposure to corrosive and low-oxygen conditions in the central CCS, and shed light on how these patterns relate to the future progression of OAH under anthropogenic climate change. To promote open access science and data sharing with stakeholders, this information was distilled and disseminated in the form of an interactive, management-focused online product. The findings from each chapter reinforce the notion that characterizing change in a highly dynamic system such as the CCS is not straightforward, and that the progression of OAH in the region and its impacts on coastal marine resources will depend on complex biophysical interactions occurring over a wide range of spatial and temporal scales.

## References

Bednaršek, N., Feely, R. A., Beck, M. W., Alin, S. R., Siedlecki, S. A., Calosi, P., Norton, E. L., Saenger, C., Štrus, J., Greeley, D., Nezlin, N. P., Roethler, M., & Spicer, J. I. (2020). Exoskeleton dissolution with mechanoreceptor damage in larval Dungeness crab related to severity of present-day ocean acidification

vertical gradients. *Science of The Total Environment*, 716, 136610.

<https://doi.org/10.1016/j.scitotenv.2020.136610>

Bednaršek, N., Feely, R. A., Reum, J. C. P., Peterson, B., Menkel, J., Alin, S. R., & Hales, B. (2014). *Limacina helicina* shell dissolution as an indicator of declining habitat suitability owing to ocean acidification in the California Current Ecosystem. *Proceedings of the Royal Society B: Biological Sciences*, 281(1785), 20140123. <https://doi.org/10.1098/rspb.2014.0123>

Bindoff, N.L., W.W.L. Cheung, J.G. Kairo, J. Arístegui, V.A. Guinder, R. Hallberg, N. Hilmi, N. Jiao, M.S. Karim, L. Levin, S. O'Donoghue, S.R. Purca Cuicapusa, B. Rinkevich, T. Suga, A. Tagliabue, and P. Williamson, 2019: Changing Ocean, Marine 20 Ecosystems, and Dependent Communities. In: IPCC Special Report on the Ocean and Cryosphere in a Changing Climate [H.-O. Pörtner, D.C. Roberts, V. Masson-Delmotte, P. Zhai, M. Tignor, E. Poloczanska, K. Mintenbeck, A. Alegría, M. Nicolai, A. Okem, J. Petzold, B. Rama, N.M. Weyer (eds.)].

Bograd, S. J., Castro, C. G., Di Lorenzo, E., Palacios, D. M., Bailey, H., Gilly, W., & Chavez, F. P. (2008). Oxygen declines and the shoaling of the hypoxic boundary in the California Current. *Geophysical Research Letters*, 35(12). <https://doi.org/10.1029/2008GL034185>

Chavez-Francisco, P., Ryan, J., Lluch-Cota, S. E. & Ñiquen, C. M. From anchovies to sardines and back: Multidecadal change in the Pacific Ocean. *Science* 299, 217–221 (2003).

- Chenillat, F., Rivière, P., Capet, X., Di Lorenzo, E. & Blanke, B. North Pacific Gyre Oscillation modulates seasonal timing and ecosystem functioning in the California Current upwelling system. *Geophys. Res. Lett.* 39, 15 (2012).
- Di Lorenzo, E. *et al.* North Pacific Gyre Oscillation links ocean climate and ecosystem change. *Geophys. Res. Lett.* 35, 8 (2008).
- Feely, R. A., Sabine, C. L., Hernandez-Ayon, J. M., Ianson, D., & Hales, B. (2008). Evidence for Upwelling of Corrosive “Acidified” Water onto the Continental Shelf. *Science*, 320(5882), 1490. <https://doi.org/10.1126/science.1155676>
- Fiechter, J., Edwards, C. A., & Moore, A. M. (2018). Wind, Circulation, and Topographic Effects on Alongshore Phytoplankton Variability in the California Current. *Geophysical Research Letters*, 45(7), 3238–3245. <https://doi.org/10.1002/2017GL076839>
- Grantham, B. A., Chan, F., Nielsen, K. J., Fox, D. S., Barth, J. A., Huyer, A., Lubchenco, J., & Menge, B. A. (2004). Upwelling-driven nearshore hypoxia signals ecosystem and oceanographic changes in the northeast Pacific. *Nature*, 429(6993), Article 6993. <https://doi.org/10.1038/nature02605>
- Jacox, M. G., Fiechter, J., Moore, A. M. & Edwards, C. A. ENSO and the California Current coastal upwelling response. *J. Geophys. Res.: Oceans* 120, 1691–1702 (2015).
- Kroeker, K. J., Kordas, R. L., Crim, R., Hendriks, I. E., Ramajo, L., Singh, G. S., Duarte, C. M., & Gattuso, J.-P. (2013). Impacts of ocean acidification on marine

organisms: Quantifying sensitivities and interaction with warming. *Global Change Biology*, 19(6), 1884–1896. <https://doi.org/10.1111/gcb.12179>

Mantua, N. J. & Hare, S. R. The Pacific decadal oscillation. *J. Oceanogr.* 58, 35–44 (2002).

Pickett, M. H., & Paduan, J. D. (2003). Ekman transport and pumping in the California Current based on the U.S. Navy's high-resolution atmospheric model (COAMPS). *Journal of Geophysical Research: Oceans*, 108(C10). <https://doi.org/10.1029/2003JC001902>

Schwing, F. B., Murphree, T., deWitt, L. & Green, P. M. The evolution of oceanic and atmospheric anomalies in the northeast Pacific during the El Niño and La Niña events of 1995–2001. *Prog. Oceanogr.* 54, 459–491 (2002).

## Chapter 1 - Physical and biogeochemical drivers of alongshore pH and oxygen variability in the California Current System

Julia Cheresch and Jerome Fiechter

### 1.1 Abstract

In the California Current System (CCS), the nearshore environment experiences natural exposure to low pH and reduced oxygen in response to coastal upwelling. Anthropogenic impacts further decrease pH and oxygen below biological thresholds, making the CCS particularly vulnerable to ocean acidification and hypoxia. Results from a coupled physical-biogeochemical model reveal a strongly heterogeneous alongshore pattern of nearshore pH and oxygen in the central CCS, both in their long-term means and trends. This spatial structuring is explained by an interplay between alongshore variability in local upwelling intensity and subsequent primary production, modulated by nearshore advection and regional geostrophic currents. The model solution suggests that the progression of ocean acidification and hypoxia will not be spatially homogeneous, thereby highlighting the need to consider sub-regional processes when assessing natural and anthropogenic impacts on coastal ecosystems in eastern boundary current upwelling regions.

### 1.2 Introduction

In the California Current System (CCS), several physical and biogeochemical processes control natural exposure to low pH and oxygen conditions on daily to seasonal time scales. In spring and summer, prevailing alongshore, equatorward winds drive coastal upwelling (Huyer 1983). As low pH, oxygen poor water is

introduced from depths between 50-100m to the surface via Ekman dynamics, wind-driven coastal upwelling is a dominant physical mechanism controlling nearshore pH and oxygen levels. High nutrient content in upwelled waters also supports new primary production, which acts as a biological regulator on pH and oxygen through photosynthesis and respiration. The addition of anthropogenic ocean acidification and oxygen decline to a system already experiencing low pH and oxygen exposure could push conditions below species-specific thresholds (Bograd et al. 2008; Hauri et al. 2013). Therefore, characterizing the past and present evolution of pH and oxygen levels at local and regional scales is key to understanding how anthropogenic impacts are emerging against natural signals in the CCS.

While seasonal upwelling acts as a dominant control on environmental variability along most of the west coast of the United States, upwelling intensity and ecosystem responses are not spatially homogeneous. Atmospheric fields and ocean circulation are affected by coastline morphology (Barth et al. 2000; Pickett and Paduan 2003), and biogeochemical variability has been similarly linked to topographic features locally modulating upwelling intensity and coastal currents (Kudela et al. 2008; Fiechter et al. 2018). Alongshore heterogeneity in coastal upwelling and subsequent biogeochemical response is supported by CCS-wide shipboard surveys and nearshore time series, documenting a spatial pattern of low pH exposure, with local "hotspots" near topographic features (Feely et al. 2007; Chan et al. 2018). Since pH and oxygen typically covary (Baumann and Smith 2017), low-oxygen exposure likely exhibits a similar nearshore spatial pattern. However,

observations characterizing the long-term response of pH and oxygen to local physical and biogeochemical drivers in the central CCS are limited, as routine sampling occurs primarily south of Pt. Conception ( $\sim 34.5^\circ\text{N}$ ). Thus, the finer scale nature of pH and oxygen variability along the entirety of the central California Current ( $35\text{-}43^\circ\text{N}$ ) has yet to be fully documented and mechanistically explained.

Coupled physical-biogeochemical models yield insight into the mechanisms shaping alongshore variability at spatiotemporal scales that observational studies cannot concurrently resolve. Existing modeling studies for the CCS have provided important knowledge about processes controlling pH and oxygen variability, and the predictability of their seasonal, interannual and long-term evolution (Gruber et al. 2012; Hauri et al. 2013a,b; Siedlecki et al. 2015, 2016; Dussin et al. 2019; Brady et al. 2020; Howard et al. 2020). Many of these studies focused on regional and basin-scale mechanisms influencing ocean acidification and hypoxia, obscuring pH and oxygen variability at finer alongshore scales (10-100km) over which processes modulating these variables (e.g., upwelling intensity, nutrient transport, and primary production) are known to vary in the central CCS (Fiechter et al. 2018).

The present work expands on earlier modeling studies by using a coupled physical-biogeochemical model at  $1/30^\circ$  ( $\sim 3$  km) resolution and benefiting from data assimilation to characterize alongshore pH and oxygen patterns, and their drivers, in the central CCS. More specifically, the analysis examines how localized enhancements in upwelling intensity and phytoplankton biomass described by Fiechter et al. (2018) shape alongshore means and trends for pH and oxygen during



1988-2010. As such, the results contextualize the relative importance of natural pH and oxygen variability, and its potential impact on local and regional ecosystem resources, in a largely undersampled region of the CCS.

### 1.3 Methods

The physical circulation for the CCS is generated using a nested implementation of the Regional Ocean Modeling System (ROMS) (Shchepetkin and McWilliams 2005; Haidvogel et al. 2008). The model consists of an outer domain at  $1/10^\circ$  ( $\sim 10\text{km}$ ) resolution from  $30^\circ\text{N}$  to  $48^\circ\text{N}$  benefiting from physical data assimilation, and a downscaled inner domain at  $1/30^\circ$  ( $\sim 3\text{km}$ ) resolution from  $32^\circ\text{N}$  to  $44^\circ\text{N}$ . The physical model is forced at the surface with the  $0.25^\circ$  resolution Cross-Calibrated Multi-Platform (CCMP) winds of Atlas et al. (2011), and the initial and boundary conditions for the outer CCS domain are derived from the Simple Ocean Data Assimilation (SODA) reanalysis of Carton et al. (2000). Details of the downscaling method can be found in Fiechter et al. (2018).

The biogeochemical model, NEMUCSC, is a customized version of the North Pacific Ecosystem Model for Understanding Regional Oceanography (NEMURO) (Kishi et al. 2007). NEMUCSC consists of three limiting macronutrients (nitrate, ammonium, and silicic acid), two phytoplankton size-classes (nanophytoplankton and diatoms), three zooplankton size-classes (microzooplankton, mesozooplankton, and predatory zooplankton), and three detritus pools (dissolved and particulate organic nitrogen and particulate silica). NEMUCSC also incorporates carbon and oxygen cycling based on the formulations of Hauri et al. (2013) and Fennel et al. (2013),

respectively. The carbon submodel includes dissolved inorganic carbon (DIC), total alkalinity and calcium carbonate; with ocean pH and pCO<sub>2</sub> calculated from the OCMIP carbonate chemistry described in co2calc\_SWS.f (<http://ocmip5.ipsl.jussieu.fr>). Atmospheric pCO<sub>2</sub> is based on the Mauna Loa time series and consists of a mean seasonal cycle superimposed with an annual increase of 1.5 ppmv before 1995 and 2 ppmv thereafter. In the model, DIC is decreased by primary production and calcium carbonate formation, and increased by respiration, remineralization and calcium carbonate dissolution; alkalinity is decrease by nitrification and calcium carbonate formation, and increased by new primary production (nitrate removal) and calcium carbonate dissolution; oxygen is decreased by nitrification and remineralization, and increased by primary production. Initial and boundary conditions for the outer domain are derived from the monthly World Ocean Atlas climatology (Conkright and Boyer, 2002) for nutrients and oxygen, from the Global Ocean Data Analysis Project (Key et al., 2004) for total alkalinity, and from the empirical relationship of Alin et al. (2012) for DIC using monthly temperature and oxygen. The empirical relationship is preferred over the GLODAP annual mean as it improves initial and boundary conditions for mid-depth (100-200m) DIC concentrations in the central CCS.

While the simulation encompasses 1980-2010, the analysis is limited to 1988-2010 to remove spin-up effects and concentrate on the period when the model is forced by the higher resolution CCMP winds. The results focus on the central CCS region (35-43°N), known to exhibit strong alongshore physical and biogeochemical

variability (Fiechter et al. 2018), to demonstrate the impacts of local upwelling intensification, primary production and coastal currents on nearshore pH and oxygen. “Nearshore” variables are defined here as zonal averages from the coast to 30 km offshore, which represents a natural scaling distance for coastal upwelling in the central CCS based on the internal Rossby radius of deformation (as evidenced by the synoptic pH and oxygen maps in Fig. 1.1, left panels). A 30 km alongshore running mean is applied to the variables to remove patchiness associated with topographic variations at scales smaller than ~10 km, which are more challenging to interpret and would detract from the analysis. Since the lowest nearshore pH and oxygen levels occur during the upwelling season, the analysis also concentrates on values averaged annually over a 4-month period coinciding with the peak magnitude of upwelling-favorable alongshore winds in the model (May to Aug for 35-40°N and Jun to Sep for 40-43°N) (Fig. 1.1, center panels). Based on monthly mean values, upwelling season extremes for 1988-2010 range from 0.1-0.2 for pH and 0.4-0.8 mL/L for oxygen depending on latitude (Fig. 1.1, right panels).

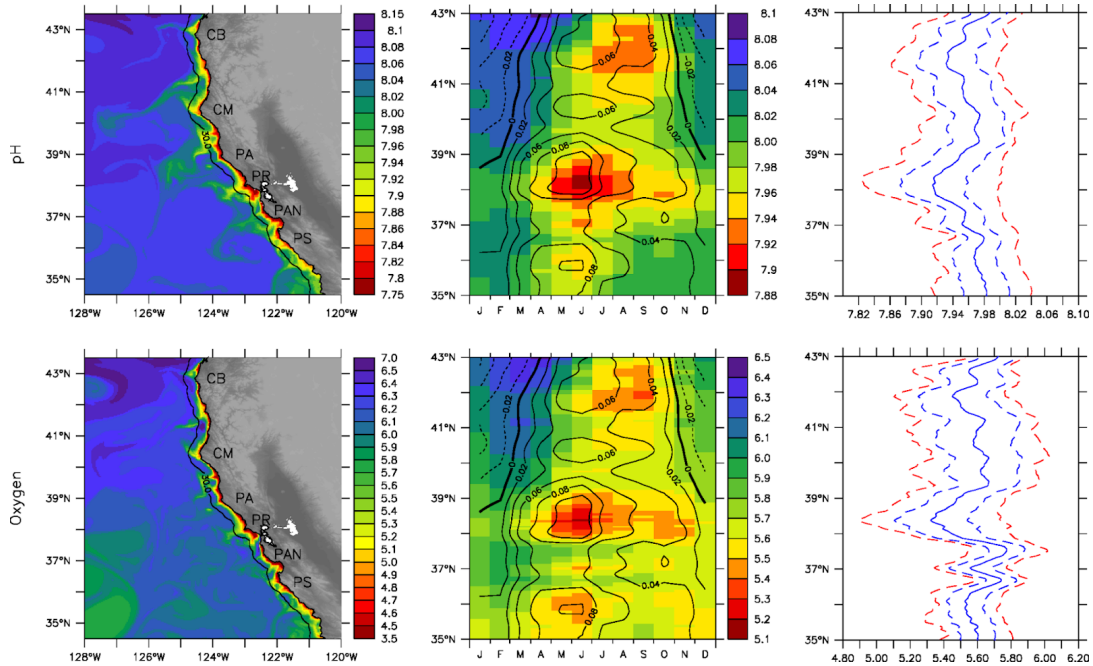


Figure 1.1 Spatiotemporal variability of simulated pH (top) and oxygen (mL/L) (bottom) at 10m depth in the central CCS during 1988-2010. Left: Synoptic maps for 16 May 2007 with 30km offshore distance (black contour) and locations of major coastal topographic features (PS = Pt. Sur, PAN = Pt. Año Nuevo, PR = Pt. Reyes, PA = Pt. Arena, CM = Cape Mendocino, CB = Cape Blanco). Center: Hovmöller diagram for nearshore climatological means; black contours represent climatological alongshore wind stress ( $N/m^2$ ) (positive equatorward) highlighting peak upwelling season at each latitude. Right: Upwelling season nearshore mean (solid blue line)  $\pm$  one standard deviation (dashed blue lines) and extreme values (dashed red lines) across years as a function of latitude. “Nearshore” indicates 0-30 km offshore average.

## 1.4 Results

In addition to existing evaluations of the  $1/10^\circ$  and  $1/30^\circ$  model solutions (temperature, salinity and density structure in Schreoder et al. (2014); coastal circulation in Fiechter et al. (2018); surface  $pCO_2$  and chlorophyll in Fiechter et al. (2014, 2018); krill abundance in Fiechter et al. (2020)), the model solution is compared against climatological (California Cooperative Oceanic Fisheries Investigations (CalCOFI) lines 67 and 77) and synoptic (NOAA’s 2007 West Coast Ocean Acidification (WCOA) cruise) observations to determine its ability to

reproduce physical and biogeochemical properties at various latitudes during the upwelling season (Fig. S.1.1). Observed springtime profiles along lines 67 and 77 generally fall within one standard deviation of the model mean (Appendix I, Supp. Figs. 1.2-1.3), with the largest discrepancies occurring for chlorophyll (which may partly result from fixed C:Chl used to convert diatom (C:Chl = 50) and nanophytoplankton (C:Chl = 100) concentrations in nitrogen units to chlorophyll). While reproducing synoptic values is typically more challenging, in situ measurements from the WCOA cruise at five transect locations between 34 and 42°N generally fall within or close to the range of simulated daily means during the cruise period (May-Jun 2007), although certain nearshore stations exhibit larger discrepancies (Figs S1.4-S1.8).

Model-data correlations for temperature, nitrate, DIC, pH, and oxygen along each transect line are greater than 0.9 for climatological values and 0.75-0.95 for synoptic values. Simulated fields also exhibit similar variability as in situ measurements (standard deviation ratios between 0.75 and 1.25), resulting in root mean square errors of 0.25-0.5 times the observed standard deviations for climatological profiles and 0.5-0.75 times the observed standard deviations for synoptic profiles (Fig. S1.9). Since locations with the largest errors for biogeochemical variables also exhibit the largest errors for temperature (e.g., WCOA transects near 36 and 38°N), model-data discrepancies are presumably caused by misrepresentation of local physical processes at synoptic scales (e.g., timing and magnitude of upwelling). This interpretation is reinforced by the fact that the lowest

errors for all climatological variables occur along CalCOFI line 67, which overlaps with the WCOA transect near 36°N. Pinpointing the exact nature of synoptic discrepancies is difficult due to the scarcity of additional supporting observations (especially at nearshore stations).

The most striking feature in the model solution is the strong alongshore variability in mean nearshore pH and oxygen levels at 10m depth (Fig. 1.2a). The simulation identifies successive coastal regions exhibiting lower (near 36°N, 38.5°N, and 42.2°N) and higher (near 35.3°N, 36.6°N, 37.5°N, 39.7°N, 41°N) pH and oxygen in response to alongshore variations in upwelling intensity, primary production and regional circulation patterns. Mean nearshore pH values range from 7.91-7.93 near minima to ~7.98 near maxima, while mean nearshore oxygen values range from 5.3-5.55 mL/L near minima to 5.7-5.8 mL/L near maxima. The meridional averages (35-43°N) are ~7.95 for pH and ~5.56 mL/L for oxygen.

Coastal regions exhibiting reduced pH and oxygen occur directly equatorward of enhanced upwelling centers, as indicated by strongly positive vertical DIC flux at 40m depth (purple shading in Fig. 1.2a, b) and elevated DIC concentrations at 10m depth (Fig. 1.2b). The latitudinal shift between vertical flux maxima and pH and oxygen minima is attributed to the alongshore circulation (arrows in Fig. 1.2b). For the two regions of enhanced upwelling near Pt Arena (~38.5°N) and Cape Blanco (~42°N), alongshore currents are strongly equatorward, resulting in pH and oxygen minima expressed ~50 km to the south of vertical DIC flux maxima. Similarly, the combination of alongshore advection and time-dependence of nutrient uptake and

growth by phytoplankton leads to maxima in net primary production shifted by 50-100 km from enhanced upwelling centers. For the regions of intensified upwelling near Pt Arena and Cape Blanco, primary production maxima occur equatorward of vertical DIC flux maxima, near 37.5°N and 41°N, respectively. Since nutrient uptake and photosynthesis by phytoplankton reduce DIC and increase oxygen, pH and oxygen maxima are collocated with regions of enhanced primary production (primary production is the dominant contributor to simulated changes in DIC, alkalinity, and oxygen (Fig. S1.10)). For the region of enhanced upwelling near Pt Sur (~36°N), alongshore currents are weakly poleward, leading to a slight northward shift of the net primary production maximum and pH and oxygen minima relative to the vertical DIC flux maximum.

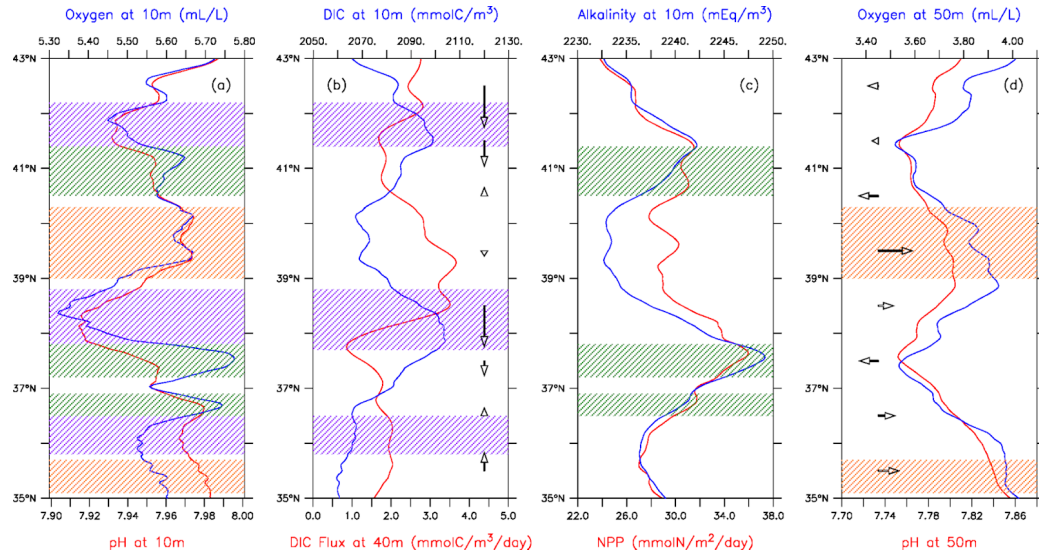


Figure 1.2 Simulated mean nearshore pH and oxygen, and their drivers, during peak upwelling season as a function of latitude for 1988-2010. (a) Mean pH (red) and oxygen (blue) at 10m depth. (b) Mean vertical DIC flux at 40m depth (red) and DIC concentration at 10m depth (blue); arrows indicate direction and magnitude of mean alongshore velocities at 20m depth (downward pointing denotes equatorward flow). (c) Mean depth-integrated net primary production (red) and alkalinity at 10m depth (blue). (d) Mean pH (red) and oxygen (blue) at 50m depth; arrows indicate direction and magnitude of mean geostrophic velocities (right pointing denotes onshore flow). Purple shading indicates pH and oxygen minima associated with enhanced upwelling. Green shading indicates pH and oxygen maxima associated with enhanced primary production. Orange shading indicates elevated pH and oxygen associated with onshore geostrophic flow. All variables represent 0-30km offshore averages, except for onshore geostrophic velocity which is the value at 100km offshore.

Areas of elevated pH and oxygen levels also occur around 35.1-35.6°N and 39-40.2°N where strong onshore geostrophic flow occurs (arrows in Fig. 1.2d), which opposes offshore Ekman transport and reduces coastal upwelling efficiency. Consequently, regions of strong onshore flow exhibit higher pH and oxygen values at 50m depth relative to neighboring shelf regions, due to reduced uplifting of the density and nutrient structures (Fig. 1.2d). Since upwelled waters in the central CCS originate between 50-60m (Jacox et al., 2015), increasing pH and oxygen in source waters would explain higher values at 10m depth. The moderate primary production



peak around 39.5°N further contributes to elevating pH and oxygen at 10m depth in that region.

Simulated pH and oxygen trends also exhibit substantial alongshore variability, and are similarly explained by trends in coastal upwelling intensity and phytoplankton biomass (trends are more clearly interpreted from state variables as biogeochemical rates are affected by the temperature trend). During 1988-2010, coastal upwelling intensified region-wide, and particularly near enhanced upwelling centers, as evidenced by the strongly positive trends in vertical velocity at 40m depth (Fig. 1.3b). This intensification leads to relatively more negative (or less positive) trends in nearshore pH and oxygen downstream of enhanced upwelling centers (purple shading in Fig. 1.3). The largest negative trends for nearshore pH and oxygen occur near 36.3°N and 38°N, with annual values around -0.0025/yr and -0.004 mL/L/yr, respectively (cumulative changes of about -0.06 and -0.092 mL/L over the 23-year period). Upwelling intensification also explains regions of increasing phytoplankton biomass further downstream, locally resulting in more positive (or less negative) trends in nearshore pH and oxygen (green shading in Fig. 1.3). Furthermore, trends in phytoplankton biomass appear to influence oxygen trends more strongly than pH trends, especially for the maximum near 37.5°N. The largest positive trends for nearshore pH and oxygen occur near 41.5°N, with annual values around 0.001 and 0.016 mL/L, respectively (cumulative changes of about 0.023 and 0.37 mL/L over the 23-year period).

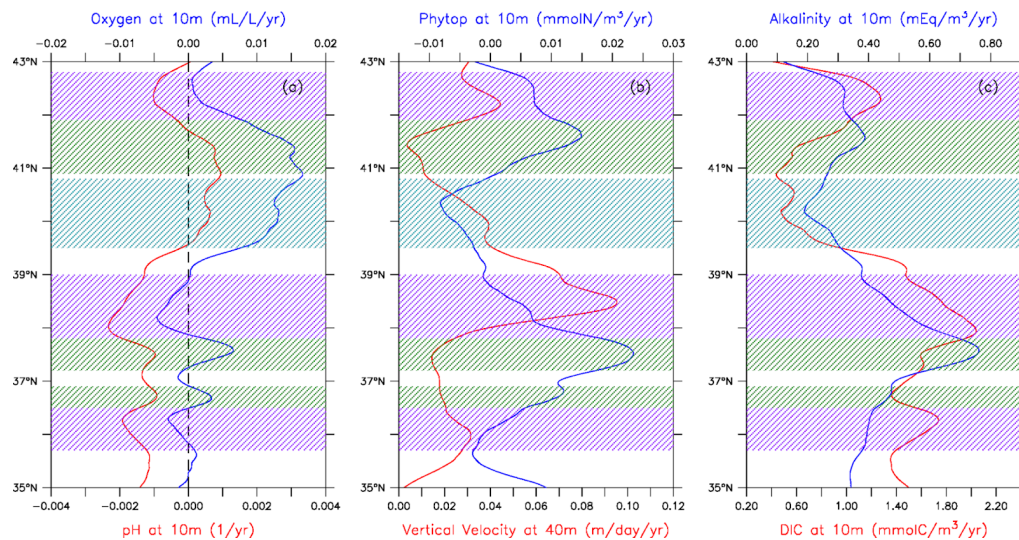


Figure 1.3 Simulated annual trends in nearshore pH and oxygen, and in their drivers, during peak upwelling season as a function of latitude for 1988-2010. (a) pH (red) and oxygen (blue) trends at 10m depth. (b) Vertical velocity trend at 40m depth (red) and phytoplankton biomass trend at 10m depth (blue). (c) DIC (red) and alkalinity (blue) trends at 10m depth. Purple shading indicates negative (or less positive) trends in pH and oxygen associated with strongly positive trends in upwelling. Green shading indicates positive (or less negative) trends in pH and oxygen associated with strongly positive trends in phytoplankton biomass. Blue shading indicates positive trends in pH and oxygen associated with negative trends in phytoplankton biomass and remineralization. All variables represent 0-30km offshore averages.

At the regional scale, the overall trend for nearshore oxygen is mainly positive north of Pt Arena ( $\sim 39^{\circ}\text{N}$ ) and near zero to the south. Between  $39.5\text{-}42^{\circ}\text{N}$ , the positive trend may be explained by a weaker trend in upwelling intensity combined with an increasing trend in phytoplankton biomass. Between  $41\text{-}42^{\circ}\text{N}$ , the positive trend is apparently related to a decrease in water column remineralization associated with a negative trend in phytoplankton biomass. South of  $39^{\circ}\text{N}$ , the stronger trend in upwelling intensification is approximately balanced by the associated larger positive trend in phytoplankton biomass, leading to a weakly positive or negative oxygen trend. In contrast, the overall trend in nearshore pH is predominantly negative (i.e., acidification) south of Cape Mendocino ( $\sim 40^{\circ}\text{N}$ ), near zero to the north, and appears

related to the relative magnitude of the DIC and alkalinity trends at 10m depth. North of 40°N, the trends in upwelling intensity and DIC are weaker and the alkalinity trend is more positive (due to the increasing trend in nitrate consumption by phytoplankton), resulting in a compensating effect on the pH trend. South of 40°N, the trend in alkalinity is outweighed by stronger trends in upwelling intensity and DIC, resulting in a negative pH trend.

### 1.5 Discussion

Results from a high-resolution coupled physical-biogeochemical model are used to characterize alongshore variability in the mean states and trends of nearshore surface pH and oxygen in the central CCS during 1988-2010. The findings demonstrate a complex interplay between local and regional scale processes, where changes in upwelling intensity, primary production, and coastal currents establish a succession of alongshore minima and maxima in the means and trends of nearshore pH and oxygen (Fig. 1.4). Regions of enhanced upwelling lead to a local decrease in pH and oxygen, and regions of increased primary production result in a local increase in pH and oxygen. While enhanced upwelling and vertical nutrient fluxes occur near coastal promontories, pH and oxygen minima and maxima are shifted downstream by local advection. This interpretation parallels the findings of Fiechter et al. (2018), which reported a succession of nutrients and chlorophyll peaks, driven by local-scale variability in coastal upwelling intensity and nearshore currents. Local maxima in pH and oxygen also occur in areas associated with onshore meanders in the geostrophic circulation, which effectively reduce coastal upwelling intensity (Marchesiello and

Estrade, 2010) and increase pH and oxygen content of upwelled source waters as nearshore isopycnal uplift is reduced. The regions of strong onshore geostrophic flow identified here near 36°N and 39°N, and subsequent impacts on coastal upwelling intensity, generally agree with existing numerical studies and observations (Centurioni et al., 2008; Jacox et al., 2014).

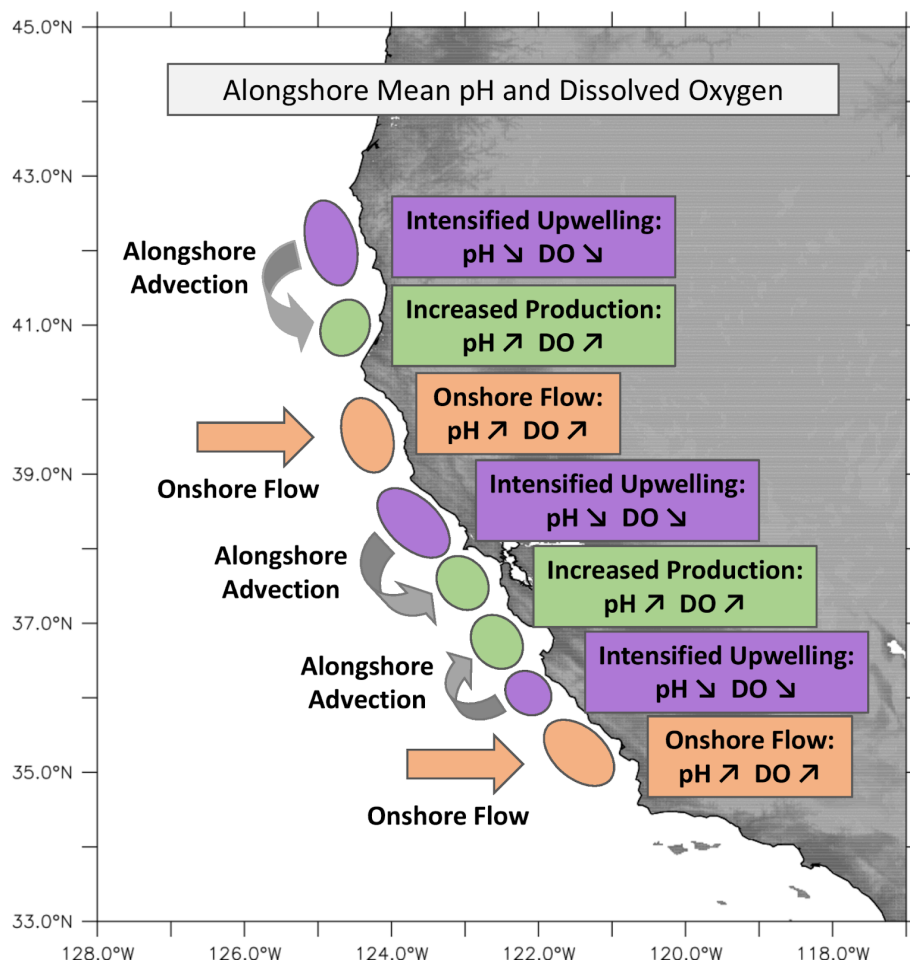


Figure 1.4 Processes controlling nearshore pH and oxygen in the central CCS. Alongshore variability in pH and oxygen are illustrated as a result of the interplay between local upwelling intensification, increased primary production, and coastal ocean circulation. Regions experiencing lower pH and lower oxygen in response to upwelling intensification are represented with purple circles. Regions of higher pH and higher oxygen in response to increased primary production are represented with green circles. Regions of elevated pH and elevated oxygen in response to onshore geostrophic flow are represented with orange circles. Alongshore advection is represented with gray arrows and onshore geostrophic flow is represented with orange arrows.

The strong pH minimum ( $\sim 7.91$ ) present in the model near  $38^\circ\text{N}$  is consistent with nearshore observations in the central CCS, which identified severe low pH exposure and synoptic values near 7.9 during the upwelling season just north of  $38^\circ\text{N}$  (Chan et al., 2018). The same study also indicates that exposure to low pH is more severe near Cape Blanco ( $\sim 43^\circ\text{N}$ ) and less severe near Monterey Bay ( $36.5\text{-}37^\circ\text{N}$ ) and Cape Mendocino ( $\sim 40^\circ\text{N}$ ), which qualitatively agrees with the local minima and maxima in nearshore pH at 10m depth produced by the simulation. At the regional scale, in situ data from a synoptic shipboard survey describe an alongshore pattern of shallower ( $36\text{-}38^\circ\text{N}$  and  $40\text{-}44^\circ\text{N}$ ) and deeper ( $35\text{-}36^\circ\text{N}$  and  $38\text{-}40^\circ\text{N}$ ) aragonite saturation horizons (Feely et al. 2008), corresponding to regions of, respectively, offshore and onshore meanders of the geostrophic flow in the model (see Fig. 1.2d). This finding suggests that broader alongshore patterns in nearshore pH and oxygen may be controlled by changes in the vertical density structure and upwelled source water content in response to modulations of coastal upwelling efficiency by the regional circulation.

The alongshore variability of simulated trends in pH and oxygen during 1988-2010 respond to similar physical and biogeochemical processes as the long-term means. pH and oxygen exhibit negative (or less positive) trends directly downstream of upwelling centers in response to increased nearshore supply of DIC-rich and oxygen-poor subsurface waters, and positive (or less negative) trends at locations where phytoplankton biomass is increasing and enhances DIC consumption and oxygen production through photosynthesis. While simulated pH and oxygen trends

are useful to identify mechanisms controlling nearshore tendencies, the magnitude of the trends may be inflated by decadal basin-scale variability in the North Pacific during 1988-2010. The rather short duration of the model run (23 years), combined with a phase transition of the North Pacific Gyre Oscillation and the Pacific Decadal oscillation in the late 1990s (Di Lorenzo et al., 2008; Peterson and Schwing, 2003), mean that the increasing trend in coastal upwelling intensity (and subsequent trends in nearshore pH and oxygen) may reflect a shift from an unproductive to a productive regime in the CCS halfway through the simulation, rather than a long-term anthropogenic signal. Despite a small change in the magnitude of mean pH and oxygen values, the simulated alongshore patterns remain consistent across the regime shift. Furthermore, since the boundary conditions for biogeochemical variables are climatological (i.e., no long-term trends in DIC, nutrients, and oxygen), anthropogenic impacts in the model are limited to oceanic physical variability and surface atmospheric forcing (i.e., changes in upwelling favorable winds and atmospheric CO<sub>2</sub> concentrations).

In summary, the results presented here highlight the strong alongshore heterogeneity in mean pH and oxygen patterns in the central CCS, and provide a mechanistic description of their physical and biogeochemical drivers at previously unresolved spatial scales. Since nearshore pH and oxygen trends exhibit similar alongshore variability, the progression of ocean acidification and hypoxia in this region will also not be spatially homogeneous. These findings reinforce the notion that assessment of anthropogenic impacts on coastal ecosystem processes in the CCS

(and presumably in other eastern boundary current upwelling systems) should not rely on regionally averaged metrics, but instead be characterized locally at relevant physical and ecological alongshore scales.

## 1.6 Acknowledgements

This research was supported by grants OCE-1566623 and OCE-1635315 from the National Science Foundation Division of Ocean Sciences. Any opinions, findings, and conclusions or recommendations expressed here are those of the authors and do not necessarily reflect the views of the National Science Foundation. The authors thank two anonymous reviewers for their constructive comments. The model output is deposited on Dryad and available at <https://doi.org/10.7291/D1D96Q>. The CalCOFI observations are available at <https://calcofi.org/ccdata.html>, and the WCOA cruise observations are available at <https://coastwatch.pfeg.noaa.gov/erddap/index.html>.

## 1.7 References

Alin, S. R., Feely, R. A., Dickson, A. G., Hernández-Ayón, J. M., Juranek, L. W., Ohman, M. D., & Goericke, R. (2012). Robust empirical relationships for estimating the carbonate system in the southern California Current System and application to CalCOFI hydrographic cruise data (2005–2011). *Journal of Geophysical Research: Oceans*, 117(C5).

<https://doi.org/10.1029/2011JC007511>

Atlas, R., Hoffman, R. N., Ardizzone, J., Leidner, S. M., Jusem, J. C., Smith, D. K.,

- & Gombos, D. (2011). A Cross-calibrated, Multiplatform Ocean Surface Wind Velocity Product for Meteorological and Oceanographic Applications. *Bulletin of the American Meteorological Society*, 92(2), 157–174.  
<https://doi.org/10.1175/2010BAMS2946.1>
- Barth, J. A., Pierce, S. D., & Smith, R. L. (2000). A separating coastal upwelling jet at Cape Blanco, Oregon and its connection to the California Current System. *Deep Sea Research Part II: Topical Studies in Oceanography*, 47(5-6), 783–810.
- Baumann, H., & Smith, E. M. (2018). Quantifying Metabolically Driven pH and Oxygen Fluctuations in US Nearshore Habitats at Diel to Interannual Time Scales. *Estuaries and Coasts*, 41(4), 1102–1117.  
<https://doi.org/10.1007/s12237-017-0321-3>
- Bograd, S. J., Castro, C. G., Di Lorenzo, E., Palacios, D. M., Bailey, H., Gilly, W., & Chavez, F. P. (2008). Oxygen declines and the shoaling of the hypoxic boundary in the California Current. *Geophysical Research Letters*, 35(12).  
<https://doi.org/10.1029/2008GL034185>
- Brady R., Lovenduski, N., Yeager, S. G., Long, M. C., Lindsay, K. (2020): Skillful multiyear predictions of ocean acidification in the California Current System. *Nature Communications*, 11: article 2166. DOI: 10.1038/s41467-02015722-x
- Carton, J. A., Chepurin, G., & Cao, X. (2000). A Simple Ocean Data Assimilation



- Analysis of the Global Upper Ocean 1950–95. Part II: Results. *Journal of Physical Oceanography*, 30(2), 311–326. [https://doi.org/10.1175/1520-0485\(2000\)030<0311:ASODAA>2.0.CO;2](https://doi.org/10.1175/1520-0485(2000)030<0311:ASODAA>2.0.CO;2)
- Centurioni, L. R., Ohlmann, J. C., & Niiler, P. P. (2008). Permanent Meanders in the California Current System. *Journal of Physical Oceanography*, 38(8), 1690–1710. <https://doi.org/10.1175/2008JPO3746.1>
- Chan, F., Barth, J. A., Blanchette, C. A., Byrne, R. H., Chavez, F., Cheriton, O., et al. (2017). Persistent spatial structuring of coastal ocean acidification in the California Current System. *Scientific Reports*, 7(1), 2526. <https://doi.org/10.1038/s41598-017-02777-y>
- Conkright, M. E., & Boyer, T. P. (2002). *World Ocean Atlas 2001: Objective Analyses, Data Statistics, and Figures* (p. 17). Silver Spring, MD: CD-ROM Documentation, National Oceanographic Data Center.
- Di Lorenzo, E., Schneider, N., Cobb, K. M., Franks, P. J. S., Chhak, K., Miller, A. J., et al. (2008). North Pacific Gyre Oscillation links ocean climate and ecosystem change. *Geophysical Research Letters*, 35(8). <https://doi.org/10.1029/2007GL032838>
- Dussin, R., Curchitser, E.N., Stock, C.A., & Van Oostende, N. (2019). Biogeochemical drivers of changing hypoxia in the California Current Ecosystem. *Deep Sea Research Part II: Topical Studies in Oceanography* 169-170, 104590. <https://doi.org/10.1016/j.dsr2.2019.05.013>
- Feely, R. A., Sabine, C. L., Hernandez-Ayon, J. M., Ianson, D., & Hales, B. (2008).

- Evidence for Upwelling of Corrosive “Acidified” Water onto the Continental Shelf. *Science*, 320(5882), 1490. <https://doi.org/10.1126/science.1155676>
- Fennel, K.; Hu, J.; Laurent, A.; Marta-Almeida, M.; Hetland, R. (2013). Sensitivity of Hypoxia Predictions for the Northern Gulf of Mexico to Sediment Oxygen Consumption and Model Nesting. *J. Geophys. Res. Ocean.* 2013, 118 (2), 990-1002. <https://doi.org/10.1002/jgrc.20077>.
- Fiechter, J., Curchitser, E. N., Edwards, C. A., Chai, F., Goebel, N. L., & Chavez, F. P. (2014). Air-sea CO<sub>2</sub> fluxes in the California Current: Impacts of model resolution and coastal topography. *Global Biogeochemical Cycles*, 28(4), 371–385. <https://doi.org/10.1002/2013GB004683>
- Fiechter, J., Edwards, C. A., & Moore, A. M. (2018). Wind, Circulation, and Topographic Effects on Alongshore Phytoplankton Variability in the California Current. *Geophysical Research Letters*, 45(7), 3238–3245. <https://doi.org/10.1002/2017GL076839>
- Fiechter, J., J.A. Santora, F. Chavez, D. Northcott, M. Messié (2020). Krill hotspot formation and phenology in the California Current Ecosystem. *Geophysical Research Letters*, 47, e2020GL088039. <https://doi.org/10.1029/2020GL088039>.
- Gruber, N., Hauri, C., Lachkar, Z., Loher, D., Frölicher, T. L., & Plattner, G.-K. (2012). Rapid Progression of Ocean Acidification in the California Current System. *Science*, 337(6091), 220. <https://doi.org/10.1126/science.1216773>
- Haidvogel, D. B., Arango, H., Budgell, W. P., Cornuelle, B. D., Curchitser, E., Di

- Lorenzo, E., et al. (2008). Ocean forecasting in terrain-following coordinates: Formulation and skill assessment of the Regional Ocean Modeling System. *Predicting Weather, Climate and Extreme Events*, 227(7), 3595–3624. <https://doi.org/10.1016/j.jcp.2007.06.016>
- Hauri, C., Gruber, N., Vogt, M., Doney, S. C., Feely, R. A., Lachkar, Z., et al. (2013). Spatiotemporal variability and long-term trends of ocean acidification in the California Current System. *Biogeosciences*, 10(1), 193–216. <https://doi.org/10.5194/bg-10-193-2013>
- Hauri, C., Gruber, N., McDonnell, A. M. P., & Vogt, M. (2013). The intensity, duration, and severity of low aragonite saturation state events on the California continental shelf. *Geophysical Research Letters*, 40(13), 3424–3428. <https://doi.org/10.1002/grl.50618>
- Howard, E.M., J. L. Penn, H. Frenzel, B. A. Seibel, D. Bianchi, L. Renault, F. Kessouri, M. A. Sutula, J. C. McWilliams, C. Deutsch, (2020). Climate-driven aerobic habitat loss in the California Current System. *Sci. Adv.* 6, eaay3188. <https://doi.org/10.1126/sciadv.aay3188>
- Huyer, A. (1983). Coastal upwelling in the California current system. *Progress in Oceanography*, 12(3), 259–284. [https://doi.org/10.1016/0079-6611\(83\)90010-1](https://doi.org/10.1016/0079-6611(83)90010-1)
- Jacox, M. G., Fiechter, J., Moore, A. M., & Edwards, C. A. (2015). ENSO and the California Current coastal upwelling response. *Journal of Geophysical Research: Oceans*, 120(3), 1691–1702. <https://doi.org/10.1002/2014JC010650>

- Jacox, M. G., Moore, A. M., Edwards, C. A., & Fiechter, J. (2014). Spatially resolved upwelling in the California Current System and its connections to climate variability. *Geophysical Research Letters*, *41*(9), 3189–3196.  
<https://doi.org/10.1002/2014GL059589>
- Key, R., Kozyr, A., Chris, S., Lee, K., Wanninkhof, R., Bullister, J., et al. (2004). A global ocean carbon climatology: Results from Global Data Analysis Project GLODAP). *Global Biogeochem. Cycles*, *18*.  
<https://doi.org/10.1029/2004GB002247>
- Kishi, M. J., Kashiwai, M., Ware, D. M., Megrey, B. A., Eslinger, D. L., Werner, F. E., et al. (2007). NEMURO—a lower trophic level model for the North Pacific marine ecosystem. *Special Issue on NEMURO (North Pacific Ecosystem Model for Understanding Regional Oceanography) and NEMURO.FISH (NEMURO for Including Saury and Herring)*, *202*(1), 12–25.  
<https://doi.org/10.1016/j.ecolmodel.2006.08.021>
- Kudela, R.M., Banas, N.S., Barth, J.A., Frame, E.R., Jay, D.A., Largier, J.L., et al. (2008). New Insights into the Controls and Mechanisms of Plankton Productivity in Coastal Upwelling Waters of the Northern California Current System. *Oceanography*, *21*(4), 46–59.
- Marchesiello, P., McWilliams, J. C., & Shchepetkin, A. (2003). Equilibrium Structure and Dynamics of the California Current System. *Journal of Physical Oceanography*, *33*(4), 753–783. [https://doi.org/10.1175/1520-0485\(2003\)33<753:ESADOT>2.0.CO;2](https://doi.org/10.1175/1520-0485(2003)33<753:ESADOT>2.0.CO;2)

- Neveu, E., Moore, A. M., Edwards, C. A., Fiechter, J., Drake, P., Crawford, W. J., et al. (2016). An historical analysis of the California Current circulation using ROMS 4D-Var: System configuration and diagnostics. *Ocean Modelling*, 99, 133–151. <https://doi.org/10.1016/j.ocemod.2015.11.012>
- Peterson, W. T., & Schwing, F. B. (2003). A new climate regime in northeast Pacific ecosystems. *Geophysical Research Letters*, 30(17).  
<https://doi.org/10.1029/2003GL017528>
- Pickett, M. H., & Paduan, J. D. (2003). Ekman transport and pumping in the California Current based on the U.S. Navy's high-resolution atmospheric model (COAMPS). *Journal of Geophysical Research: Oceans*, 108(C10).  
<https://doi.org/10.1029/2003JC001902>
- Schroeder, I. D., J. A. Santora, A. M. Moore, C. A. Edwards, J. Fiechter, E. L. Hazen, S. J. Bograd, J. C. Field, and B. K. Wells (2014). Application of a data-assimilative regional ocean modeling system for assessing California Current System ocean conditions, krill, and juvenile rockfish interannual variability. *Geophys. Res. Lett.*, 41, doi:10.1002/2014GL061045.
- Shchepetkin, A. F., & McWilliams, J. C. (2005). The regional oceanic modeling system (ROMS): a split-explicit, free-surface, topography-following-coordinate oceanic model. *Ocean Modelling*, 9(4), 347–404.  
<https://doi.org/10.1016/j.ocemod.2004.08.002>
- Siedlecki, S.A., Banas, N., Davis, K.A., Giddings, S., Hickey, B.M., MacCready, P.,

Connolly, T., and S. Geier, Seasonal and interannual oxygen variability on the Washington and Oregon continental shelves, (2015), *J. Geophys. Res. Oceans*, 120, DOI: 10.1002/2014JC010254

Siedlecki, S.A., Kaplan, I.C., Hermann, A., Nguyen, T., Bond, N., Williams, G., Newton, J., Peterson, W. T., Alin, S., and R.A. Feely (2016) Experiments with Seasonal Forecasts of ocean conditions for the Northern region of the California Current upwelling system, *Nature: Scientific Reports* 6, doi:10.1038/srep27203

## 1.8 Supplementary information

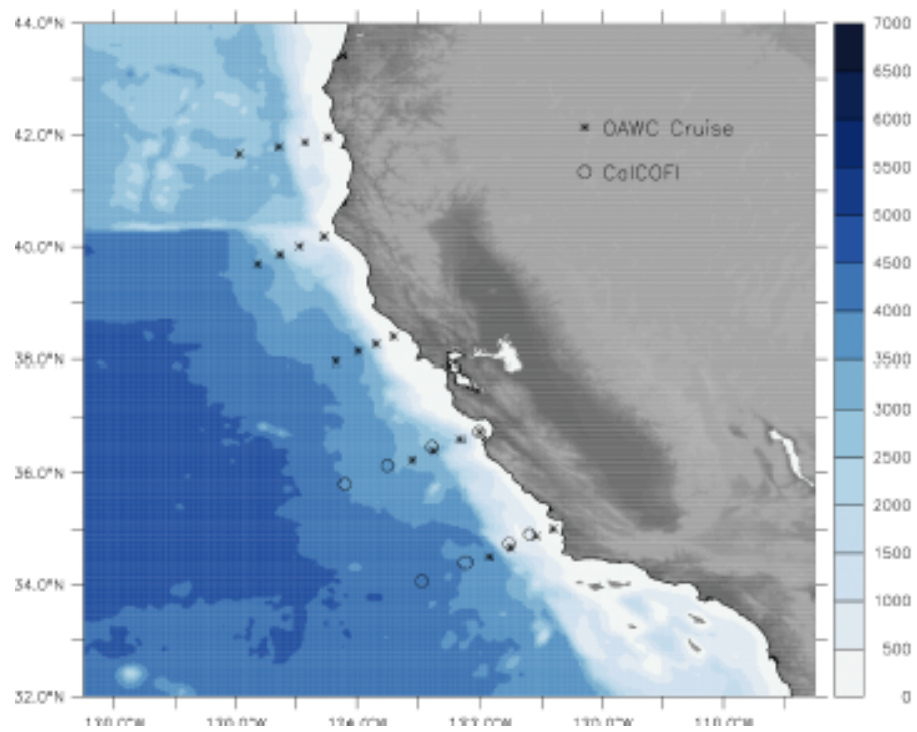


Figure S1.1 Map of in-situ observations used for model evaluation. Open circles denote CalCOFI survey lines 67 (near 36.5°N) and 77 (near 34.5°N). Stars denote survey lines from NOAA's 2007 West Coast Ocean Acidification (WCOA) Cruise.

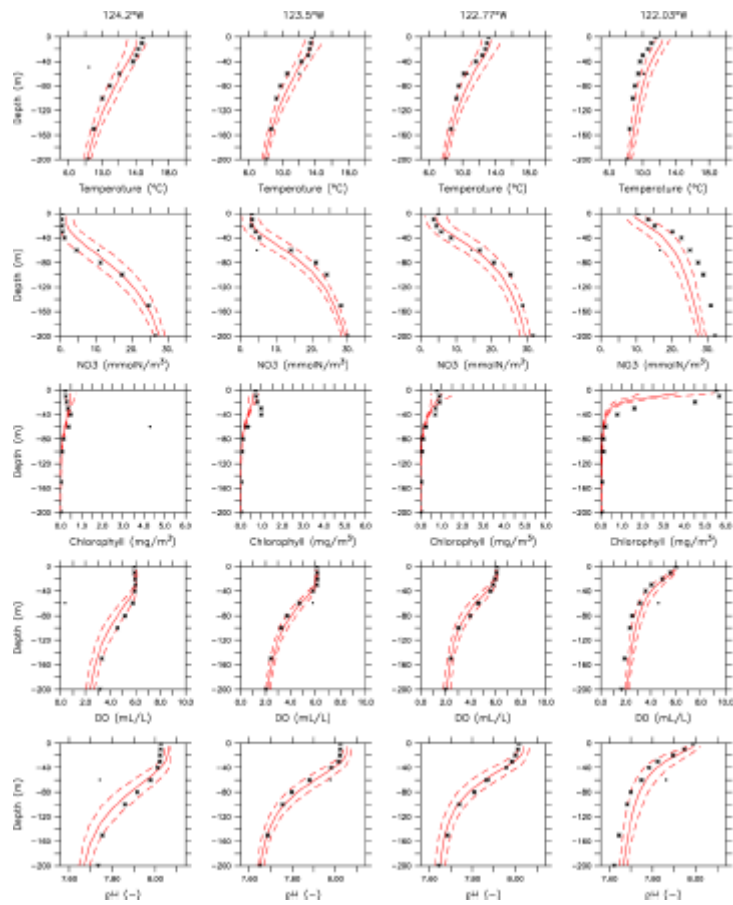


Figure S1.2 Springtime (Apr-Jun) simulated (red lines) and observed (black symbol) climatological profiles of (from top-to-bottom) temperature (C), nitrate (mmolN/m<sup>3</sup>), chlorophyll (mg/m<sup>3</sup>), dissolved oxygen (mL/L) and pH along CalCOFI line 67 from offshore (left) to nearshore (right). Simulated values are expressed as Apr-Jun climatological mean (solid line)  $\pm$  one standard deviation (dashed lines). Observations are climatological mean based synoptic values from Apr-Aug surveys.



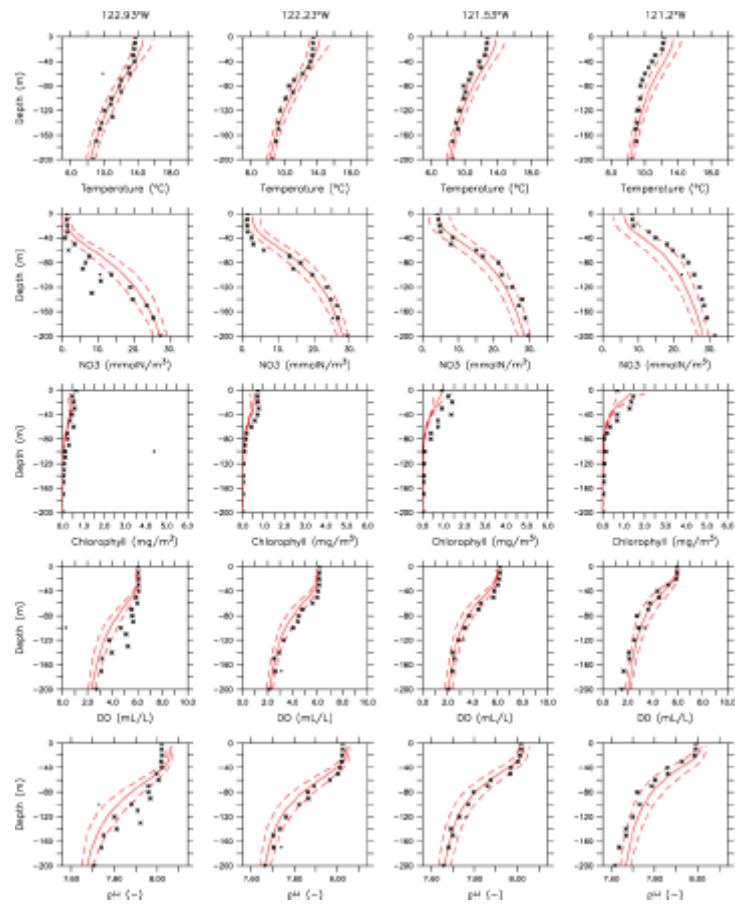


Figure S1.3 Springtime simulated (red lines) and observed (black symbol) climatological profiles of (from top-to-bottom) temperature (C), nitrate (mmolN/m<sup>3</sup>), chlorophyll (mg/m<sup>3</sup>), dissolved oxygen (mL/L) and pH along CalCOFI line 77 from offshore (left) to nearshore (right). Simulated values are expressed as Apr-Jun climatological mean (solid line)  $\pm$  one standard deviation (dashed lines). Observations are climatological mean based synoptic values from Apr-Aug surveys.

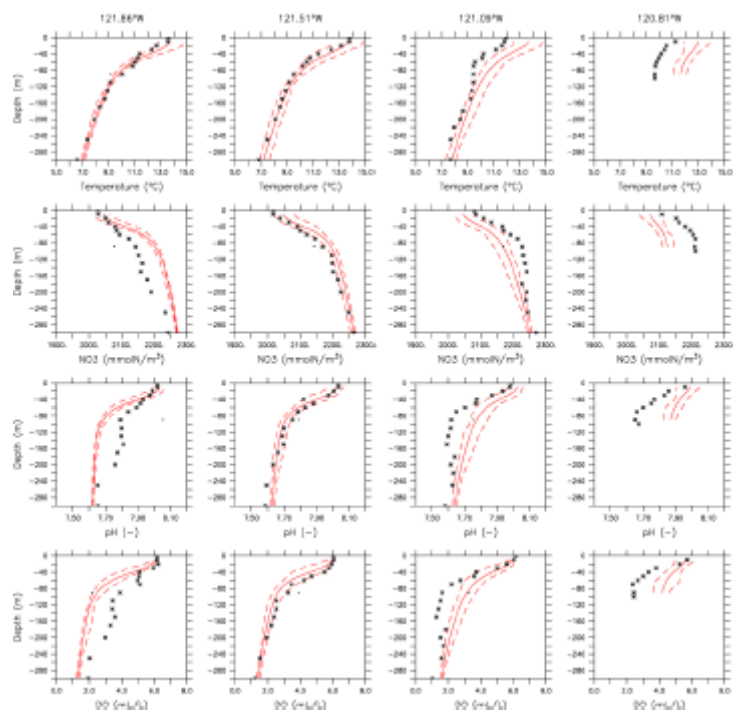


Figure S1.4 Simulated (red lines) and observed (black symbol) profiles of (from top-to-bottom) temperature (C), nitrate (mmolN/m<sup>3</sup>), pH and dissolved oxygen (mL/L) during May-Jun 2007 along WCOA Cruise transect near 42°N from offshore (left) to nearshore (right). Simulated values are expressed as May-Jun mean (solid line)  $\pm$  one standard deviation (dashed lines). Observations are synoptic values.

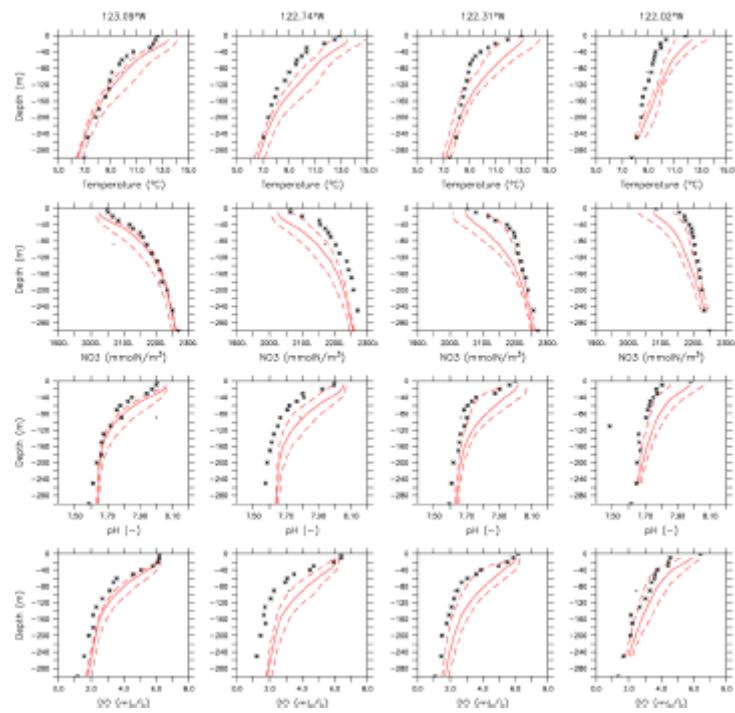


Figure S1.5 Springtime simulated (red lines) and observed (black symbol) climatological profiles of (from top-to-bottom) temperature (C), nitrate (mmolN/m<sup>3</sup>), pH and dissolved oxygen (mL/L) during May-Jun 2007 along WCOA Cruise transect near 40°N from offshore (left) to nearshore (right). Simulated values are expressed as May-Jun mean (solid line)  $\pm$  one standard deviation (dashed lines). Observations are synoptic values.

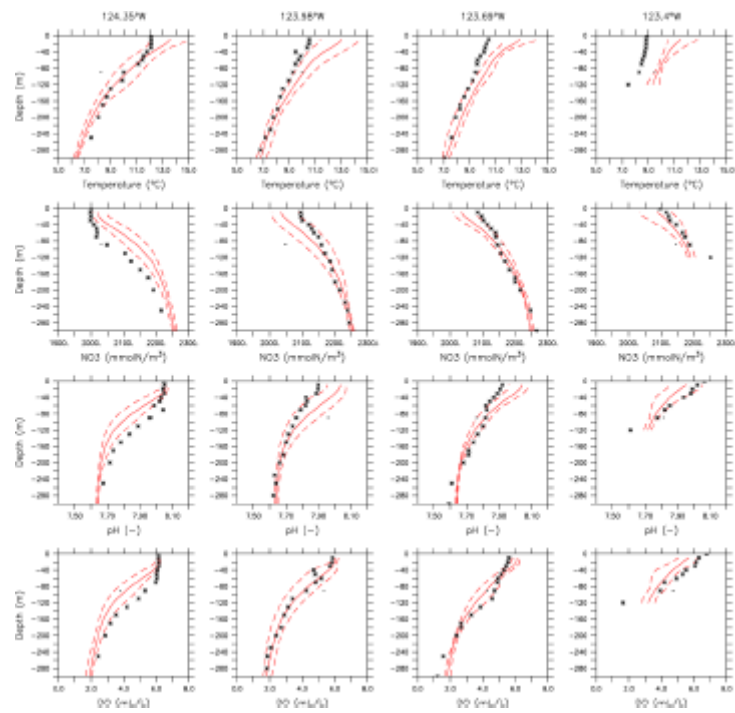


Figure S1.6 Springtime simulated (red lines) and observed (black symbol) climatological profiles of (from top-to-bottom) temperature (C), nitrate (mmolN/m<sup>3</sup>), pH and dissolved oxygen (mL/L) during May-Jun 2007 along WCOA Cruise transect near 38°N from offshore (left) to nearshore (right). Simulated values are expressed as May-Jun mean (solid line)  $\pm$  one standard deviation (dashed lines). Observations are synoptic values.

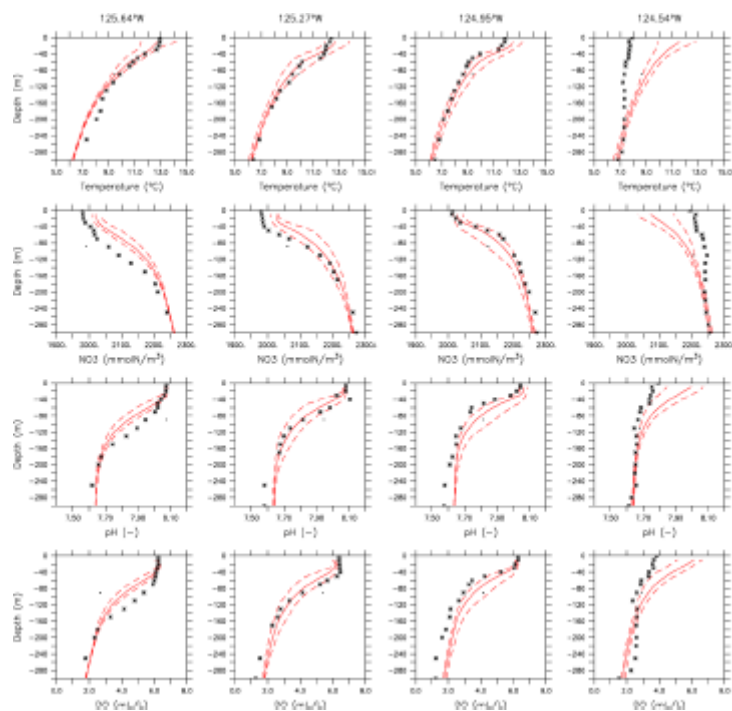


Figure S1.7 Springtime simulated (red lines) and observed (black symbol) climatological profiles of (from top-to-bottom) temperature (C), nitrate (mmolN/m<sup>3</sup>), pH and dissolved oxygen (mL/L) during May-Jun 2007 along WCOA Cruise transect near 36°N from offshore (left) to nearshore (right). Simulated values are expressed as May-Jun mean (solid line)  $\pm$  one standard deviation (dashed lines). Observations are synoptic values.

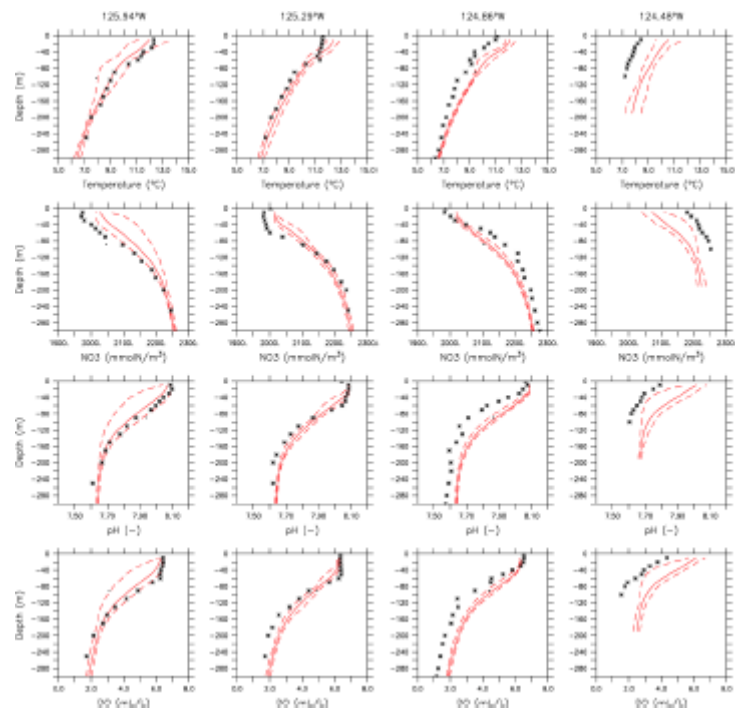


Figure S1.8 Springtime simulated (red lines) and observed (black symbol) climatological profiles of (from top-to-bottom) temperature (C), nitrate (mmolN/m<sup>3</sup>), pH and dissolved oxygen (mL/L) during May-Jun 2007 along WCOA Cruise transect near 34°N from offshore (left) to nearshore (right). Simulated values are expressed as May-Jun mean (solid line)  $\pm$  one standard deviation (dashed lines). Observations are synoptic values.

## Chapter 2 - Upwelling intensity and source water properties drive high interannual variability of corrosive events in the California Current

Julia Cheresch, Kristy Kroeker and Jerome Fiechter

### 2.1 Abstract

Ocean acidification is progressing rapidly in the California Current System (CCS), a region already susceptible to reduced aragonite saturation state due to seasonal coastal upwelling. Results from a high-resolution (~3 km), coupled physical-biogeochemical model highlight that the intensity, duration, and severity of undersaturation events exhibit high interannual variability along the central CCS shelfbreak. Variability in dissolved inorganic carbon (DIC) along the bottom of the 100-m isobath explains 70-90% of event severity variance over the range of latitudes where most severe conditions occur. An empirical orthogonal function (EOF) analysis further reveals that interannual event variability is explained by a combination coastal upwelling intensity and DIC content in upwelled source waters. Simulated regional DIC exhibits low frequency temporal variability resembling that of the Pacific Decadal Oscillation, and is explained by changes to water mass composition in the CCS. While regional DIC concentrations and upwelling intensity individually explain 9 and 43% of year-to-year variability in undersaturation event severity, their combined influence accounts for 66% of the variance. The mechanistic description of exposure to undersaturated conditions presented here provides important context for monitoring the progression of ocean acidification in the CCS and identifies conditions leading to increased vulnerability for ecologically and commercially important species.

## 2.2 Introduction

The global ocean has absorbed approximately 25% of anthropogenic  $CO_2$  emissions since the beginning of the industrial era [1], resulting in ocean acidification. Rapid reductions in pH and carbonate ion ( $CO_3^{2-}$ ) concentration in the upper ocean have emerged as pressing threats to marine life [2]. Of particular concern is decreasing calcium carbonate mineral ( $CaCO_3$ ) saturation states and its less stable polymorph aragonite. The saturation state of aragonite ( $\Omega_{arag}$ ) in seawater depends on the concentrations of calcium ( $[Ca^{2+}]$ ) and carbonate ions ( $[CO_3^{2-}]$ ), as well as the apparent solubility of aragonite ( $K'_{sparag}$ ) at in situ temperature, salinity, and pressure, expressed as:

$$\Omega_{arag} = [Ca^{2+}][CO_3^{2-}] K'_{sparag}$$

At  $\Omega_{arag}$  less than 1, dissolution of aragonite becomes thermodynamically favorable, posing risk to organisms which use calcium carbonate minerals to build shells and skeletons.

The effects of ocean acidification are exacerbated in the California Current System (CCS) due to coastal upwelling [3,4]. In spring and summer, equatorward winds intensify along the west coast of North America. Upwelling favorable winds drive offshore transport of the surface Ekman layer, which is then replaced near the coast by waters originating from depths between 50-100m [5,6,7]. These waters are rich in nutrients and both natural and anthropogenic  $CO_2$ , making them simultaneously low in pH and  $\Omega_{arag}$  [7,8,9]. During upwelling events, enhanced



nutrient content in upwelled water supports elevated primary production, which increases  $\Omega_{\text{arag}}$  near the surface by drawing down  $\text{CO}_2$  levels, but also reduces  $\Omega_{\text{arag}}$  at depth due to subsequent remineralization of production exported below the mixed layer. The addition of anthropogenic  $\text{CO}_2$  in a naturally low pH and low  $\Omega_{\text{arag}}$  environment is expected to push conditions beyond biological thresholds, causing a variety of deleterious responses [2,10,11]. The depth at which  $\Omega_{\text{arag}}$  becomes undersaturated, known as the  $\Omega_{\text{arag}}$  saturation horizon, has already shoaled in nearshore waters of the CCS by 25-40m since the preindustrial era, and corrosive waters have been observed on the continental shelf [7,12].

Due to the intermittent nature of upwelling, whereby alongshore persisting for several days to weeks are followed by periods of relaxation, events of  $\Omega_{\text{arag}}$  undersaturation are episodic in nature [4,13]. Such events have been captured in synoptic surveys as well as long-term time series, which documented exposure to corrosive conditions during periods of enhanced upwelling-favorable wind stress [7,14]. Alongshore variability in coastline topography also modulates atmospheric wind patterns and nearshore ocean circulation, thereby impacting the local magnitude of upwelling intensity, primary production, and pH on the shelf [15,16,17,18, 19]. Furthermore, upwelling and primary production exhibit strong interannual variability due to changes in atmospheric and oceanic forcing associated with modes of climate variability, such as the El Niño Southern Oscillation (ENSO) [20,21], Pacific Decadal Oscillation (PDO) [22,23] and North Pacific Gyre Oscillation (NPGO) [24,25]. Due to their highly variable nature, the physical and biogeochemical drivers of low  $\Omega_{\text{arag}}$

exposure in the CCS are typically difficult to fully interpret based on synoptic surveys and stationary time series. Coupled physical-biogeochemical ocean models provide a means to resolve variability at spatial and temporal scales observational platforms cannot simultaneously capture. Existing modeling studies have yielded important insights into the drivers of ocean acidification exposure in the CCS, and many have relied upon spatially-averaged metrics to focus on regional or basin scale processes shaping ocean acidification [26,3,27,28,29,30]. Exposure to low pH conditions (one of the important determinants of  $\Omega_{\text{arag}}$  in the CCS) has been shown to exhibit strong alongshore heterogeneity, shaped by regional and local physical and biogeochemical processes, suggesting spatially-averaged metrics may obscure finer scale variability important to ocean acidification exposure [19].

A framework to quantify low  $\Omega_{\text{arag}}$  events by duration, intensity and severity was developed to characterize future exposure under a high emissions scenario using model output for the CCS [27]. The results highlighted that low  $\Omega_{\text{arag}}$  events in the CCS will become more frequent and severe with increasing anthropogenic  $\text{CO}_2$  emissions. However, a comprehensive mechanistic understanding of the drivers of these events in a recent historical context is still lacking. The present study aims to address this gap using a  $\sim 3$  km horizontal resolution ocean model spanning 1988-2010 to characterize the physical and biogeochemical drivers of  $\Omega_{\text{arag}}$  undersaturation event intensity, duration, and severity at spatial and temporal scales relevant to marine ecosystem management. Since the rapid progression of OA along the U.S. west coast is projected to be spatially heterogeneous [28,30,19], a comprehensive

understanding of the mechanisms driving historical exposure to low  $\Omega_{\text{arag}}$  provides valuable context for interpreting future intensity, duration and severity of exposure to undersaturation in the CCS due to anthropogenic climate change.

## 2.3 Methods

### 2.3.1 Model Configuration

The physical circulation is resolved by the Regional Ocean Modeling System (ROMS) [31,32]. ROMS was configured with 42 terrain-following depth levels and a grid nesting approach consisting of an inner domain for the central CCS (32- 44°N, 116.5-128.5°W) at 1/30° (~3 km) resolution forced by an outer domain for the broader CCS (30-48°N, 115-134°W) at 1/10° (~10 km) resolution with physical data assimilation. The physical circulation is forced at the surface by the 0.25° resolution Cross-Calibrated Multi-Platform (CCMP) winds [33], and physical initial and boundary conditions for the outer domain are derived from the Simple Ocean Data Assimilation (SODA) reanalysis [34]. A complete description of the physical model configuration can be found in Fiechter et al. (2018) [18].

Biogeochemical processes are simulated using NEMUCSC, an adaptation of the North Pacific Ecosystem Model for Understanding Regional Oceanography (NEMURO) [35], with the addition of carbon and oxygen cycling based on formulations of Hauri et al. (2013a,b) [27,28], and Fennel et al. (2013) [36], respectively. Boundary and initial conditions for the outer domain are derived from the World Ocean Atlas monthly climatology for nutrients and oxygen [37], from the Global Ocean Data Analysis project for total alkalinity (TAlk) [38], and from the

empirical relationship of Alin et al. (2012) [39] for dissolved organic carbon (DIC) based on monthly temperature and oxygen. Due to their climatological nature, the boundary conditions do not reflect global and basin-scale trends in biogeochemical properties. Atmospheric  $pCO_2$  is prescribed based on the Mauna Loa time series, with a superimposed mean seasonal cycle and annual increase of 1.5 ppmv before 1995 and 2 ppmv thereafter. A complete description of the biogeochemical model configuration can be found in Cheresh & Fiechter (2020) [19].

The analysis presented here is based on the higher-resolution inner domain at ~3 km resolution and focuses on the region between Pt Conception and Cape Blanco (35-43°N), which is known to exhibit substantial alongshore variability in physical and biogeochemical processes influencing pH (and presumably  $\Omega_{arag}$  due to their strong covariability in the CCS) [20]. While the full simulation spans 1980-2010, the analysis is limited to 1988-2010 to eliminate spin-up effects.

### 2.3.2 Model evaluation

The model is evaluated with observations from the 2007 West Coast Ocean Acidification (WCOA) Cruise between 35-42°N by comparing simulated daily mean values for May-June 2007 to synoptic measurements from 0-300m depth at the 4 stations closest to shore along each transect. The ability of the model to reproduce temporal and alongshore properties of undersaturation events is also evaluated using daily-averaged model output compared to daily-averaged observations from nearshore moorings deployed at approximately 12-m depth within kelp forests at ~35.2, 36.0, 38.9, and 39.3°N [41]. Because the observations (2017-2019) and

simulation (1988-2010) do not overlap in time, the model is evaluated for its ability to reproduce the mean, range, and monthly climatological properties of measured pH, temperature, and dissolved oxygen (DO). An event analysis (as described below) is applied to simulated and observed variables to further assess the capacity of the model to capture low pH events ( $\text{pH} < 7.7$ , which approximates a mean  $\Omega_{\text{arag}}$  of 1 over a wide range of TAlk values regularly observed in the CCS (i.e., 2100-2300  $\mu\text{mol/kg}$ ).

### 2.3.3 Event analysis

The event analysis focuses on determining the properties of undersaturated events with respect to aragonite, where “events” are defined as periods of time when  $\Omega_{\text{arag}}$  values are lower than a specified threshold. Following Hauri et al. (2013), events are characterized by their intensity, duration, and severity [27]. Duration (D) represents the number of consecutive days  $\Omega_{\text{arag}}$  values are below the threshold during an event. Intensity (I) represents the difference between the threshold (T) and the mean saturation state ( $\Omega_{\text{mean}}$ ) during an event ( $I = T - \Omega_{\text{mean}}$ ). Severity is quantified as the product of duration and intensity ( $S = D \times I$ ). Although biological thresholds are presumably species- or even population-specific, a heuristic threshold of  $\Omega_{\text{arag}} = 1$  is chosen here, as exposure to saturation states below 1 thermodynamically favors dissolution of calcium carbonate.

Intensity, duration, and severity are calculated using daily averaged model fields extracted along the 100-m isobath as a location characteristic of alongshore,

seasonal, and interannual event variability affecting coastal waters in the central CCS. The bottom of the 100-m isobath is also indicative of upwelled source water properties [21] and, therefore, of the conditions that eventually modulate coastal exposure to undersaturated events. Physical and biogeochemical water mass properties associated with events are determined by averaging annually over days during which conditions along the bottom of the 100-m isobath were undersaturated. These properties are then individually regressed against event severity to identify variables most closely associated with interannual variability in event properties at each latitude. While averaged meridional wind stress within 50 km from the coast is included in the regression as a proxy for coastal upwelling intensity [18], the influence of regional upwelling dynamics and water mass properties is assessed more extensively by examining the depth and physical and biogeochemical properties associated with the 26.0 kg/m<sup>3</sup> isopycnal ( $\sigma_{26}$ ), a density surface historically considered as representative of upwelled source waters in the central CCS [42]. An EOF analysis is used to isolate the dominant modes of regional variability for meridional wind stress, as well as the depth and DIC content of  $\sigma_{26}$  within 200km from the coast (a representative offshore distance over which regional variability relates to changes in upwelled source waters). Finally, a multiple linear regression model is used to relate the variables identified as important in the analysis to interannual variability of event severity. All analyses are conducted and figures created using Ferret v7.1 (<http://ferret.pmel.noaa.gov/Ferret/>), except for the multiple

linear regression and associated statistical tests done using R (stats, lmtest and zoo packages) [43,444,45].

## 2.4 Results

### 2.4.1 Model Evaluation

The ability of the simulation to reproduce observed variability across the shelf at several latitudes spanning the model domain is evaluated in terms of the agreement between observed and simulated properties via Taylor diagrams (Fig. 2.1, upper panels), and between observed and simulated relationships for two properties via linear regressions (Fig. 2.1, lower panels). Based on the Taylor diagrams, simulated DIC and pH exhibit the closest agreement with in situ measurements, with standard deviation ratios (modeled to observed) of 0.75-1.25 and correlation coefficients above 0.8 at most locations, resulting in root mean square differences (RMSD) of 0.5-1 observed standard deviation (i.e., RMSD are less than 1 observed standard deviation and often close to 0.5 standard deviation). Simulated temperatures correlate well with observations ( $r > 0.7$ ), but are more variable (standard deviation ratios of 1-2), yielding RMSD between 0.5-1.25 observed standard deviations. Simulated and observed TAlk values are more weakly correlated ( $r = 0.3-0.75$ ), but have comparable variability (standard deviation ratios between 0.5-1.25), leading to RMSD in the range of 0.5-1 observed standard deviation. A summary of the statistics for each variable and latitude, along with model bias, is provided in Table S2.1. A least squares regression between temperature and DIC yields  $R^2$  values of 0.75 for the observations, and 0.85 for the model.  $R^2$  values for a regression between DIC and pH

are higher, with 0.91 for observed and 0.99 for simulated values. Regressions of TAlk with DIC and pH reveal weaker relationships, with respective  $R^2$  values of 0.5, 0.22 for the observations, and 0.85 and 0.75 for the model. These comparisons indicate that in both model and observations, DIC explains a substantially greater fraction of pH (and presumably saturation state) variability than TAlk over the coastal region and depths considered here. Overall, the model evaluation demonstrates reasonable agreement between simulated and observed variables, especially for DIC and pH, across the shelf at latitudes (35-42°N) spanning the central CCS. The assessment is consistent with that of Cheresch and Fiechter (2020) based on the same model output and in situ observations, which identified that biogeochemical discrepancies were generally associated with physical conditions not exactly matching the synoptic timing of upwelling along transects.



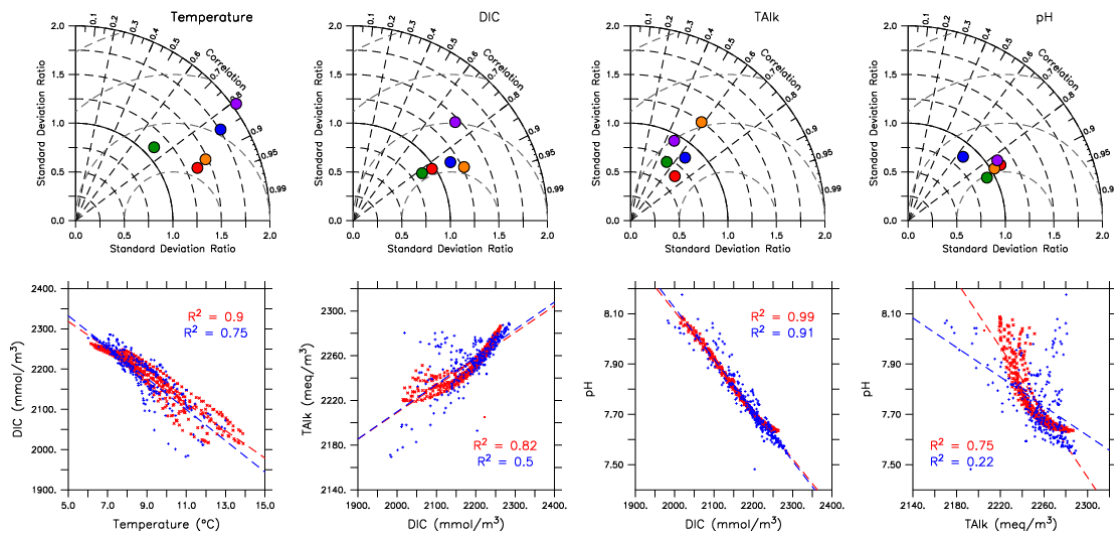


Figure 2.1 Simulated and observed conditions during the 2007 WCOA Cruise. Top panels: Taylor diagrams for (from left to right) temperature, DIC, TAlk, and pH along transect lines at 35°N (purple), 37°N (orange), 38°N (blue), 40°N (green), and 42°N (red). Radial distance corresponds to the ratio of simulated to observed standard deviations and azimuthal angle corresponds to model-observation correlation. Dashed concentric circles centered at (1, 1) denote root mean square difference normalized by observed standard deviation (0.5 increments). Bottom panels: simulated (red) and observed (blue) relationships for (from left to right) temperature vs. DIC, DIC vs. TAlk, DIC vs. pH, and TAlk vs. pH. Dashed lines indicate least-square linear fit for model and observations and corresponding  $R^2$  values are listed in each panel. Both Taylor diagrams and regressions are based on the 4 stations closest to the coast along each transect line and restricted to values in the 0-300m depth range. Observations are synoptic values and simulated values represent means over the cruise period for the Taylor diagram and daily means for the regressions.

For nearshore moorings, in situ pH values generally fall within the range of simulated climatological values, and simulated mean climatological pH values track the observed seasonal cycle at all locations (Fig. 2.2). The observed climatological monthly mean falls within simulated minimum and maximum climatological values. In most cases, the observed monthly mean is contained within one simulated climatological standard deviation from the model monthly climatological mean. The model's ability to reproduce monthly pH variability (in a climatological sense) also extends to temperature and dissolved oxygen (Fig. S2.1). Frequency histograms of low pH ( $< 7.7$ ) event severity at each site indicate that simulated and observed range and distribution of severity values are consistent, with the highest proportion of

events having low severity (Fig. 2.2). Furthermore, the alongshore pattern in frequency distributions for event severity is similar between model and observations, with more frequent and higher severity events occurring at northern sites (Van Damme and Point Arena) relative to southern sites (Big Creek and Point Buchon). Because severity is calculated using intensity and duration, the model-data agreement extends to these properties as well (Fig. S2.2).

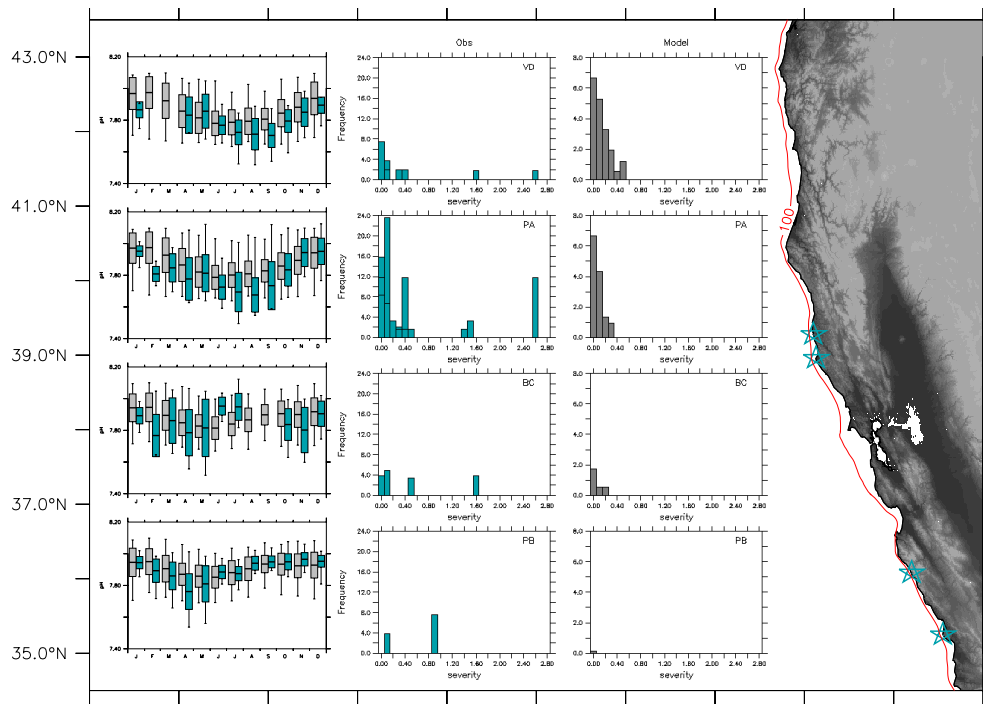


Figure 2.2 Simulated (1988-2010) and observed (2017-2019) pH at nearshore moorings indicated by blue stars on map at right (Van Damme (39.27°N, -123.80°W), Point Arena (38.95°N, -123.74°W), Big Creek (36.0°N, -121.60°W) and Point Buchon (35.24°N, -120.9°W); red line denotes 100-m isobath). (Left) Monthly climatological mean, standard deviation and minimum/maximum values represented by box and whisker plots for observed (blue) and simulated (gray) pH values. (Middle and Right) Frequency histograms of observed and simulated severity of low pH events (pH < 7.7) per year at each location. Map created using Ferret v7.1 (<http://ferret.pmml.noaa.gov/Ferret/>).

#### 2.4.2 Spatiotemporal variability of undersaturation events

Exposure to undersaturated conditions along the 100-m isobath varies strongly with depth, latitude, and time (Fig. 2.3 and Fig. S2.3). Near the surface, there are locations where no events occur throughout the entire simulation; where events occur, they typically have low intensity, short duration, and low severity. At depths below 60 m, events occur at every latitude and are most intense, longest, and most severe near the bottom.

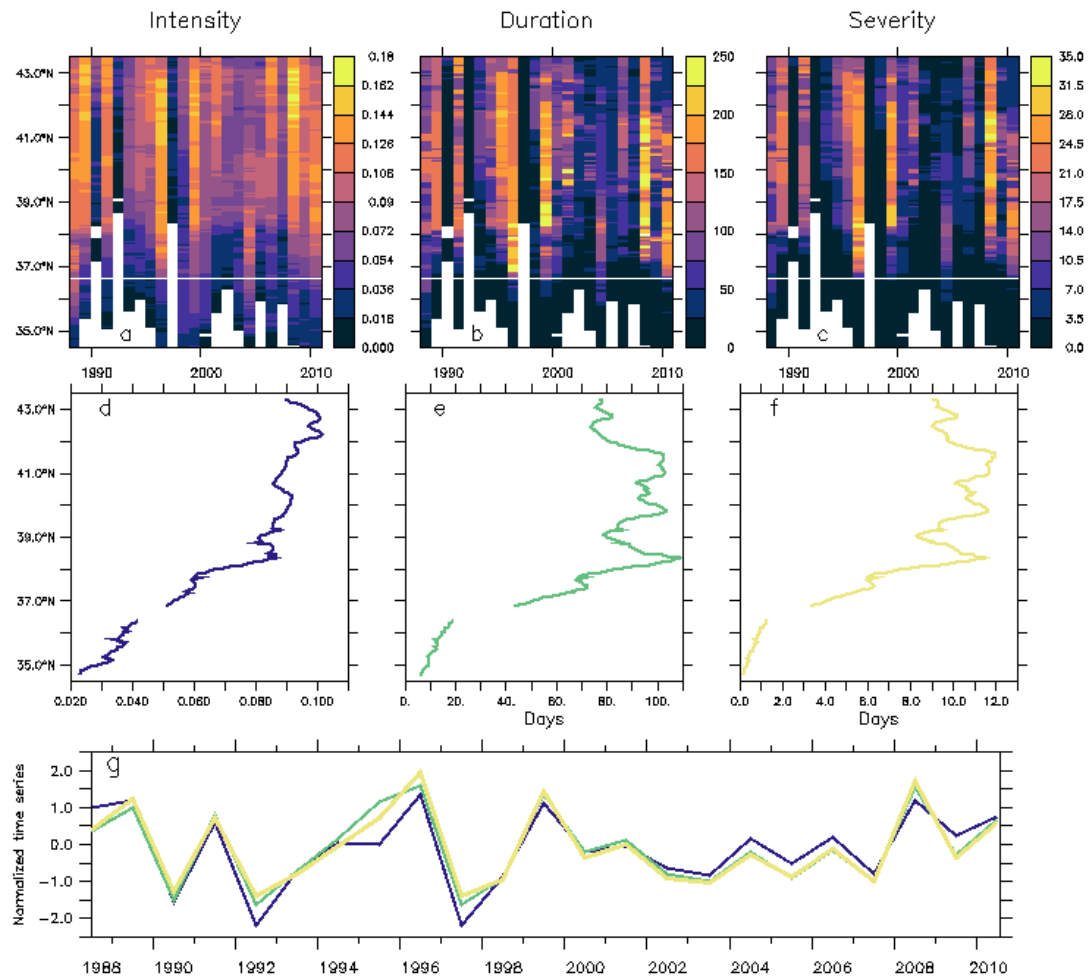


Figure 2.3 Simulated aragonite undersaturation ( $\Omega_{arag} < 1$ ) event properties during the upwelling season (May-September) along the bottom of the 100-m isobath. (Top) Annual mean intensity (a), duration (b) and severity (c). (Middle) 1988-2010 mean event intensity (d), duration (e) and severity (f) as a function of latitude. (Bottom) Standardized annual mean event intensity (blue), duration (green) and severity (yellow) averaged over latitude (34.5-43.5°N).

Along the bottom of the 100-m isobath, exposure to undersaturated conditions in the central CCS is most significant during the period of strongest coastal upwelling favorable conditions (May-September, hereafter referred to as “upwelling season”) (Fig. S2.3). Event properties along the bottom of the 100-m isobath exhibit strong interannual variability, with years of low intensity, duration and severity (e.g., 1992 and 1997), and years experiencing prolonged undersaturation (e.g., 1999 and 2008)

(Fig. 2.3a-c). Based annual upwelling season averages, intensity ranges from 0.0-0.2 (corresponding to average  $\Omega_{\text{arag}}$  of 1.0-0.8), and average duration and severity ranges from 1-258 days and 0-34 days, respectively. While simulated events occur at all latitudes, they are more intense, longer lasting, and therefore more severe, north of 37°N. The alongshore and temporal properties of these events also indicate a strong covariability of intensity, duration, and severity (Fig. 2.3d-g).

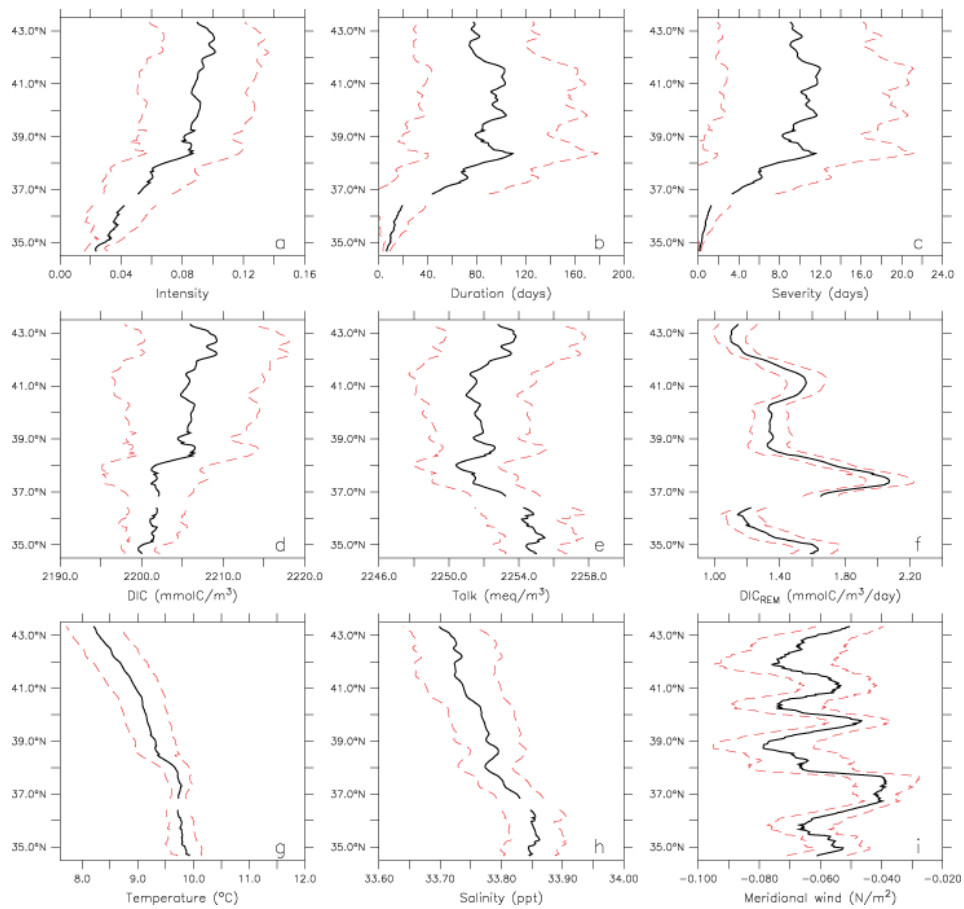


Figure 2.4 Upwelling-season mean (black lines) and standard deviation (red dashed lines) of event properties and associated water mass characteristics during events (i.e. when  $\Omega_{\text{arag}} < 1$ ). (Top) Event intensity (a), duration (b), and severity (c). (Middle) DIC (d), TALK (e), and rate of DIC production from remineralization ( $DIC_{\text{REM}}$ ) (f). (Bottom) Temperature (g), salinity (h), and meridional wind stress averaged 0-50km offshore (i).

Temporal means and standard deviations demonstrate that interannual variability greatly exceeds (by as much as a factor of 2-3) alongshore variations over the region where undersaturated conditions occur most frequently (i.e., 38-43°N). Average water mass properties during undersaturated conditions along the bottom of the 100-m isobath indicate alongshore similarities between event properties and DIC and TAlk (Fig. 2.4). In contrast, alongshore patterns of temperature, salinity, and DIC contribution from remineralization ( $DIC_{REM}$ ) bear less resemblance with event properties. Pairwise linear regressions between event severity and water mass properties during events indicate that DIC explains the largest fraction of the interannual variability in event severity ( $R^2$  of 0.7-0.9 in regions of high event severity north of 37°N) (Fig. 2.5, left panel). In contrast, TAlk and  $DIC_{REM}$  independently explain less than 50% of interannual variance in event severity, except for a narrow range of latitudes between 40-41°N where  $R^2$  values for TAlk increase to ~0.7 (but still lower than the  $R^2$  values for DIC of ~0.9 over the same range of latitudes). For physical variables, temperature is generally not a good predictor of event severity ( $R^2 < 0.3$ ) and the explanatory power of meridional (upwelling favorable) wind stress is limited to latitudes ranging between 38-41°N and explains 30-50% of the interannual variance in event severity (Fig. 2.5, right panel).

The emergence of DIC as the dominant driver of year-to-year variations in undersaturated conditions along the bottom of the 100-m isobath at all latitudes based on the regressions is consistent with the strong simulated and observed relationship between DIC and pH (and presumably  $\Omega_{arag}$ ) in coastal waters of the central CCS

(see Fig. 2.1). While TAlk,  $DIC_{REM}$ , and meridional wind stress can locally explain a non-trivial fraction of the event severity variance, their importance consistently falls below that of DIC. The dominance of DIC as the driver of interannual variability in  $\Omega_{arag}$  is further confirmed with a sensitivity study following Turi et al. 2018 (Table S2.2). DIC explains on average 75% of the interannual variability (approximately 80% at 35°N decreasing roughly linearly to 70% at 43°N), while TAlk explains roughly 20% of variability in  $\Omega_{arag}$  (Fig. S2.4). Temperature has a small ( $\sim 5\%$ ) impact on  $\Omega_{arag}$ , and salinity's contribution is negligible.

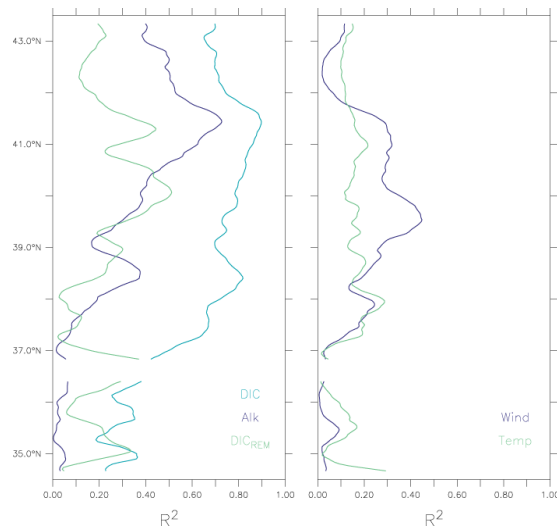


Figure 2.5 Relationships between event severity and water mass properties during undersaturated conditions ( $\Omega_{arag} < 1$ ) along the bottom of the 100-m isobath based on upwelling season means. (Left)  $R^2$  values between severity and DIC (blue line), severity and total TAlk (green line), and severity and  $DIC_{REM}$  (purple line). (Right)  $R^2$  values between severity and meridional wind stress (purple line) and severity and temperature (green line). All values are from the bottom of the 100-m isobath, except meridional wind stress, which represents a 0-50km offshore average.

DIC and TAlk budgets were also constructed to identify the physical (advection and mixing) and biogeochemical (remineralization, calcium carbonate

dissolution, and nitrification) processes controlling changes in these properties along the bottom of the 100-m isobath. Advection emerges as the dominant mechanism influencing interannual variability in DIC and TAlk during the upwelling season, with average contributions at most latitudes greater than any other process by at least two orders of magnitude (Fig. S2.5).

#### 2.4.3 Drivers of undersaturation events

Possible mechanisms through which DIC concentrations along the bottom of the 100-m isobath can vary interannually are: (1) changes in upwelling intensity, whereby weaker or stronger upwelling would lead to lower or higher DIC concentrations, and (2) changes in DIC concentrations near the source depth of upwelled water independently of upwelling intensity.

To explore the relative importance of changes in upwelling intensity vs. changes in upwelled source water DIC content (associated with anomalous transport of water masses), regional variations of the two following properties are considered: (1) depth of  $\sigma_{26}$  as a proxy for changes in upwelling intensity, and (2) DIC concentrations on  $\sigma_{26}$  as a proxy for changes in upwelled source water properties. The depth of  $\sigma_{26}$  is commonly used in the central CCS to track the source depth of upwelled waters and upwelling strength, and is approximately 50-60 m during the upwelling season along the 100-m isobath (Fig. S2.6). The first EOF mode for DIC concentrations on  $\sigma_{26}$  explains 52% of the variance and is characterized by a broad, regional pattern with higher variability in the northern part of the domain (i.e., where events are most severe) (Fig. 2.6). The temporal amplitude of this mode exhibits



primarily low-frequency variability, with positive and negative anomalies lasting ~3-7 years and resembling the Pacific Decadal Oscillation. Positive DIC anomalies correspond with positive phases of the PDO, and vice versa, although with an apparent lag of ~1 year. The first EOF mode for the depth of  $\sigma_{26}$  explains 35% of the variance and exhibits a predominantly coastal signal. The temporal variability of this mode is dominated by interannual variability and aligns with the temporal amplitude of the first EOF mode for meridional wind-stress averaged within 50 km of the coast.

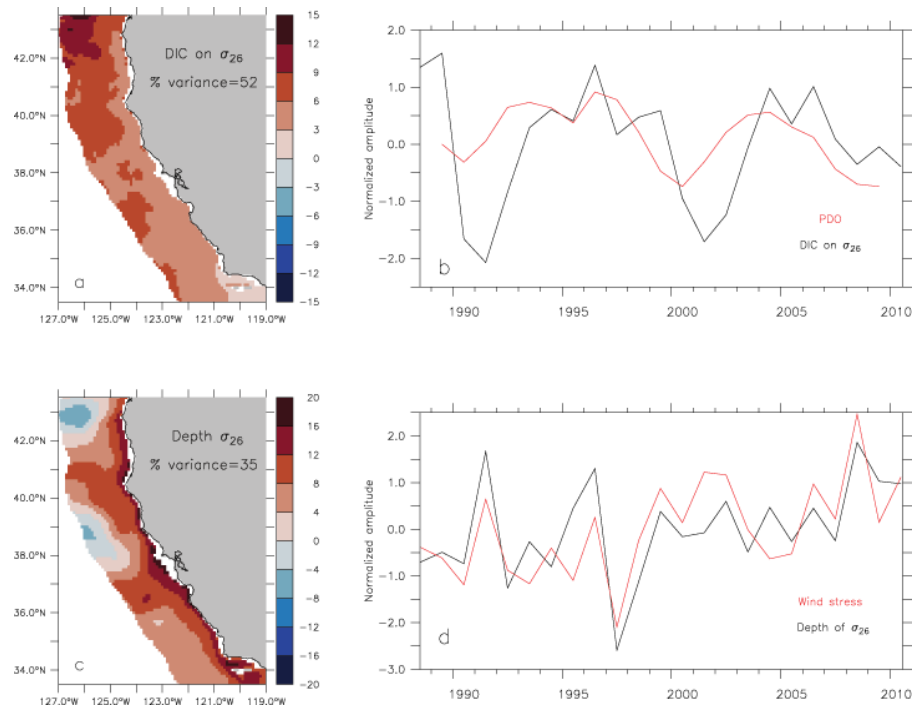


Figure 2.6 Leading EOF mode of interannual variability for the DIC content (top) and depth of  $\sigma_{26}$  (bottom) based on upwelling season averages and restricted to 0-200km offshore. (a) Spatial patterns of EOF mode 1 for  $\sigma_{26}$  DIC content ( $\text{mmolC/m}^3$ ). (b) Temporal amplitude of EOF mode 1 for  $\sigma_{26}$  DIC content (black line), and 3-year running mean of Pacific Decadal Oscillation (PDO) index (red line) (<https://www.ncdc.noaa.gov/teleconnections/pdo/>). (c) Spatial pattern of EOF mode 1 for  $\sigma_{26}$  depth (m); positive values indicate shallower depths. (d) Temporal amplitude of EOF mode 1 for  $\sigma_{26}$  depth (black line) and temporal amplitude of EOF mode 1 for meridional wind stress averaged within 50km of the coast (red line). Maps created using Ferret v7.1 (<http://ferret.pmel.noaa.gov/Ferret/>).

While the first EOF mode for the depth of  $\sigma_{26}$  is clearly related to meridional wind stress and interannual variations in upwelling intensity (i.e., shallower isopycnal depths occur during years of stronger upwelling), the regional patterns associated with the first EOF mode for DIC on  $\sigma_{26}$  warrant further examination. The low frequency variability of the mode, and apparent relationship to the PDO, suggest a connection to changes in the intensity of the subtropical gyre circulation and water mass advection into the central CCS. Upwelling-season mean meridional velocities and spice calculated at the depth of  $\sigma_{26}$  and separately averaged for years of positive and negative amplitudes of the first EOF mode for DIC (see Fig. 2.6b) verify this hypothesis. During positive phases of the first EOF mode, DIC at the depth of  $\sigma_{26}$  is, as expected, higher over the entire region (Fig. 2.7a). The difference in DIC concentrations between positive and negative phases ranges from approximately -5 to 30 mmolC/m<sup>3</sup> (Fig. 2.7d). The largest positive differences occur north of 37°N, which is consistent with the spatial patterns of mode 1 indicating the highest variability in the northern part of the domain (see Fig. 2.6a). Similar differences (positive vs. negative DIC phases) for meridional velocities and spice (Fig. 2.7b-c, e-f) clearly indicate that the regional increase in DIC concentrations is associated with an equivalent increase in poleward velocities and spice on  $\sigma_{26}$ , pointing to a strengthening of northward transport of Pacific Equatorial Waters (which have higher spice and DIC content on  $\sigma_{26}$  than Pacific Subarctic Upper Waters) in the central CCS. An increased contribution of Pacific Equatorial Waters to the region is also

consistent with a weakening of the subtropical gyre circulation and, therefore, a positive phase of the PDO.

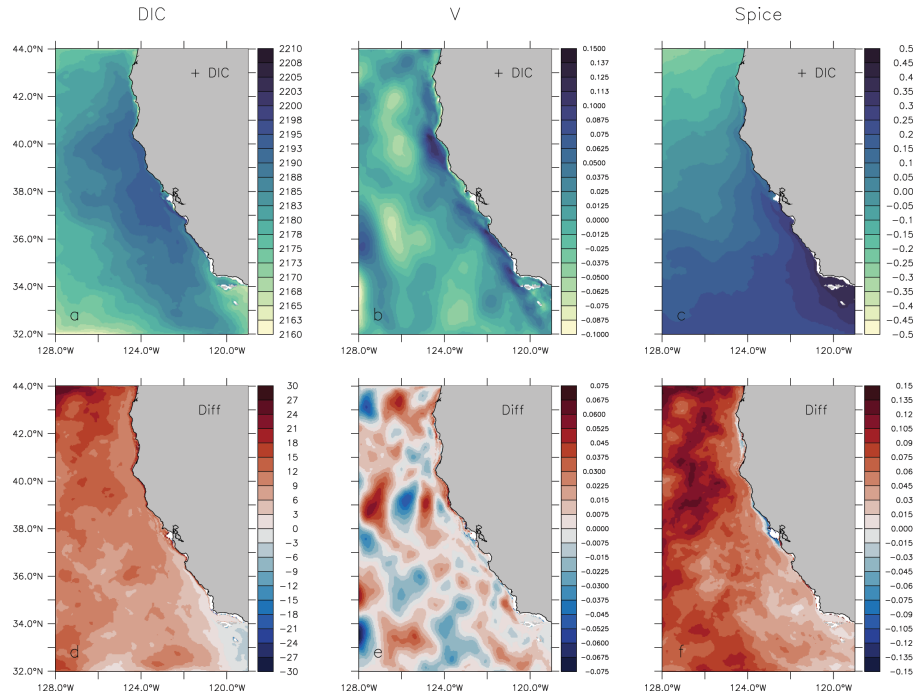


Figure 2.7 Environmental conditions during periods of increased DIC content on  $\sigma_{26}$ . (Top) Upwelling-season mean DIC concentrations (mmolC/m<sup>3</sup>) (a), meridional velocity (m/s) (b), and spice (kg/m<sup>3</sup>) (c) on  $\sigma_{26}$  during positive phases of the first EOF mode for DIC. (Bottom) Upwelling-season mean DIC (mmolC/m<sup>3</sup>) (d), meridional velocity (m/s) (e), and spice (kg/m<sup>3</sup>) (f) differences between positive and negative phases of the first EOF mode for DIC. Maps created using Ferret v7.1 (<http://ferret.pmel.noaa.gov/Ferret/>).

The combined effect of low frequency changes in DIC content near the depth of upwelled source waters and higher frequency variability associated with interannual changes in coastal upwelling intensity on undersaturated event properties along the bottom of the 100-m isobath is further quantified via a multiple linear regression (MLR). Using upwelling season alongshore mean values for the depth of  $\sigma_{26}$  (as a proxy for upwelling intensity) and DIC concentrations on  $\sigma_{26}$  (as a proxy for upwelled source water content) as explanatory variables and log severity as a

response variable, a MLR given by  $\log(\text{severity}) = -195.06754 + 0.12333 (\sigma_{26}) + 0.09645 ([\text{DIC}])$  yields a multiple  $R^2$  value of 0.66, and a p-value of  $1.967\text{e-}05$  (Fig. S2.5). Regressions between event severity and the two explanatory variables indicate that, individually, the depth of  $\sigma_{26}$  explains 43% of interannual variability in severity, and DIC concentrations on  $\sigma_{26}$  explains 9% of interannual variability in severity (Table S2.3).

## 2.5 Discussion

Previous work has identified a region-wide susceptibility to ocean acidification in the CCS, and the present study describes recent spatiotemporal patterns and drivers of exposure to undersaturated conditions. The results demonstrate that event intensity, duration, and severity in the central CCS exhibit substantial interannual variability governed by changes in the strength of coastal upwelling and DIC concentrations in upwelled source waters.

Comparison of simulated pH, dissolved oxygen, and temperature against observed data from nearshore moorings indicates the model reproduces, in a climatological sense, natural variability experienced in coastal waters on monthly time scales. Episodic excursions of observed pH below the minimum simulated values are attributed to a model bias towards higher pH levels near the source depth of upwelled water identified in previous evaluations [19]. The tendency of the model to simulate slightly higher than observed pH values suggests that the present assessment of exposure to undersaturated conditions is likely conservative and provides lower bounds for event properties. While noticeable differences exist in the

magnitude of pH values, the alongshore pattern of event occurrence and overall magnitude of event properties are generally consistent between the model and observations. The focus of the present study is to identify dominant drivers of interannual event variability rather than provide exact estimates of event properties in terms of their magnitude. As such, the interpretation relies on regional spatial and temporal patterns to describe event properties along the 100-m isobath, while in reality there are additional physical and biogeochemical mechanisms, such as tidal mixing and benthic processes, that will further influence event properties at the local scale of nearshore environments. The lack of a global anthropogenic signal in the model boundary conditions and the relatively short simulation period also preclude any conclusions about trends in corrosive events from the present analyses.

A distinct separation between the northern and southern regions of the central CCS is apparent in the alongshore pattern of event properties, such that intensity, duration, and severity values are lower south of 37°N, and higher north of 37°N. The region of higher event severity north of 37°N corresponds to latitudes experiencing overall higher mean DIC concentrations and lower mean TAlk relative to the region south of 37°N. While DIC is the variable most closely associated with interannual variability in event severity over the range of latitudes considered here, other variables, such as TAlk, organic matter remineralization, and meridional wind stress, may locally influence the alongshore pattern and temporal variability of event properties. For example, the fraction of interannual variance in event severity explained independently by TAlk and remineralization substantially increases in the

region of higher primary production south of Cape Blanco (41-42°N; as identified in Cheresch and Fiechter (2020) and evidenced by higher POC remineralization rates in Fig. 2.4). The importance of DIC over TAlk in shaping the interannual response of  $\Omega_{\text{arag}}$  was confirmed with a sensitivity analysis, and is consistent with Turi et al., 2018, who also found DIC to be the dominant variable driving changes in pH within 100 km from the coast in the central CCS. The results presented here do not contradict previous work identifying the role of remineralization in reducing  $\Omega_{\text{arag}}$  at depth in the CCS [9], but rather establish that it has limited explanatory power for year-to-year variability in event intensity. Based on the interannual variability of simulated remineralization rates during events at the bottom of the 100-m isobath (standard deviation of  $\sim 0.2 \text{ mmolC/m}^3/\text{day}$ ; Fig. 2.4), it would take the full average duration of an event ( $\sim 80$  days; Fig. 2.4) to create a DIC change comparable to the interannual DIC variability during events (standard deviation of  $\sim 10 \text{ mmolC/m}^3$ ; Fig. 2.4). Furthermore, when DIC content in upwelled source waters is regionally elevated, contributions from remineralization within 200 km of the coast are on average lower (Fig. S2.4), suggesting a reduction in the supply of DIC from export production and a mitigating effect on undersaturation events. DIC and TAlk budgets were also constructed to dissociate physical and biogeochemical contributions, and revealed that advection is the dominant process (by at least two orders of magnitude) impacting the interannual variability of DIC and TAlk during the upwelling season along the bottom of the 100-m isobath. While this finding confirms that interannual variations in coastal upwelling intensity and DIC content in upwelled source waters

are the primary processes controlling the onset and intensity of undersaturation events during the upwelling season, remineralization may prolong the duration of events at alongshore locations where enhanced primary production and vertical export occur. Additional mechanisms may also shape the alongshore properties of events at finer spatial scales, such as variations in upwelling intensity and duration as well as regional circulation patterns [19].

Based on the leading EOF mode for DIC concentrations on  $\sigma_{26}$  within 200 km of the coast, more than half of DIC variance is related to a low-frequency, regional signal that contributes differences up to 30-40 mmolC/m<sup>3</sup> between periods of increased and decrease DIC (Fig. 2.6 and 2.7) in the northern domain. The temporal amplitude of this EOF mode resembles the Pacific Decadal Oscillation index. When the EOF amplitude and PDO index are positive, higher DIC concentrations occur on  $\sigma_{26}$  in combination with spicier waters and increased northward velocities. The connection to the PDO and co-occurrence of higher DIC concentrations, higher spice values, and increased poleward transport at depth point toward a change in water mass composition of the central CCS. This interpretation is consistent with a previous water mass analysis based on observations collected near 34.5°N, which concluded that 1996 (a year with higher simulated DIC content) had a lower fraction (~40%) of PSUW at 100-m depth, while 2008 (a year with lower simulated DIC content) had a higher fraction (~70%) of PSUW at the same depth [46]. While a temporal lag is expected between change in the intensity of the subtropical gyre circulation and changes in water mass composition in the coastal regions of the central CCS, the 1-

year lag between the PDO and simulated DIC concentrations on  $\sigma_{26}$  (Fig. 2.6) may be an artifact of averaging annually, such that any lag would be artificially amplified to one year.

The regional patterns and variability of DIC content in upwelled source waters cannot alone explain event severity, however. For example, in 1997, anomalously low event severity occurred alongside above average regional DIC concentrations. In contrast, simulated events in 2008 were anomalously severe, despite average regional DIC concentrations. Therefore, it is not only the DIC content in upwelled source waters, but also the strength of upwelling that dictates event severity. The first EOF mode for the depth of  $\sigma_{26}$  exhibits a coastal signature with high-frequency temporal variability associated with the leading mode of variability for meridional (upwelling-favorable) wind stress, thereby suggesting that interannual variability in the depth of  $\sigma_{26}$  within 200 km of the coast is primarily governed by changes in coastal upwelling intensity. When regional DIC is high and average to above average winds occur (e.g., 1996 and 1999), high DIC waters are upwelled and severe events happen. However, elevated regional DIC superimposed to below average upwelling intensity is not by itself sufficient to produce undersaturated conditions along the shelfbreak. This finding suggests that, based on the 1988-2010 period, average or above average upwelling-favorable wind stress is a necessary condition for high severity events to occur. In contrast, anomalously strong upwelling-favorable wind stress alone can lead to severe events despite below average DIC concentrations in upwelled source waters (i.e., during a negative PDO phase). These results highlight the various



pathways by which low to high severity events can occur in the central CCS (Fig. 2.8).

It is worth noting that during positive phases of the PDO, when regional DIC concentrations are elevated, upwelling-favorable wind stress tends to be weaker (Fig. 2.6), which is consistent with reductions in upwelling strength during positive phases of the PDO, and vice versa [24]. Over the 23-year simulation, there are few instances when high regional DIC co-occurred with strong upwelling conditions, suggesting a potential compensatory effect of reduced upwelling during years of anomalously high regional DIC, theoretically mitigating the severity of undersaturation events in the central CCS.

Turi et al. (2018) established a relationship between basin-scale climate variability and nearshore pH variability in the CCS [46]. Specifically, ENSO variations were linked to changes in water mass composition and primary productivity, which regionally modulated exposure to low pH. Turi et al. (2018) also demonstrated that La Niña events correspond to anomalously low pH and DIC below ~100 m. While the present results corroborate that ENSO variability plays a role in driving interannual variability in event severity (e.g., 1989, 1996, 1999, and 2008 all have above average event severity and correspond with moderate to strong La Niña conditions), it cannot by itself explain the simulated interannual variability in event severity. For example, moderate to strong La Niña events occurred in 2000, 2006 and 2009, but resulted in below average simulated event severity, suggesting that a moderate to strong La Niña event (and associated changes in water mass composition

and coastal upwelling intensity) may not solely dictate undersaturation events at 100-m depth. It is more likely that interannual modes of variability modulating physical and biogeochemical properties in the central CCS, such as ENSO, superimpose on lower frequency modes of basin-scale variability, such as the PDO, and potentially exacerbate or mediate exposure to undersaturated conditions.

The present study builds on the work of Hauri et al. (2013), in which changes to simulated event properties from the preindustrial era through 2050 were quantified under a high-emissions scenario [27]. Event properties calculated here are higher than those reported in Hauri et al. (2013) for the 5-year time period approximating 2010. The discrepancy could be attributed to wind forcing differences between the two simulations. Hauri et al. (2013) used climatological wind forcing, which likely underestimates synoptic variability and, therefore, the intensity of coastal upwelling events. Additionally, Hauri et al. (2013) reported a model bias towards higher  $\Omega_{\text{arag}}$  and noted that this could lead to an underestimation of event duration. Furthermore, the present analysis focuses on events along the bottom of the 100-m isobath, whereas Hauri et al. (2013) included shallower shelf regions where events may be shorter and less intense, reducing spatially-averaged event property statistics.

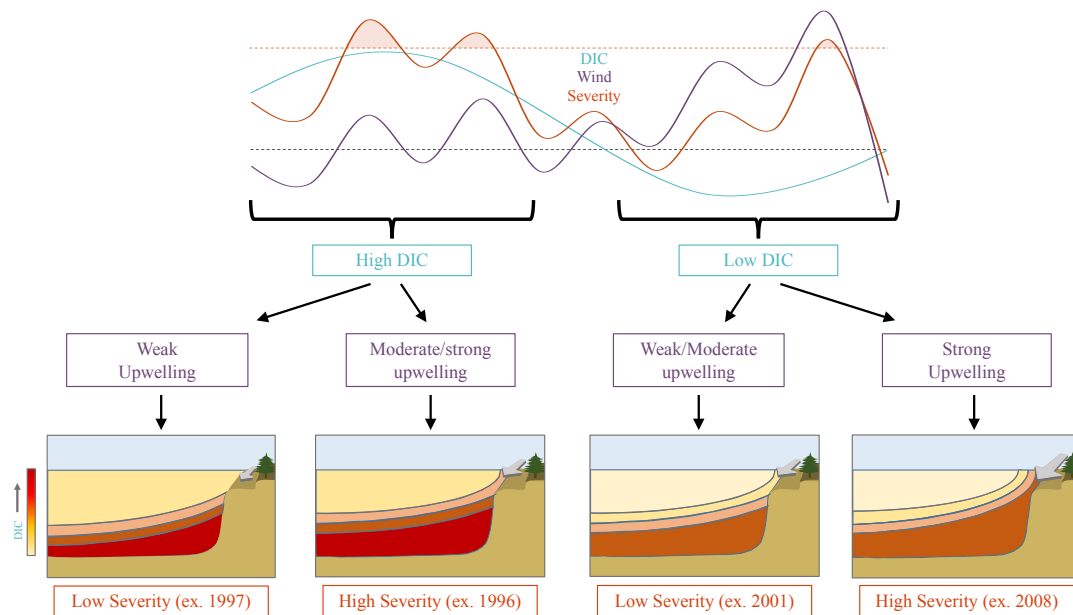


Figure 2.8 Conceptual flow diagram of undersaturation ( $\Omega_{arag} < 1$ ) event severity and its drivers in the central California Current System. (Top) Theoretical time series of dissolved inorganic carbon (DIC) concentration (blue), upwelling-favorable wind stress (purple) and event severity (orange), with the dashed gray and dashed orange lines representing a theoretical mean and one standard deviation, respectively, and the shaded orange regions representing “extreme” events. (Bottom) Conceptual cross-sections of the upwelling-dominated coastal region, with gray lines indicating theoretical density surfaces, color shading indicating concentration of DIC, and gray alongshore arrow size representing the relative strength of upwelling-favorable winds.

The current findings have important implications for marine species and ecosystems in upwelling regions. In the CCS, exposure to undersaturated conditions has been linked to shell or carapace dissolution of ecologically important species [10, 11]. Most observational studies examining the ecological effects of ocean acidification have necessarily related snapshots of organisms’ conditions to concurrent conditions. However, the duration, intensity and severity of exposure is likely important in governing species’ responses. The effects of exposure to low  $\Omega_{arag}$  and pH conditions are likely to differ with intensity (e.g., increasingly deleterious effects with increasing intensities [48]). Thus, the results detailed here add

to a growing body of evidence that the impacts of ocean acidification along the U.S. west coast will not be experienced uniformly with latitude and vary significantly from year to year. The mechanistic exploration of the drivers of events in high-resolution model simulations provides a valuable framework for identifying geographic hotspots or oceanographic conditions (e.g., PDO) associated with increased vulnerability to ocean acidification at local and regional scales.

## 2.6 Acknowledgments

This research was funded primarily by grants OCE-1566623 and OCE-1635315 from the National Science Foundation Division of Ocean Sciences, with additional support from NOAA grant NA19OAR0170357 and California Sea Grant College Program Project R/HCE-29F. Any opinions, findings, and conclusions or recommendations expressed here are those of the authors and do not necessarily reflect the views of the National Science Foundation, NOAA, California Sea Grant or the U.S. Dept. of Commerce. The observational data was supported by the California Ocean Protection Council Grant (C0302200). We thank three anonymous reviewers for their thorough and constructive comments.

## 2.7 Data Availability Statement

The model output used to complete the analysis has been deposited on Dryad (<https://datadryad.org/stash/share/nZwBAOZpOpv-HunYw684CoJ8jCCOCom9XaoU0HwSaeI>). The observational data will be made available on the data platform for CenCOOS (<https://data.caloos.org/>). Contact the

corresponding author to request additional information about or access to the datasets used in this study.

## 2.8 References

1. Friedlingstein, P. *et al.* Global Carbon Budget 2021. *Earth Syst. Sci. Data* **14**, 1917–2005 (2022).
2. Kroeker, K. J. *et al.* Impacts of ocean acidification on marine organisms: quantifying sensitivities and interaction with warming. *Global Change Biology* **19**, 1884–1896 (2013).
3. Gruber, N. *et al.* Rapid Progression of Ocean Acidification in the California Current System. *Science* **337**, 220–223 (2012).
4. Hauri, C. *et al.* Ocean acidification in the California Current System. *Oceanography* **22**, 60–71 (2009).
5. Huyer, A. Coastal upwelling in the California current system. *Progress in Oceanography* **12**, 259–284 (1983).
6. Jacox, M. G., Moore, A. M., Edwards, C. A. & Fiechter, J. Spatially resolved upwelling in the California Current System and its connections to climate variability. *Geophysical Research Letters* **41**, 3189–3196 (2014).
7. Feely, R. A., Sabine, C. L., Hernandez-Ayon, J. M., Ianson, D. & Hales, B. Evidence for Upwelling of Corrosive ‘Acidified’ Water onto the Continental Shelf. *Science* **320**, 1490 (2008).
8. Feely, R. A. *et al.* The combined effects of acidification and hypoxia on pH and aragonite saturation in the coastal waters of the California current

- ecosystem and the northern Gulf of Mexico. *Continental Shelf Research* **152**, 50–60 (2018).
9. Feely, R. A. *et al.* Chemical and biological impacts of ocean acidification along the west coast of North America. *Estuarine, Coastal and Shelf Science* **183**, 260–270 (2016).
  10. Bednaršek, N. *et al.* Systematic review and meta-analysis toward synthesis of thresholds of ocean acidification impacts on calcifying pteropods and interactions with warming. *Front. Mar. Sci.* **6**, 227 (2019).
  11. Bednaršek, N. *et al.* Exoskeleton dissolution with mechanoreceptor damage in larval Dungeness crab related to severity of present-day ocean acidification vertical gradients. *Science of The Total Environment* **716**, 136610 (2020).
  12. Harris, K. E., DeGrandpre, M. D. & Hales, B. Aragonite saturation state dynamics in a coastal upwelling zone. *Geophysical Research Letters* **40**, 2720–2725 (2013).
  13. Juranek, L. W. *et al.* A novel method for determination of aragonite saturation state on the continental shelf of central Oregon using multi-parameter relationships with hydrographic data. *Geophysical Research Letters* **36**, (2009).
  14. Chan, F. *et al.* Persistent spatial structuring of coastal ocean acidification in the California Current System. *Scientific Reports* **7**, 2526 (2017).

15. Barth, J. A., Pierce, S. D. & Smith, R. L. A separating coastal upwelling jet at Cape Blanco, Oregon and its connection to the California Current System. *Deep Sea Research Part II: Topical Studies in Oceanography* **47**, 783–810 (2000).
16. Pickett, M. H. & Paduan, J. D. Ekman transport and pumping in the California Current based on the US Navy’s high—Resolution atmospheric model (COAMPS). *J. Geophys. Res. Oceans* **108**(C10), 3327 (2003).
17. Kudela, R. M. *et al.* New Insights into the Controls and Mechanisms of Plankton Productivity in Coastal Upwelling Waters of the Northern California Current System. *Oceanography* **21**, 46–59 (2008).
18. Fiechter, J., Edwards, C. A. & Moore, A. M. Wind, Circulation, and Topographic Effects on Alongshore Phytoplankton Variability in the California Current. *Geophysical Research Letters* **45**, 3238–3245 (2018).
19. Cheres, J. & Fiechter, J. Physical and Biogeochemical Drivers of Alongshore pH and Oxygen Variability in the California Current System. *Geophysical Research Letters* **47**, e2020GL089553 (2020).
20. Schwing, F. B., Murphree, T., deWitt, L. & Green, P. M. The evolution of oceanic and atmospheric anomalies in the northeast Pacific during the El Niño and La Niña events of 1995–2001. *Progress in Oceanography* **54**, 459–491 (2002).

21. Jacox, M. G., Fiechter, J., Moore, A. M. & Edwards, C. A. ENSO and the California Current coastal upwelling response. *Journal of Geophysical Research: Oceans* **120**, 1691–1702 (2015).
22. Mantua, N. J. & Hare, S. R. The Pacific Decadal Oscillation. *Journal of Oceanography* **58**, 35–44 (2002).
23. Chavez Francisco P., Ryan John, Lluch-Cota Salvador E., & Ñiquen C. Miguel. From Anchovies to Sardines and Back: Multidecadal Change in the Pacific Ocean. *Science* **299**, 217–221 (2003).
24. Di Lorenzo, E. *et al.* North Pacific Gyre Oscillation links ocean climate and ecosystem change. *Geophysical Research Letters* **35**, (2008).
25. Chenillat, F., Rivière, P., Capet, X., Di Lorenzo, E. & Blanke, B. North Pacific Gyre Oscillation modulates seasonal timing and ecosystem functioning in the California Current upwelling system. *Geophysical Research Letters* **39**, (2012).
26. Brady, R. X., Lovenduski, N. S., Yeager, S. G., Long, M. C. & Lindsay, K. Skillful multiyear predictions of ocean acidification in the California Current System. *Nature Communications* **11**, 2166 (2020).
27. Hauri, C., Gruber, N., McDonnell, A. M. P. & Vogt, M. The intensity, duration, and severity of low aragonite saturation state events on the California continental shelf. *Geophysical Research Letters* **40**, 3424–3428 (2013).



28. Hauri, C. *et al.* Spatiotemporal variability and long-term trends of ocean acidification in the California Current System. *Biogeosciences* **10**, 193–216 (2013).
29. Siedlecki, S. A. *et al.* Experiments with Seasonal Forecasts of ocean conditions for the Northern region of the California Current upwelling system. *Scientific Reports* **6**, 27203 (2016).
30. Siedlecki, S. A. *et al.* Coastal processes modify projections of some climate-driven stressors in the California Current System. *Biogeosciences* **18**, 2871–2890 (2021).
31. Haidvogel, D. B. *et al.* Ocean forecasting in terrain-following coordinates: Formulation and skill assessment of the Regional Ocean Modeling System. *Journal of Computational Physics* **227**, 3595–3624 (2008).
32. Shchepetkin, A. F. & McWilliams, J. C. The regional oceanic modeling system (ROMS): a split-explicit, free-surface, topography-following-coordinate oceanic model. *Ocean Modelling* **9**, 347–404 (2005).
33. Atlas, R. *et al.* A Cross-calibrated, Multiplatform Ocean Surface Wind Velocity Product for Meteorological and Oceanographic Applications. *Bulletin of the American Meteorological Society* **92**, 157–174 (2011).
34. Carton, J. A., Chepurin, G. & Cao, X. A Simple Ocean Data Assimilation Analysis of the Global Upper Ocean 1950–95. Part II: Results. *Journal of Physical Oceanography* **30**, 311–326 (2000).

35. Kishi, M. J. *et al.* NEMURO—a lower trophic level model for the North Pacific marine ecosystem. *Ecological Modelling* **202**, 12–25 (2007).
36. Fennel, K., Wilkin, J., Previdi, M. & Najjar, R. Denitrification effects on air-sea CO<sub>2</sub> flux in the coastal ocean: Simulations for the northwest North Atlantic. *Geophysical Research Letters* **35**, (2008).
37. Conkright, M. E. *et al.* World ocean atlas 2001 : objective analyses, data statistics, and figures : CD-ROM documentation. (2002).
38. Key, R. *et al.* A global ocean carbon climatology: Results from Global Data Analysis Project (GLODAP). *Global Biogeochem. Cycles* **18**, (2004).
39. Alin, S. R. *et al.* Robust empirical relationships for estimating the carbonate system in the southern California Current System and application to CalCOFI hydrographic cruise data (2005–2011). *Journal of Geophysical Research: Oceans* **117**, (2012).
40. Kroeker 2023
41. Jacox, M. G., Moore, A. M., Edwards, C. A. & Fiechter, J. Spatially resolved upwelling in the California Current System and its connections to climate variability. *Geophysical Research Letters* **41**, 3189–3196 (2014).
42. Schroeder, I. D. *et al.* Source water variability as a driver of rockfish recruitment in the California Current Ecosystem: implications for climate change and fisheries management. *Can. J. Fish. Aquat. Sci.* **76**, 950–960 (2019).

43. R Core Team. R: A language and environment for statistical computing. R Foundation for Statistical Computing, Vienna, Austria. <https://www.R-project.org/>. (2022).
44. Zeileis A. & Hothorn T. Diagnostic checking in regression relationships. *R News*, **2**(3), 7–10 (2002).
45. Zeileis, A. & Grothendieck, G. zoo: S3 infrastructure for regular and irregular time series. *Journal of Statistical Software*, **14**(6), 1–27 (2005).
46. Bograd, S. J., Schroeder, I. D. & Jacox, M. G. A water mass history of the Southern California current system. *Geophysical Research Letters* **46**, 6690–6698 (2019).
47. Turi, G. *et al.* Response of O<sub>2</sub> and pH to ENSO in the California Current System in a high-resolution global climate model. *Ocean Science* **14**, 69–86 (2018).
48. Donham, E. M., Strobe, L. T., Hamilton, S. L. & Kroeker, K. J. Coupled changes in pH, temperature, and dissolved oxygen impact the physiology and ecology of herbivorous kelp forest grazers. *Global Change Biology* **28**, 3023–3039 (2022).
49. Durbin, J. & Watson, G.S. Testing for serial correlation in least squares regression. *Biometrika* **37**, 409–428 (1950).
50. Royston, P. The W test for normality. *Applied Statistics*, **31**, 176–180 (1982).
51. Bartlett, M. S. Properties of sufficiency and statistical tests. *Proceedings of the Royal Society of London Series A* **160**, 268–282 (1937).

## 2.9 Supplementary information

<b>Variable/Latitude</b>	<b>Bias</b>	<b>RMSD</b>	<b>Correlation</b>	$\sigma_{\text{model}}$	$\sigma_{\text{observations}}$
<b>Temperature (°C)</b>					
42N	0.6262	0.6669	0.9182	1.524	1.117
40N	0.1558	1.007	0.7314	1.430	1.296
38N	0.3620	0.8206	0.8473	1.367	0.7764
37N	0.6467	0.9049	0.9048	1.874	1.269
35N	0.3323	1.296	0.8090	1.937	0.9487
<b>DIC (mmol/m<sup>3</sup>)</b>					
42N	-21.15	42.50	0.8365	73.07	75.38
40N	5.111	35.83	0.8246	54.38	63.22
38N	17.78	27.53	0.8578	53.55	45.88
37N	-32.91	30.67	0.9010	68.48	54.08
35N	7.822	46.56	0.7203	67.03	45.97
<b>TAlk (meq/m<sup>3</sup>)</b>					
42N	2.162	21.21	0.7063	19.21	29.85
40N	-2.545	20.90	0.5249	16.98	24.02
38N	-2.309	14.62	0.6548	15.98	18.70
37N	-9.689	14.38	0.5851	17.13	13.74
35N	-2.697	14.18	0.4795	13.40	14.36
<b>pH (total scale)</b>					
42N	0.05674	0.07629	0.8572	0.1476	0.1330
40N	-0.02096	0.05509	0.8787	0.1061	0.1149
38N	-0.05755	0.09503	0.6533	0.1046	0.1209
37N	0.07143	0.06945	0.8566	0.1317	0.1271
35N	-0.02837	0.07569	0.8292	0.1342	0.1213

Table S2.1. Summary of model-comparison statistics for the Taylor diagrams presented in Fig. 2.1.

Property	Range of values	Sensitivity
Temperature	9.09 – 9.66 (°C)	0.007641
Salinity	33.7 – 33.86	-0.00471
Dissolved inorganic carbon (DIC)	2178 – 2198 (mmolC/m <sup>3</sup> )	-0.006954572
Total alkalinity	2246 – 2257 (meq/m <sup>3</sup> )	0.007359559

Table S2.2. Sensitivity analysis for aragonite saturation state. A sensitivity analysis following Turi et al., 2018, and using the CO2Sys\_v2.1.xls was conducted to assess the sensitivity of  $\Omega_{\text{arag}}$  to temperature, salinity, dissolved inorganic carbon (DIC) and total alkalinity.  $\Omega_{\text{arag}}$  values were calculated by varying one property at a time while keeping the others constant. The range of values represents the upwelling season mean +/- upwelling season standard deviation along the bottom of the 100m isobath. Sensitivity is calculated as the slope of a linear regression between the property being varied and the resulting  $\Omega_{\text{arag}}$  values.

	Intercept	DIC	Depth $\sigma_{26}$	$R^2$	AIC	DW p-value	SW p-value	BT p-value
1	***1.4844	0.4082		0.09704	80.33986	0.7284	0.02675	0.02671
2	***1.4844		***0.8630	0.4336	69.61213	0.08425	0.3221	0.006822
4	*** 1.4844	**0.6434	***1.0124	0.6616	59.76403	0.1127	0.1916	0.8153

Signif. codes: 0 ‘\*\*\*’ 0.001 ‘\*\*’ 0.01 ‘\*’ 0.05 ‘.’ 0.1 ‘ ’ 1

Table S2.3. Summary statistics of linear regressions. Linear regressions were fit between log(severity) and two explanatory variables, the depth of  $\sigma_{26}$  and the concentration of DIC at the depth of  $\sigma_{26}$ . Explanatory variables were fit independently and then together, and were scaled by their center values in order to compare coefficient. P-values from tests on the residuals are reported. The assumption of independence was verified using the Durbin-Watson (DW) test [1], the assumption of normality was verified using the Shapiro-Wilks (SW) test [1], and the assumption of constant variance was verified using the Bartlett test (BT) [3].

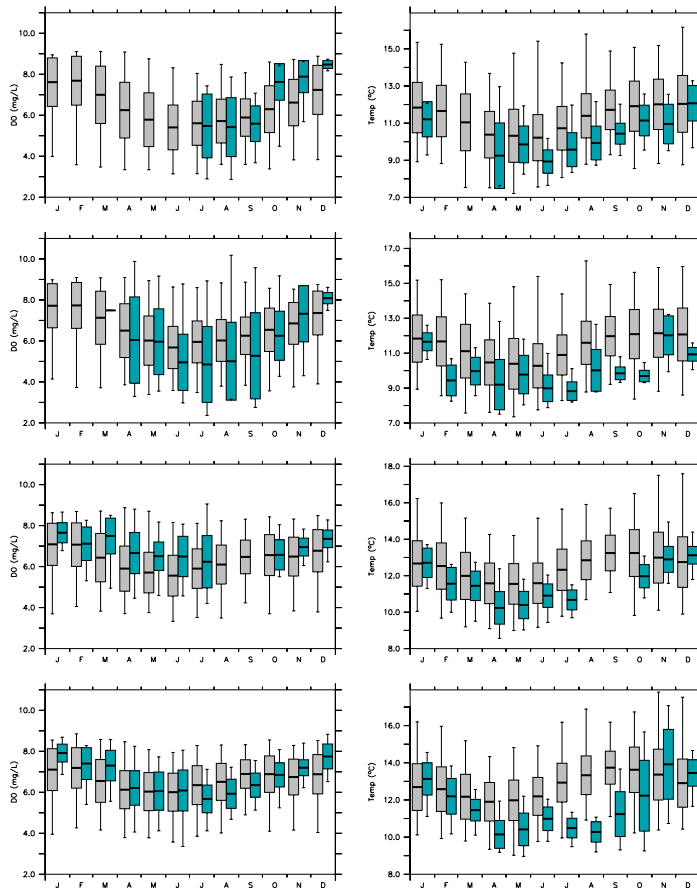


Figure S2.1. Simulated (1988-2010) and observed (2017-2019) dissolved oxygen (left) and temperature (right) at nearshore moorings. Monthly climatological mean, standard deviation and minimum/maximum values are represented by box and whisker plots for observed (blue) and simulated (gray) values at (from top to bottom) Van Damme, Point Arena, Big Creek, and Point Buchon (see Fig. 2.2 for locations).

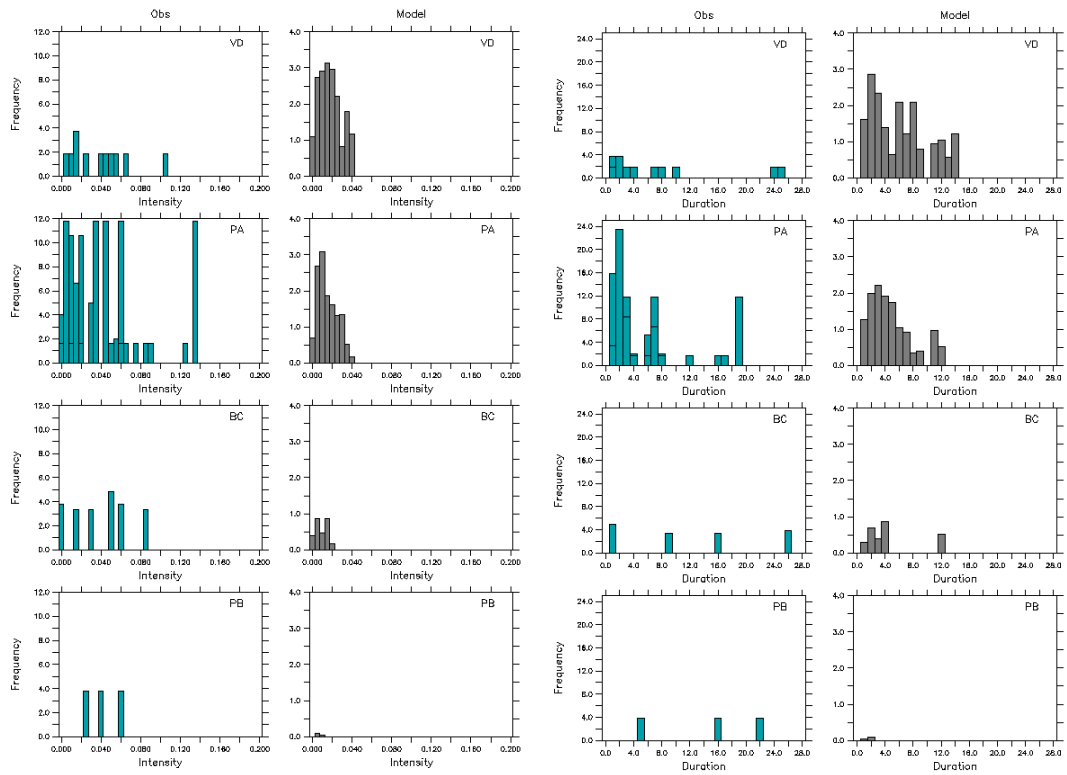
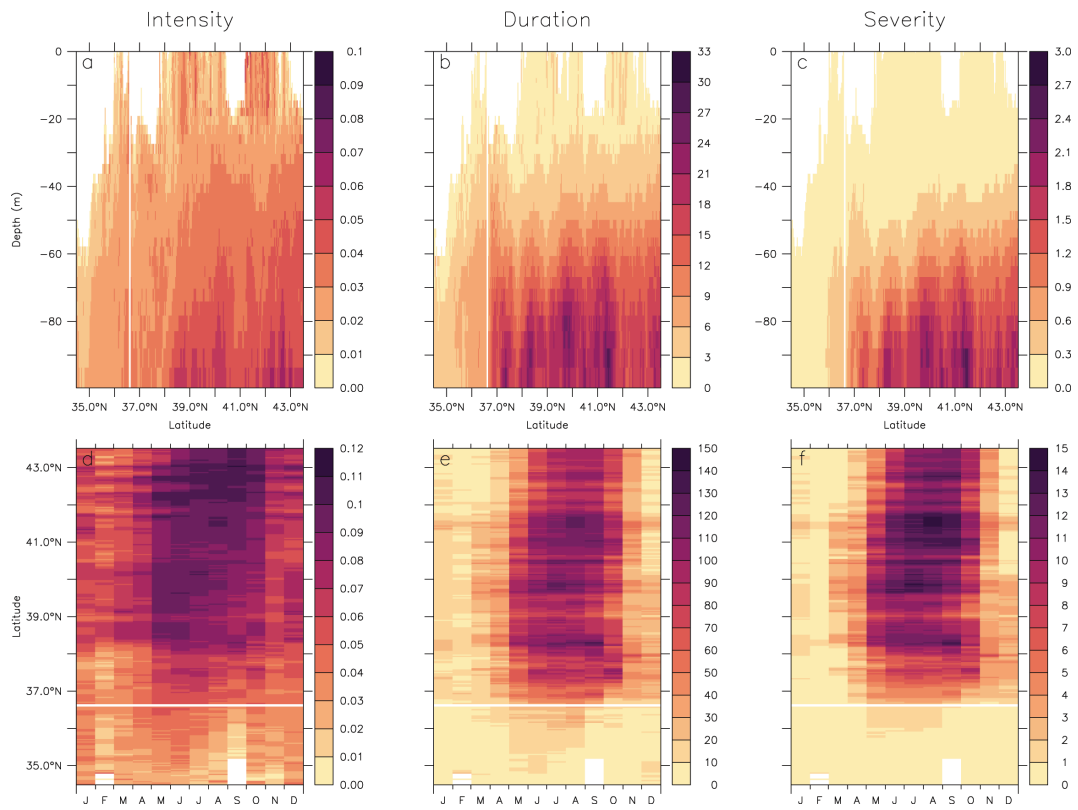


Figure S2.2. Simulated (1988-2010) and observed (2017-2019) intensity and duration of low pH events ( $\text{pH} < 7.7$ ). Frequency distribution of observed (blue) and simulated (gray) event duration (left panels) and intensity (right panels) at each nearshore mooring (VD=Van Damme, PA = Point Arena, BC = Big Creek, PB = Point Buchon; see Fig. 2.2 for locations). Event properties are normalized by the number of years of data.



**Figure S2.3.** Climatological properties of undersaturation events ( $\Omega_{\text{arag}} < 1$ ). Top: event properties along the 100m isobath with respect to depth and latitude in terms of their monthly climatological intensity (a), duration in days (b), and severity (c). Bottom: Monthly climatology of event properties along the bottom of the 100m isobath with respect to latitude in terms of intensity (d), duration in days (e), and severity (f). White shading indicates absence of events.



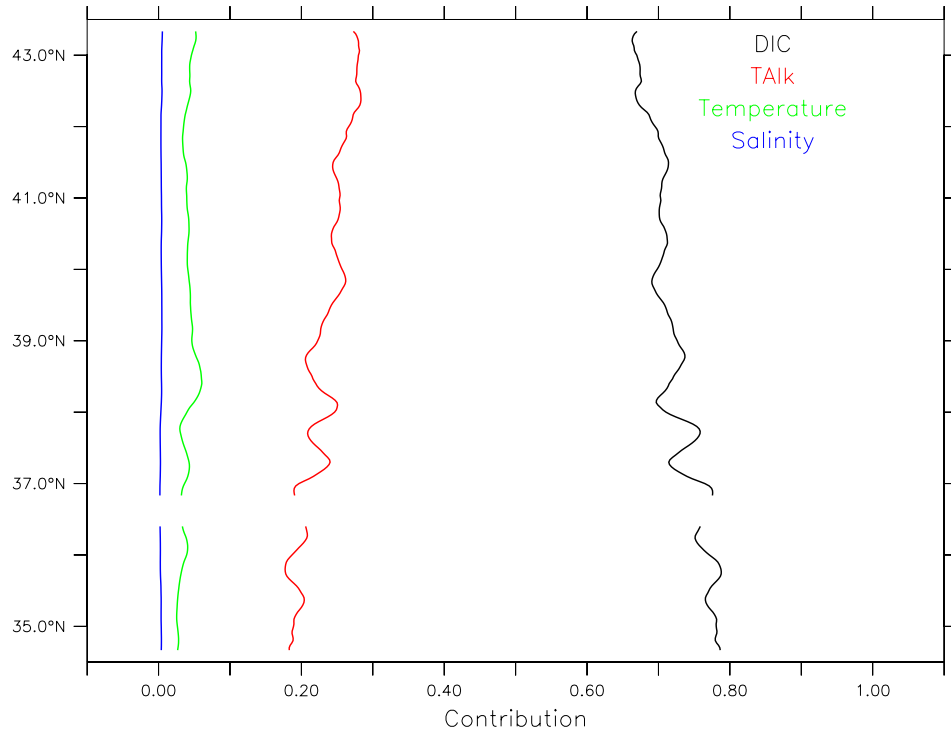


Figure S2.4. Fraction of the variability in  $\Omega_{\text{arag}}$  attributed to changes in DIC (red), total alkalinity (red), temperature (green) and salinity (blue) plotted as upwelling season averages as a function of latitude.

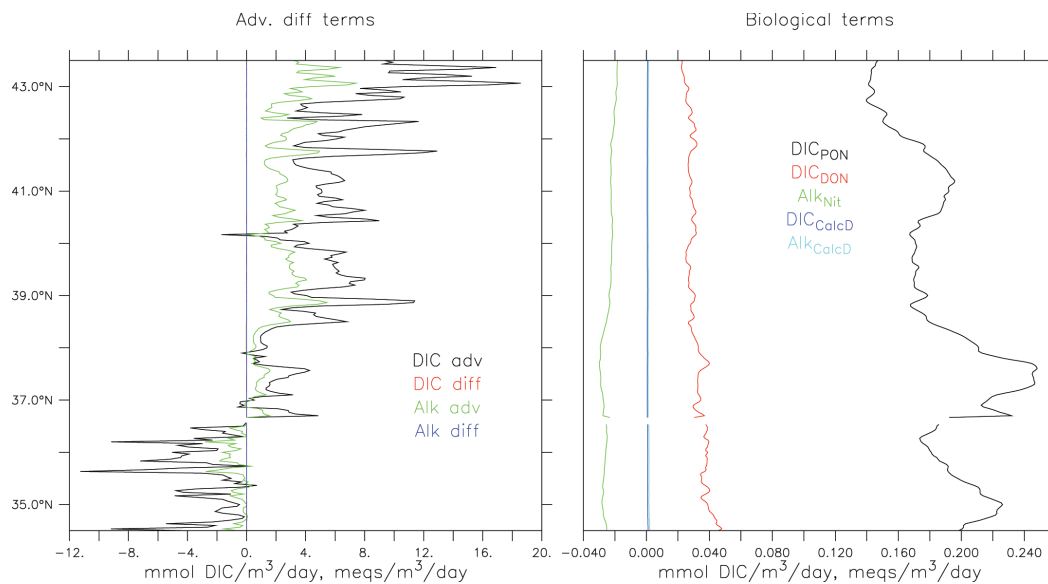


Figure S2.5. Dissolved inorganic (DIC) and total alkalinity (TALK) budget terms (mmol DIC/m<sup>3</sup>/day or meq/m<sup>3</sup>/day) along the bottom of the 100m isobath. (Left) Advection and mixing terms influencing DIC (black and red curves, respectively) and TALK (green and blue curves, respectively) (note that the two mixing terms overlay each other as they are several orders of magnitude lower than advective terms). (Right) Biological processes influencing DIC and TALK, including remineralization of particulate organic nitrogen (PON) into ammonium (black), remineralization of dissolved organic nitrogen (DON) into ammonium (red), calcium carbonate dissolution (CalcD) (blue for DIC, cyan for TALK), and nitrification (green). All values represent upwelling season means.

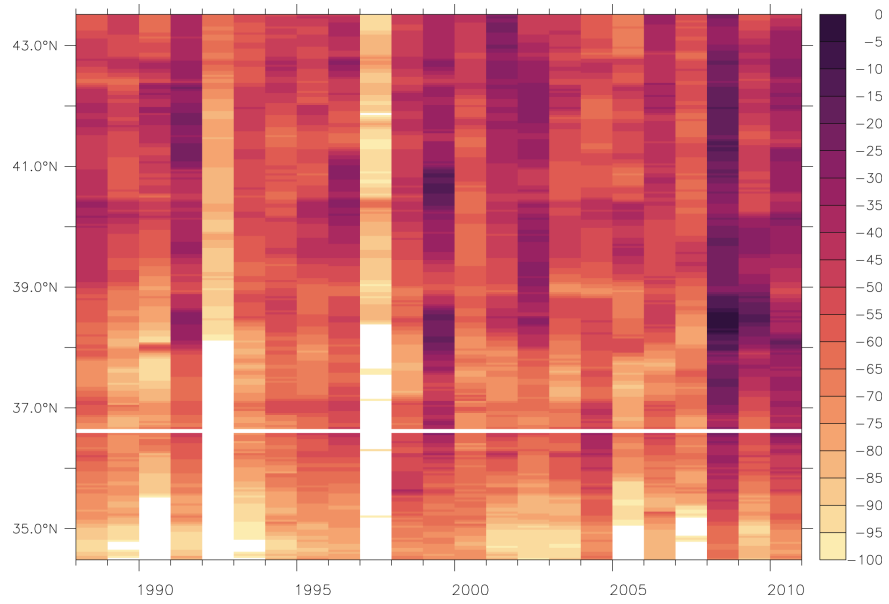


Figure S2.6. Mean depth (m) of 26.0 kg/m<sup>3</sup> isopycnal ( $\sigma_{26}$ ) on the 100m isobath during the upwelling season (May-Sept.). Missing data indicate that  $\sigma_{26}$  was deeper than 100m during the upwelling season.

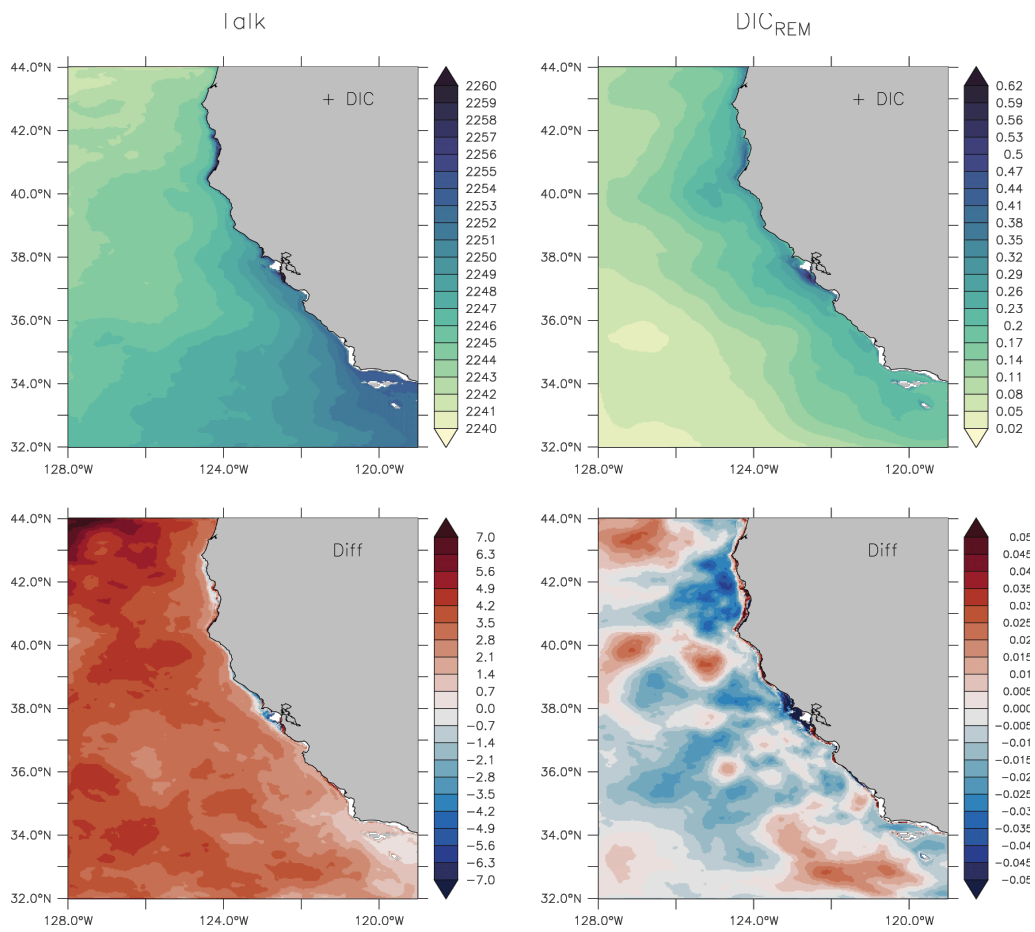


Figure S2.7. Top: Upwelling-season mean alkalinity (meq/m<sup>3</sup>) (left) and DIC<sub>REM</sub> (mmolC/m<sup>3</sup>/day) (right). Bottom: Upwelling-season mean alkalinity (meq/m<sup>3</sup>) (left) and DIC<sub>REM</sub> (mmolC/m<sup>3</sup>/day) (right) differences between positive and negative phases of the first EOF mode for DIC (see Fig. 2.6).

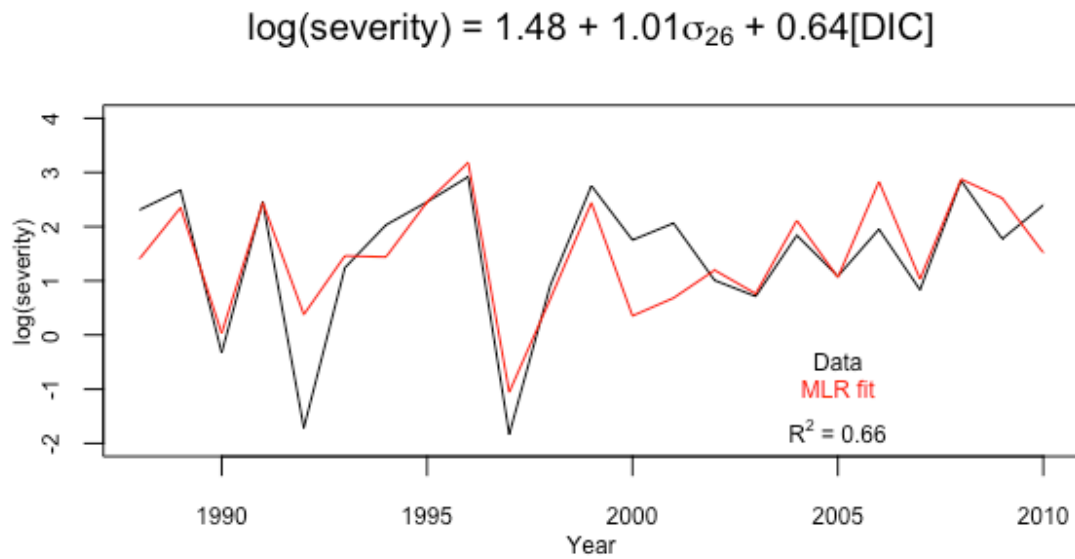


Figure S2.8. Multiple linear regression model (red) with latitudinally averaged (35.5-43.5°N ) annual upwelling season (May-Sept) values of log severity (black) as a response variable and the scaled depth of 26 isopycnal ( $\sigma_{26}$ ) and DIC concentrations at the depth of  $\sigma_{26}$  averaged 0-200km offshore as explanatory variables. The MLR is given by  $\log(\text{severity}) = 1.48 + 1.01(\sigma_{26}) + 0.64([\text{DIC}])$  and yields a multiple R-squared value of 0.66.

## 2.10 Supplementary References

1. Durbin, J. & Watson, G.S. Testing for serial correlation in least squares regression. *Biometrika* **37**, 409–428 (1950).
2. Royston, P. The W test for normality. *Applied Statistics*, **31**, 176–180 (1982).
3. Bartlett, M. S. Properties of sufficiency and statistical tests. *Proceedings of the Royal Society of London Series A* **160**, 268–282 (1937).

## Chapter 3 - Future evolution of OAH hot spots and refugia in the central California

### Current System

Julia Cheresh and Jerome Fiechter

#### 3.1 Abstract

In the California Current System, low pH and oxygen exposure occurs naturally due to coastal upwelling, which draws acidified, oxygen-depleted water onto the shelf. The addition of anthropogenic ocean acidification and deoxygenation are pushing conditions beyond critical biological thresholds, and there is an urgent need to understand how the future progression of these stressors will unfold at regional and local scales. Here, a three-member ensemble of regional climate projections downscaled to 3 km horizontal resolution is used to characterize the future progression of ocean acidification and hypoxia (OAH) in the central California Current System through the end of the 21st century. The results indicate that OAH hot spots and refugia, and their emergence from present-day conditions, depend heavily on the metrics used to quantify them. Locations where pH emerges earliest from its historical range of variability correspond to regions of inherently low variability, whereas locations where pH crosses a specified biological threshold earliest correspond to regions with low baseline pH values. Neither the alongshore patterns of the time when pH emerges from its historical range of variability nor the time when pH drops below a specified threshold correlate with the alongshore pattern of the pH trend. In contrast, the alongshore pattern of the year when oxygen emerges

from its historical envelope of variability is correlated with the alongshore pattern in the trend in oxygen. These findings provide important insight into the properties shaping the future progression of OAH, and highlight the complexity of characterizing anthropogenic change in a highly spatially and temporally dynamic system.

### 3.2 Introduction

Ocean acidification and global oxygen decline are among the most concerning anthropogenic threats to marine life. In the California Current System (CCS), where environmental variability is dominated by upwelling, the impacts of ocean acidification and hypoxia (OAH) are particularly pronounced, due to natural exposure to lower pH and oxygen conditions during seasonal coastal upwelling (Hauri et al., 2009). Enhanced nutrient content in upwelled water supports primary production, which increases pH and oxygen near the surface, but reduces pH and oxygen at depth due to export production and remineralization. Nearshore denizens of the CCS are adapted to withstand relatively high environmental variability however, the recent and projected evolution of OAH will push conditions beyond these ranges, causing a variety of deleterious responses (Kroeker et al., 2013; Bednarsek et al., 2019; Bednarsek et al., 2020). Observations have already captured the emergence of corrosive water in the surface layer and shoaling of the hypoxic boundary, and these events are predicted to increase in severity and frequency, resulting in a compression of viable habitat for ecologically, economically and culturally important species

(Feely et al. 2007; Bograd et al., 2008; Hauri et al., 2013a,b; Gruber et al., 2012; Howard et al., 2020).

The central CCS (~35-43°N) is home to highly productive and biodiverse ecosystems, which hold significant ecological, economic, and cultural importance. The region also harbors many commercially harvested and protected species, and supports a network of marine protected areas including three National Marine Sanctuaries. While seasonal upwelling is a dominant control on environmental variability along most of the U.S. West Coast, upwelling intensity and ecosystem responses are not spatially or temporally homogeneous. Atmospheric fields and ocean circulation are affected by coastline morphology (Pickett and Paduan 2003), and biogeochemical variability has been similarly linked to topographic features locally modulating upwelling intensity and the advective properties of the alongshore and cross-shore circulation (Kudela et al., 2008; Fiechter et al. 2018; Cheresh and Fiechter 2020). These findings are supported by in situ measurements from CCS-wide synoptic shipboard surveys and time series from nearshore stations, which both document a spatial pattern of low pH exposure at local "hotspots" near topographic features (Feely et al. 2008; Chan et al. 2018). Since pH and oxygen typically covary (Baumann and Smith 2017), low-oxygen exposure exhibits a similar nearshore spatial pattern (Cheresh and Fiechter, 2020).

Unfortunately, the central CCS is lacking a sustained long-term ocean monitoring network, and adequate spatiotemporal monitoring in the region is made challenging by complex interactions between physical and biogeochemical



oceanographic processes occurring at relatively small spatial scales. Therefore, high-resolution model simulations of environmental change can aid monitoring investment decisions and provide assessment of future impacts of OAH on habitats of managed species. Existing modeling studies predict rapid intensification of ocean acidification in the CCS in the coming decades. For instance, Gruber et al. (2012) estimated that by 2050, half of the water column will be undersaturated with respect to aragonite. Concurrently, the intensity of low-aragonite events is projected to increase threefold over the same period (Hauri et al., 2013). For sensitive species, suitable habitat is predicted to dramatically shrink and shift due to oxygen declines (Howard et al., 2020), and the same can be expected for acidification-driven declines. However, Cheresh and Fiechter (2020) demonstrated that historical changes in pH and oxygen during 1988-2010 are not spatially homogenous and consist of an alongshore succession of minima and maxima in trends at scales of O(10-100 km), with the most dramatic long-term reduction in pH and oxygen (and thus the most vulnerable habitats to OAH) occurring near local upwelling centers.

Therefore, characterizing the progression of future OAH based on regional averages may underestimate the occurrence and severity of OAH hotspots, but also obscure potential areas of refuge for vulnerable species. Furthermore, pH and oxygen vary significantly with depth, which suggests that future changes may differentially affect benthic vs. pelagic organisms. However, our understanding of the dynamics driving local scale variability in pH and oxygen levels from in situ observations is often limited to the surface. To address these issues and improve our understanding of

OAH impacts on shifting or disappearing viable habitats throughout the water column, an ensemble of high-resolution downscaled climate projections for the central CCS is examined. Three earth system models (ESMs) were selected from the CMIP5 ensemble and downscaled to 3 km resolution to represent the projected range of physical and biogeochemical changes in the CCS under the RCP8.5 high emissions scenario.

Because exposure to low pH and oxygen conditions in the CCS exhibits high alongshore variability, this study focuses on future “hot spots” and “refugia”, and the time at which these features become distinct from present-day variability. Time of Emergence (ToE) is a commonly used term in climate science to describe the point at which an anthropogenic signal emerges from natural variability, and it has been widely used in signal detection of physical variables such as temperature. The concept has more recently been utilized in biogeochemical applications as well, and often is calculated as the first year when the signal-to-noise ratio is greater than or equal to 2 (Schlunegger et al., 2019, Turk et al., 2019). While useful in describing the progression of environmental anthropogenic change, this definition of emergence is not particularly ecologically relevant, nor necessarily suitable for dynamic coastal environments which exhibit high interannual variability. Therefore, the present study examines other potentially more biologically meaningful metrics to quantify time of emergence as it relates to crossing particular biological thresholds or conditions significantly different from historical mean conditions and variability.

### 3.3 Methods

#### 3.3.1 Coupled physical-biogeochemical model

A coupled physical-biogeochemical model is used to produce the regional ocean acidification and hypoxia projections. The physical model is an implementation of the Regional Ocean Modeling System (ROMS) (Haidvogel et al., 2008; Shchepetkin & McWilliams, 2005) for the California Current region including a higher resolution (1/30 deg.) domain for the central CCS (32-44N, 116.5-128.5W) nested into a lower resolution (1/10 deg.) domain for the entire CCS (30–48°N; 115.5–134°W). The vertical resolution for both domains is given by 42 terrain-following depth levels with surface and bottom clustering. NEMUCSC is a biogeochemical model adapted from the North Pacific Ecosystem Model for Understanding Regional Oceanography (NEMURO; Kishi et al., 2007), with the addition of carbon and oxygen cycling (Cheresh & Fiechter, 2020). NEMURO contains three limiting micronutrients (nitrate, silicate and opal), representative phytoplankton (nanophytoplankton and diatoms) and zooplankton (micro, meso and predatory) groups, and detritus pools (DON, PON and opal). NEMUCSC includes oxygen and carbon submodels, which track dissolved oxygen, DIC, total alkalinity, and calcium carbonate concentrations. The calculations of pCO<sub>2</sub>, pH, and aragonite saturation state are based on the OCMIP chemistry described in `co2calc_SWS.f` (<http://ocmip5.ipsl.jussieu.fr>). ROMS and NEMUCSC are coupled such that daily atmospheric fluxes and physical fields are read in from an existing ROMS simulation

and used to calculate sources, sinks, and transport of biogeochemical properties in NEMUCSC in an “offline” manner (Cheresh and Fiechter, 2020).

### 3.2.2 Earth System Models

The three earth system models (ESMs) used to generate the downscaled ROMS-NEMUCSC projections are the Geophysical Fluid Dynamics Laboratory (GFDL) ESM2M (Dunne et al., 2012), Institut Pierre Simon Laplace (IPSL) CM5A-MR (Dufresne et al., 2013), and Hadley Center HadGEM2-ES (Collins et al., 2011), referred to hereafter as GFDL, IPSL, Hadley, respectively. These ESMs were selected from the Coupled Model Intercomparison Project phase 5 (CMIP5) ensemble because they capture the spread of CMIP5 ensemble projected 21<sup>st</sup> century warming and primary productivity (in terms of both mean and variance) under the RCP8.5 high emissions scenario.

The GFDL, IPSL and Hadley solutions for 1980-2100 were first dynamically downscaled to 1/10° (~10 km) resolution using a time-varying delta approach for the region between 30–48°N and 115.5–134°W (Pozo Buil et al., 2021) and subsequently nested into the higher resolution 1/30° (~3km) domain for the central CCS.

### 3.2.3 Analysis method

To assess spatial and temporal patterns in the downscaled projections, annual mean temperature, pH, aragonite saturation state ( $\Omega_{arag}$ ), and dissolved oxygen values are extracted at all latitudes from the coast to the 100m isobath, which roughly approximates the shelfbreak in the central CCS. For pH and oxygen, general metrics

such as mean, standard deviations, and trends are calculated, as well as two specific metrics: “climatological time of emergence” ( $ToE_{clim}$ ) and “threshold time of emergence” ( $ToE_{thresh}$ ).  $ToE_{clim}$  represents the year when conditions (i.e. pH or dissolved oxygen) permanently leave the historical envelope of variability, defined here as the 2000-2020 mean  $\pm$  1 standard deviation.  $ToE_{thresh}$  represents the year when conditions permanently drop below a specified threshold (e.g., pH < 7.75). Annual mean surface and bottom values, averaged between the coast and the 100m isobath are used to calculate  $ToE_{clim}$  and  $ToE_{thresh}$ . To facilitate identification of the properties shaping the alongshore patterns of  $ToE_{clim}$  and  $ToE_{thresh}$ , 2000-2020 temporal mean and standard deviation, and 2000-2100 trend, these quantities are regridded to a  $0.25^\circ$  latitudinal axis, which helps remove alongshore noise associated with local processes acting at spatial scales smaller than a Rossby radius of deformation ( $\sim 30$  km for the region). The 2000-2020 temporal mean, 2000-2020 temporal standard deviation, and 2000-2100 trends for pH and dissolved oxygen are regressed against  $ToE_{clim}$  and  $ToE_{thresh}$  for pH and  $ToE_{clim}$  for dissolved oxygen. A threshold of pH < 7.75 is used to calculate  $ToE_{thresh}$ , as this value approximates the threshold below which dissolution is thermodynamically favorable over calcification in the nearshore central CCS.  $ToE_{thresh}$  was not calculated for dissolved oxygen, because it never permanently crosses established hypoxic thresholds, and values at the surface are bottom are sufficiently ecologically distinct, such that different thresholds would need to be applied.

### 3.4 Results

At both the surface and bottom of the 100m isobath, the three models show general agreement in warming, with alongshore average temperatures increasing through the end of the century (Fig. 3.1a,e). The models begin to diverge around 2050, with, as expected, Hadley predicting the highest rate of warming, and GFDL predicting the lowest rate of warming. The year when the annual ensemble mean permanently exits the historical envelope of variability at a given latitude (referred to as  $ToE_{clim}$  hereafter) ranges from 2020-2040 and 2030-2040 for surface and bottom temperature along the surface and bottom of the 100m isobath, respectively (hashed period in Fig. 3.1a,e).

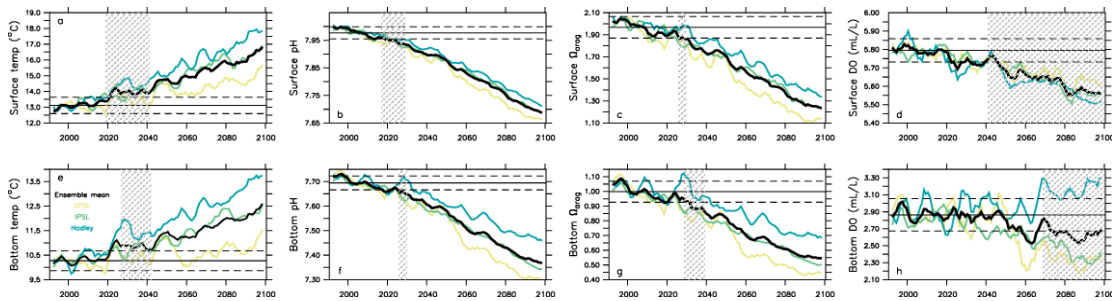


Figure 3.1 Projected changes in temperature, pH, aragonite saturation state, and dissolved oxygen along the surface and bottom of the 100m isobath. Projected temperature (a,e), pH (b,f), aragonite saturation state (c,g), and dissolved oxygen (d,h) from GFDL (yellow), IPSL (green) and Hadley (blue) and the three-member ensemble mean (black). Horizontal black solid and dashed lines represent the 1990-2020 mean and mean  $\pm 1$  standard deviation, respectively. Hashing depicts the range of years when the ensemble mean permanently departs from the historical envelop (1990-2020 mean  $\pm 1$  standard deviation) at each latitude along the 100m isobath.

At the surface, alongshore mean values along the 100m isobath depict a relatively linear decrease in pH,  $\Omega_{arag}$ , and dissolved oxygen through the century in all three model projections (Fig. 3.1b-d). At the bottom, projected pH,  $\Omega_{arat}$ , and

dissolved oxygen decline through the end of the century, except for the Hadley solution, which exhibits a sudden increase in dissolved oxygen for 2070-2100 (Fig. 3.1f-h).

$ToE_{clim}$  values range from approximately 2018-2028 and 2026-2030 for surface and bottom pH along the 100m isobath, respectively (hashed period in Fig. 3.1b,f).  $\Omega_{arag}$   $ToE_{clim}$  values range from approximately 2028-2030 and 2030-2040 along the surface and bottom of the 100m isobath, respectively (hashed period in Fig. 3.1c,g). While there is strong model agreement for surface pH through the end of the century, the projected changes at the bottom from the three ensemble members begin to diverge mid-century. Hadley predicts the most modest decreases in pH and  $\Omega_{arag}$ , while GFDL predicts the greatest decreases in pH and  $\Omega_{arag}$ . Oxygen exhibits stronger interannual variability relative to pH and  $\Omega_{arag}$ , resulting in later, and much more latitudinally variable  $ToE_{clim}$  values along the surface and bottom of 100-m isobath (2040-2100 and 2070-2100, respectively) (hashed period in Fig. 3.1d,h). At the bottom of the 100m isobath, Hadley predicts increasing dissolved oxygen values, which stands in strong contrast to IPSL and GFDL, and does not align with current understanding of the physical and biogeochemical effects expected to accompany anthropogenic climate change. For this reason, the remainder of the analysis focuses on IPSL, with future work planned to compare IPSL with GFDL as a more moderate warming scenario (but not necessarily lesser impacts on pH, omega, and dissolved oxygen).

We next consider the alongshore patterns of  $ToE_{clim}$  and  $ToE_{thresh}$  by looking at their values at each latitude.  $ToE_{clim}$  for pH exhibits a relatively narrow range of alongshore variability, with values spanning 2021-2034 at the surface, and 2025-2035 at the bottom (Fig. 3.2d, i). Locations in the lower quartile of  $ToE_{clim}$  values for pH indicate an earlier time of emergence and include  $\sim 41.5^\circ\text{N}$ ,  $37.5^\circ\text{N}$ ,  $36.8^\circ\text{N}$  and  $35^\circ\text{N}$ . Locations in the upper quartile of  $ToE_{clim}$  values for pH indicate a later time of emergence and include  $\sim 43^\circ\text{N}$ ,  $38.8^\circ\text{N}$  and  $36^\circ\text{N}$ . The alongshore pattern of  $ToE_{clim}$  for pH most closely resembles the alongshore pattern of the 2000-2020 temporal standard deviation (also referred to as “historical variability”, hereafter), such that latitudes with earlier  $ToE_{clim}$  correspond to latitudes with lower 2000-2020 standard deviations, and vice versa (Fig. 3.2 a, d, b, g). Regressions between  $ToE_{clim}$  for pH and historical variability at the surface and bottom yield  $R^2$  values of 0.42 and 0.37, respectively (Table 3.1).



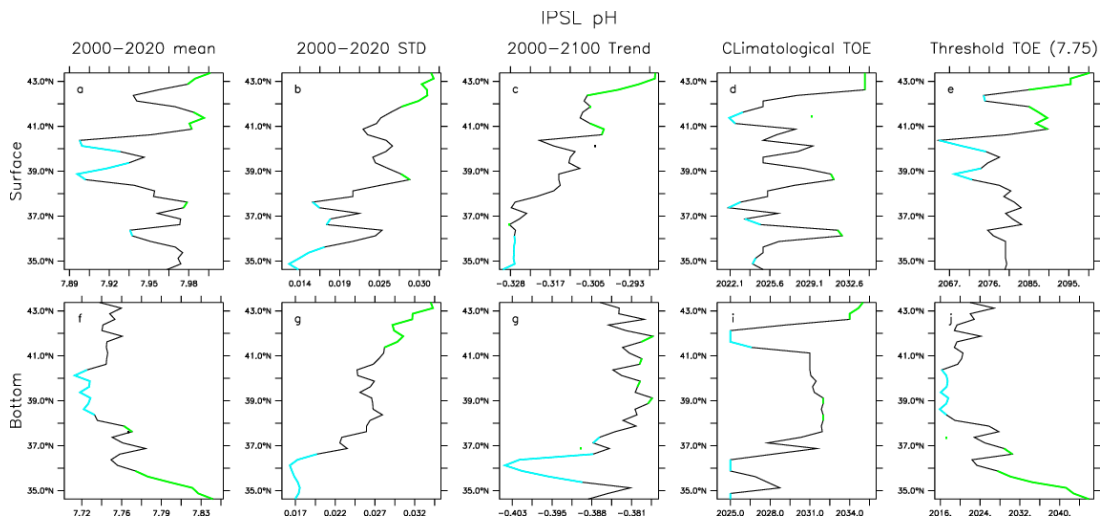


Figure 3.2 Alongshore properties influencing climatological and threshold time of emergence ( $ToE_{clim}$  and  $ToE_{thresh}$ ) for pH. Surface (a-e) and bottom (f-j) 2000-2020 mean pH (a,f), 2000-2020 pH standard deviation (b,g), 2000-2100 pH trend (unit =  $100 \text{ years}^{-1}$ ) (c,h),  $ToE_{clim}$  (unit = year) (d,i) and  $ToE_{thresh}$  (unit = year) (e,j) as a function of latitude.  $ToE_{thresh}$  is calculated using a threshold of pH = 7.75. All properties are calculated using a cross-shelf average from the coast to the 100m isobath. Green overlay represents latitudes that fall within the upper quartile (across all latitudes) and cyan overlay represents latitudes that fall into the lower quartile.

For pH,  $ToE_{thresh}$  exhibits a much wider range than  $ToE_{clim}$ , with values spanning 2064-2099 and 2015-2045 at the surface and bottom, respectively (Fig. 3.2 e, j). At the surface, locations in the lower quartile indicate an earlier  $ToE_{thresh}$  and include  $\sim 42.5^\circ\text{N}$ ,  $40.5^\circ\text{N}$ , and  $38.8^\circ\text{N}$ . Locations in the upper quartile at the surface indicate a later  $ToE_{thresh}$  and include  $43^\circ\text{N}$ ,  $41-42^\circ\text{N}$ , and  $37.5^\circ\text{N}$ .

Alongshore variability in  $ToE_{thresh}$  is tightly linked to the 2000-2020 mean pH values (Fig. 3.2 e, j, a, f), with linear regressions between the two resulting in an  $R^2$  values of 0.77 and 0.96 at the surface and bottom, respectively (Table 3.1). This result indicates that regions with historically low pH will be the first to cross below specific thresholds, while regions with higher historical pH will cross the threshold up to 30 years later. At the bottom, an  $R^2$  of 0.35 indicates a relationship between the

alongshore patterns of  $ToE_{thresh}$  and the 2000-2020 standard deviation for pH, such that locations with higher variability have an earlier  $ToE_{thresh}$ .

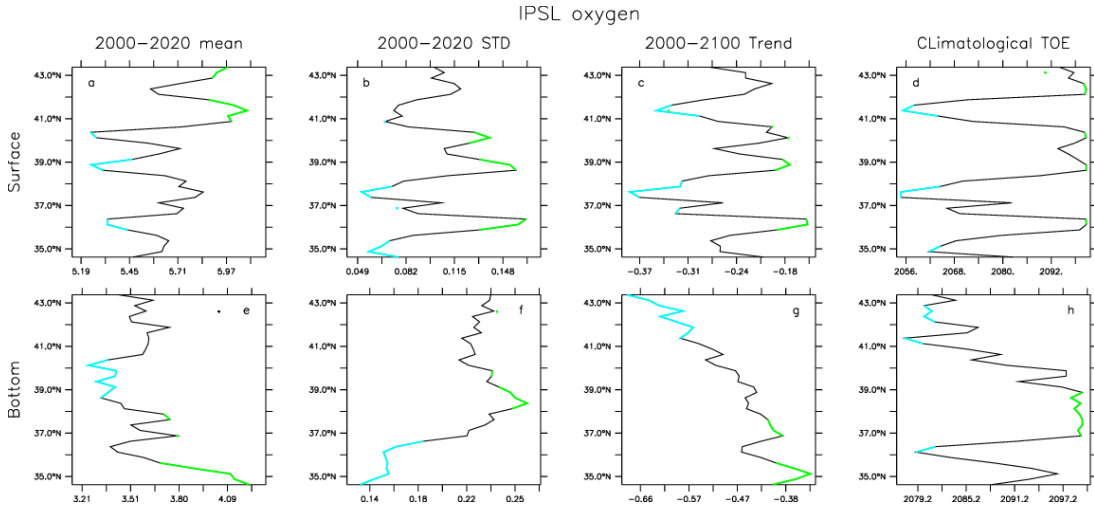


Figure 3.3 Alongshore properties influencing climatological time of emergence ( $ToE_{clim}$ ) for dissolved oxygen. Surface ( a-d) and bottom ( e-h) 2000-2020 mean DO (a,e), 2000-2020 DO standard deviation (b,f), 2000-2100 DO trend (unit =  $100 \text{ years}^{-1}$ ) (c,g) and  $ToE_{clim}$  (unit = year) (d,h) as a function of latitude. All properties are calculated using a cross-shelf average from the coast to the 100m isobath. Green overlay represents latitudes that fall within the upper quartile (across all latitudes), while cyan overlay represents latitudes that fall into the lower quartile.

Oxygen exhibits a wide range of  $ToE_{clim}$  values at both the surface and bottom, spanning approximately 2055-2100 and 2077-2099, respectively (Fig. 3.3d, h). The alongshore pattern of surface oxygen  $ToE_{clim}$  corresponds with the alongshore patterns of both the 2000-2020 standard deviation (Fig. 3.3b, f) and 2000-2100 trend (Fig. 3.3c, g). Regressions between surface oxygen  $ToE_{clim}$  and surface oxygen 2000-2020 standard deviation and 2000-2100 trend yield  $R^2$  values of 0.74 and 0.76, respectively (Table 3.1). At the surface, locations in the lower quartile indicate earlier  $ToE_{clim}$  and include  $\sim 41.5^\circ\text{N}$ ,  $37.5^\circ\text{N}$ , and  $35^\circ\text{N}$ , which correspond

to regions of low historical variability and a more strongly negative trend. Surface locations in the upper quartile indicate later  $ToE_{clim}$  and include  $\sim 42.5^\circ\text{N}$ ,  $40.4^\circ\text{N}$ ,  $38.5^\circ\text{N}$  and  $37.5^\circ\text{N}$ . At the bottom, locations in the lower quartile indicate earlier  $ToE_{clim}$  and include  $\sim 42-43^\circ\text{N}$ ,  $41.5^\circ\text{N}$ , and  $36^\circ\text{N}$ . Locations in the upper quartile for bottom oxygen indicate later  $ToE_{clim}$  and include the region between  $37-39^\circ\text{N}$ .  $ToE_{clim}$  for bottom oxygen relates most closely to the 2000-2100 trend, with a regression between the alongshore patterns of  $ToE_{clim}$  and the 2000-2100 trend yielding an  $R^2$  value of 0.49 (Table 3.1). This result indicates that near the bottom, the trend is the primary determinant of when oxygen will exit its historical envelope of variability.

Surface pH				Bottom pH			
	2000-2020 mean	2000-2020 STD	2000-2100 Trend		2000-2020 mean	2000-2020 STD	2000-2100 Trend
TOE clim	0.0671	0.4272	0.2662	TOE clim	0.2037	0.3741	0.2582
TOE thresh	0.7764	0.0118	0.2658	TOE thresh	0.9577	0.3571	0.1077

Surface DO				Bottom DO			
	2000-2020 mean	2000-2020 STD	2000-2100 Trend		2000-2020 mean	2000-2020 STD	2000-2100 Trend
TOE clim	0.3597	0.7352	0.7573	TOE clim	0.0034	0.07167	0.4906

Table 3.1  $R^2$  values from regressions between climatological time of emergence ( $ToE_{clim}$ ) and 2000-2020 mean values, 2000-2020 standard deviation values, 2000-2100 trend values for surface and bottom pH and oxygen, and between threshold time of emergence ( $ToE_{thresh}$ ) and 2000-2020 mean values, 2000-2020 standard deviation values, 2000-2100 trend values for surface and bottom pH. Regressions were calculated using cross-shelf averages from the coast to the 100m isobath. Blue shading indicates properties most highly correlated with  $ToE_{clim}$ . Green shading indicates properties most highly correlated with  $ToE_{thresh}$ .

### 3.5 Discussion

Results from three downscaled regional climate projections (i.e., Hadley, IPSL and GFDL) provide an assessment of the future progression of OAH, and

illustrate the challenges of characterizing hot spots and refugia in a highly dynamic coastal upwelling system. Hadley is excluded from the time of emergence analyses due to its increasing oxygen trend at depth, which conflicts with the other projections, and the consensus surrounding deoxygenation occurring at depth along with anthropogenic climate change. This increase in oxygen in depth corresponds to a sudden, rapid decrease in primary production projected by Hadley around 2050 (Pozo Buil et al., 2021), presumably leading to a reduction in respiration of organic matter at depth. This precipitous decrease in primary production is unlikely and suggests that Hadley's representation of biogeochemical processes may not be suitable for the California Current upwelling system beyond mid-century. IPSL is the focus of the analysis as its rate of warming roughly tracks the CMIP5 ensemble mean, providing a middle-of-the-road estimate under the RCP8.5 high emissions scenario.

In upwelling systems such as the CCS, pH and oxygen dynamics tend to covary, because they are influenced by the same physical and biogeochemical processes. However, the projections demonstrate that the progression of ocean acidification and deoxygenation will likely be decoupled in nature. The projections show a relatively linear decrease in pH through the end of the century, with high alongshore coherence in the time at which annual pH permanently drops below the historical envelope of variability ( $ToE_{clim}$ ). In contrast, oxygen exhibits stronger interannual variability throughout the century relative to its long-term negative trend, resulting in both later and less spatially coherent  $ToE_{clim}$  values. This finding is

likely due to a strong trend in atmospheric  $CO_2$  in the RCP8.5 emissions scenario, whereas no trend is present in atmospheric oxygen.

To characterize ocean acidification hot spots and refugia, many practitioners look to anthropogenic trends. However, the downscaled projections presented here suggest that trends in pH are not particularly variable across latitudes in the central CCS, and are not highly correlated with the time at which pH permanently exits its historical range of variability or crosses a biologically-relevant threshold. Furthermore, looking at the alongshore patterns in pH trends,  $ToE_{clim}$  and  $ToE_{thresh}$  both provide a different narrative, whereby regions with the strongest negative trends do not necessarily coincide with the earliest  $ToE_{clim}$  or  $ToE_{thresh}$ , and  $ToE_{clim}$  and  $ToE_{thresh}$  do not necessarily mirror each other.

The alongshore pattern of  $ToE_{clim}$  for pH is most correlated with historical variability, such that locations that emerge soonest in the simulation period also exhibit the lowest historical variability. These locations, including 35°N, 36.75°N, 37.5°N and 41.5°N, correspond to regions of enhanced primary production associated with higher pH and oxygen values at the surface (Cheresh and Fiechter, 2020). Locations that emerge later in the simulation, such as 36.5°N, 38.5°N and 43°N, exhibit high historical variability, and correspond to regions of enhanced upwelling. When considering time of emergence using a particular threshold for pH, such as 7.75, some locations exhibiting the earliest  $ToE_{clim}$  values have the latest  $ToE_{thresh}$  values, such as 40°N and 41.5°N.  $ToE_{thresh}$  is most highly correlated with historical mean values, whereby locations with historically low values permanently drop below

a specified threshold soonest. These locations include 39°N, 40°N and 42.5°N, which are all located in regions of relatively strong upwelling (as compared to other latitudes within the domain) (Cheresh and Fiechter, 2020). Therefore, enhanced upwelling regions that historically exhibit high variability and low pH exposure are associated with later  $ToE_{clim}$  values and earlier  $ToE_{thresh}$  values. While  $ToE_{clim}$  and  $ToE_{thresh}$  do not directly contradict each other at all locations, it is important to highlight the fact that defining a hot spot vs. refugia, and when these features emerge, depends strongly on the metrics of interest or needed for management.

The story of oxygen is different. Significantly more alongshore variability is present in the 2000-2100 oxygen trend than in that of pH, and the trend is highly correlated with  $ToE_{clim}$ . At the surface, locations with earlier  $ToE_{clim}$  values for oxygen correspond to stronger negative trends and lower historical variability, and are situated in regions of historically high primary production (Cheresh and Fiechter, 2020). Locations with later  $ToE_{clim}$  values for oxygen correspond to weaker trends, and are situated in regions of historically strong upwelling intensity. This finding indicates that oxygen is decreasing more rapidly in regions where primary production is the dominant oxygen driver (as opposed to upwelling), thereby suggesting that biological activity is changing more rapidly in the simulation than physical processes, such as upwelling strength or water mass circulation. Unlike pH, whose alongshore properties are similar at the surface and bottom, the trend and  $ToE_{clim}$  alongshore patterns for oxygen differ across depth. At the bottom, locations with earlier  $ToE_{clim}$  values correspond to regions of historically enhanced upwelling, while locations with

later  $ToE_{clim}$  values correspond to regions of historically elevated primary production (Cheresh and Fiechter, 2020).

The results presented here highlight the complexity of characterizing anthropogenic change in a highly variable marine ecosystem. Not only do pH and oxygen exhibit different patterns in terms of their decline throughout the century, but characterizing hot spots and refugia for each is dependent upon the metric of interest. These findings suggest that practitioners interested in where and when pH will emerge from its historical range of variability soonest may want to identify locations with historically low temporal variability, which in the central CCS is likely away from enhanced upwelling centers and within regions of elevated primary productivity. Those interested in where and when pH will permanently cross a particular threshold may want consider locations with historically low baseline values, likely near enhanced upwelling centers. If one is interested in surface oxygen and when it will emerge from its historical envelope of variability, regions of enhanced primary production will emerge soonest, whereas near the bottom regions of enhanced upwelling will emerge soonest. Future work to further characterize the physical and biogeochemical processes shaping the alongshore response of  $ToE_{clim}$  and  $ToE_{thresh}$  should continue to improve the preliminary assessment of the projected evolution of OAH hotspots and refugia presented here. Additionally, repetition of the analysis with GFDL would allow for comparison with IPSL and exploration of these metrics under a more moderate warming scenario.

### 3.6 References

- Bednaršek, N., Feely, R. A., Beck, M. W., Alin, S. R., Siedlecki, S. A., Calosi, P., Norton, E. L., Saenger, C., Štrus, J., Greeley, D., Nezhlin, N. P., Roethler, M., & Spicer, J. I. (2020). Exoskeleton dissolution with mechanoreceptor damage in larval Dungeness crab related to severity of present-day ocean acidification vertical gradients. *Science of The Total Environment*, 716, 136610. <https://doi.org/10.1016/j.scitotenv.2020.136610>
- Bednaršek, N., Feely, R. A., Howes, E. L., Hunt, B. P. V., Kessouri, F., León, P., Lischka, S., Maas, A. E., McLaughlin, K., Nezhlin, N. P., Sutula, M., & Weisberg, S. B. (2019). Systematic Review and Meta-Analysis Toward Synthesis of Thresholds of Ocean Acidification Impacts on Calcifying Pteropods and Interactions With Warming. *Frontiers in Marine Science*, 6. <https://doi.org/10.3389/fmars.2019.00227>
- Bograd, S. J., Castro, C. G., Di Lorenzo, E., Palacios, D. M., Bailey, H., Gilly, W., & Chavez, F. P. (2008). Oxygen declines and the shoaling of the hypoxic boundary in the California Current. *Geophysical Research Letters*, 35(12). <https://doi.org/10.1029/2008GL034185>
- Chan, F., Barth, J. A., Blanchette, C. A., Byrne, R. H., Chavez, F., Cheriton, O., Feely, R. A., Friederich, G., Gaylord, B., Gouhier, T., Hacker, S., Hill, T., Hofmann, G., McManus, M. A., Menge, B. A., Nielsen, K. J., Russell, A., Sanford, E., Sevadjian, J., & Washburn, L. (2017). Persistent spatial structuring of coastal ocean acidification in the California Current System. *Scientific Reports*, 7(1), 2526. <https://doi.org/10.1038/s41598-017-02777-y>



- Cheresh, J., & Fiechter, J. (2020). Physical and Biogeochemical Drivers of Alongshore pH and Oxygen Variability in the California Current System. *Geophysical Research Letters*, 47(19), e2020GL089553. <https://doi.org/10.1029/2020GL089553>
- Collins, W. J., Bellouin, N., Doutriaux-Boucher, M., Gedney, N., Halloran, P., Hinton, T., Hughes, J., Jones, C. D., Joshi, M., Liddicoat, S., Martin, G., O'Connor, F., Rae, J., Senior, C., Sitch, S., Totterdell, I., Wiltshire, A., & Woodward, S. (2011). Development and evaluation of an Earth-System model – HadGEM2. *Geoscientific Model Development*, 4(4), 1051–1075. <https://doi.org/10.5194/gmd-4-1051-2011>
- Dufresne, J.-L., Foujols, M.-A., Denvil, S., Caubel, A., Marti, O., Aumont, O., Balkanski, Y., Bekki, S., Bellenger, H., Benshila, R., Bony, S., Bopp, L., Braconnot, P., Brockmann, P., Cadule, P., Cheruy, F., Codron, F., Cozic, A., Cugnet, D., ... Vuichard, N. (2013). Climate change projections using the IPSL-CM5 Earth System Model: From CMIP3 to CMIP5. *Climate Dynamics*, 40(9), 2123–2165. <https://doi.org/10.1007/s00382-012-1636-1>
- Dunne, J. P., John, J. G., Adcroft, A. J., Griffies, S. M., Hallberg, R. W., Shevliakova, E., Stouffer, R. J., Cooke, W., Dunne, K. A., Harrison, M. J., Krasting, J. P., Malyshev, S. L., Milly, P. C. D., Phillipps, P. J., Sentman, L. T., Samuels, B. L., Spelman, M. J., Winton, M., Wittenberg, A. T., & Zadeh, N. (2012). GFDL's ESM2 Global Coupled Climate–Carbon Earth System Models. Part I:

- Physical Formulation and Baseline Simulation Characteristics. *Journal of Climate*, 25(19), 6646–6665. <https://doi.org/10.1175/JCLI-D-11-00560.1>
- Feely, R. A., Sabine, C. L., Hernandez-Ayon, J. M., Ianson, D., & Hales, B. (2008). Evidence for Upwelling of Corrosive “Acidified” Water onto the Continental Shelf. *Science*, 320(5882), 1490. <https://doi.org/10.1126/science.1155676>
- Fiechter, J., Edwards, C. A., & Moore, A. M. (2018). Wind, Circulation, and Topographic Effects on Alongshore Phytoplankton Variability in the California Current. *Geophysical Research Letters*, 45(7), 3238–3245. <https://doi.org/10.1002/2017GL076839>
- Gruber, N., Hauri, C., Lachkar, Z., Loher, D., Frölicher, T. L., & Plattner, G.-K. (2012). Rapid Progression of Ocean Acidification in the California Current System. *Science*, 337(6091), 220–223. <https://doi.org/10.1126/science.1216773>
- Haidvogel, D. B., Arango, H., Budgell, W. P., Cornuelle, B. D., Curchitser, E., Di Lorenzo, E., Fennel, K., Geyer, W. R., Hermann, A. J., Lanerolle, L., Levin, J., McWilliams, J. C., Miller, A. J., Moore, A. M., Powell, T. M., Shchepetkin, A. F., Sherwood, C. R., Signell, R. P., Warner, J. C., & Wilkin, J. (2008). Ocean forecasting in terrain-following coordinates: Formulation and skill assessment of the Regional Ocean Modeling System. *Predicting Weather, Climate and Extreme Events*, 227(7), 3595–3624. <https://doi.org/10.1016/j.jcp.2007.06.016>

- Hauri, C., Gruber, N., McDonnell, A. M. P., & Vogt, M. (2013). The intensity, duration, and severity of low aragonite saturation state events on the California continental shelf. *Geophysical Research Letters*, *40*(13), 3424–3428. <https://doi.org/10.1002/grl.50618>
- HAURI, C., GRUBER, N., PLATTNER, G.-K., ALIN, S., FEELY, R. A., HALES, B., & WHEELER, P. A. (2009). OCEAN ACIDIFICATION IN THE CALIFORNIA CURRENT SYSTEM. *Oceanography*, *22*(4), 60–71.
- Hauri, C., Gruber, N., Vogt, M., Doney, S. C., Feely, R. A., Lachkar, Z., Leinweber, A., McDonnell, A. M. P., Munnich, M., & Plattner, G.-K. (2013). Spatiotemporal variability and long-term trends of ocean acidification in the California Current System. *Biogeosciences*, *10*(1), 193–216. <https://doi.org/10.5194/bg-10-193-2013>
- Howard, E. M., Penn, J. L., Frenzel, H., Seibel, B. A., Bianchi, D., Renault, L., Kessouri, F., Sutula, M. A., McWilliams, J. C., & Deutsch, C. (2020). Climate-driven aerobic habitat loss in the California Current System. *Science Advances*, *6*(20), eaay3188. <https://doi.org/10.1126/sciadv.aay3188>
- Kishi, M. J., Kashiwai, M., Ware, D. M., Megrey, B. A., Eslinger, D. L., Werner, F. E., Noguchi-Aita, M., Azumaya, T., Fujii, M., Hashimoto, S., Huang, D., Iizumi, H., Ishida, Y., Kang, S., Kantakov, G. A., Kim, H., Komatsu, K., Navrotsky, V. V., Smith, S. L., ... Zvalinsky, V. I. (2007). NEMURO—a lower trophic level model for the North Pacific marine ecosystem. *Special Issue on NEMURO (North Pacific Ecosystem Model for Understanding*

*Regional Oceanography*) and NEMURO.FISH (NEMURO for Including Saury and Herring), 202(1), 12–25.

<https://doi.org/10.1016/j.ecolmodel.2006.08.021>

- Kroeker, K. J., Kordas, R. L., Crim, R., Hendriks, I. E., Ramajo, L., Singh, G. S., Duarte, C. M., & Gattuso, J.-P. (2013). Impacts of ocean acidification on marine organisms: Quantifying sensitivities and interaction with warming. *Global Change Biology*, 19(6), 1884–1896. <https://doi.org/10.1111/gcb.12179>
- KUDELA, R. M., BANAS, N. S., BARTH, J. A., FRAME, E. R., JAY, D. A., LARGIER, J. L., LESSARD, E. J., PETERSON, T. D., & VANDER WOUDE, A. J. (2008). New Insights into the Controls and Mechanisms of Plankton Productivity in Coastal Upwelling Waters of the Northern California Current System. *Oceanography*, 21(4), 46–59. JSTOR.
- Pickett, M. H., & Paduan, J. D. (2003). Ekman transport and pumping in the California Current based on the U.S. Navy's high-resolution atmospheric model (COAMPS). *Journal of Geophysical Research: Oceans*, 108(C10). <https://doi.org/10.1029/2003JC001902>
- Schlunegger, S., Rodgers, K. B., Sarmiento, J. L., Frölicher, T. L., Dunne, J. P., Ishii, M., & Slater, R. (2019). Emergence of anthropogenic signals in the ocean carbon cycle. *Nature Climate Change*, 9(9), Article 9. <https://doi.org/10.1038/s41558-019-0553-2>
- Shchepetkin, A. F., & McWilliams, J. C. (2005). The regional oceanic modeling system (ROMS): A split-explicit, free-surface, topography-following-

coordinate oceanic model. *Ocean Modelling*, 9(4), 347–404.

<https://doi.org/10.1016/j.ocemod.2004.08.002>

Turk, D., Wang, H., Hu, X., Gledhill, D. K., Wang, Z. A., Jiang, L., & Cai, W.-J.

(2019). Time of Emergence of Surface Ocean Carbon Dioxide Trends in the

North American Coastal Margins in Support of Ocean Acidification

Observing System Design. *Frontiers in Marine Science*, 6.

<https://www.frontiersin.org/articles/10.3389/fmars.2019.00091>

## Chapter 4 - Development of an interactive web-based management tool for ocean acidification and hypoxia

Julia Cheresh and Jerome Fiechter

### 4.1 Introduction

From marine resource managers, scientists, and policy-makers to fishers and aquaculture growers, many communities are confronting the challenges posed by ocean acidification and hypoxia. Along the U.S. West Coast, ocean acidification and hypoxia are progressing rapidly, and many of these communities seek to know where the impacts of OAH will be most severe and when the effects will be felt by specific organisms or ecosystems in general. Traditional channels of communicating scientific findings — namely, peer-reviewed publications and conference proceedings — are often not accessible to the individuals and groups who are responsible for decision making in the face of a changing climate. Web-based tools can allow for the dissemination of scientific information in a user-friendly and cost-free format. Application of these tools range from displaying general scientific communication to providing real-time recommendations and serving as data repositories.

To address the gap between research and marine resource management, a web tool for OAH was developed based on an ensemble of dynamically downscaled regional climate projections. A draft of the tool was created and shared with OAH community members from various sectors including ocean observing, research, and management. The tool was then modified based on feedback from OAH community members to make it more relevant to real-world applications. This chapter describes

the implementation of the web tool, along with how feedback from OAH community members was incorporated into the tool's functionality and general lessons learned from the process of developing such product.

## 4.2 Methods

### 4.2.1 Technical Development

The web tool was developed in R as a Shiny App (Chang et al., 2023). All data processing and visualization was conducted using Ferret (<http://ferret.pmel.noaa.gov/Ferret/>). Images were pre-rendered such that no live calculations or plotting is done by the Shiny tool, making the user experience quick and streamlined. The choice to only include pre-rendered images does limit the interactivity of the tool, such that the user is not able to zoom in on a particular location or pick a specific year from which to display data, as examples. Since earth system model solutions, and hence downscaled climate projections, describe the evolution of free-running coupled ocean-atmosphere dynamics, they only reproduce known modes of variability (e.g., El Niño Southern Oscillation) in a statistical sense and should not be treated as actual forecasts for a specific year, but rather as representative of the long-term evolution of current and future climate variability under anthropogenic forcing. Therefore, the choice of pre-calculating model output products and limiting the interactivity of the tool provides a safeguard against a potential misinterpretation of the regional projections, while still providing the user

with far more information than would be available in a traditional peer-reviewed paper.

#### 4.2.2 OAH community engagement

A key component of the web-tool development was discussing the product with OAH community members and practitioners who may understand the needs of users or would be users of the tool themselves. The goal of this process was to increase the relevance of the tool to real-world needs in the management and monitoring space. Interested parties were identified with the help of Dr. Justine Kimball, who is the Senior Program Manager for climate change at the California Ocean Protection Council and possesses a broad knowledge of various agencies priorities and projects. The community engagement process reached seven individuals from the ocean observing, research, and management spaces. Organizations represented include the Central and Northern California Ocean Observing System (CeNCOOS), UC Davis Bodega Marine Labs, and the Channel Islands, Monterey Bay, Cordell Bank, and Greater Farallones National Marine Sanctuaries. Participants were shown a beta version of the tool and asked a series of questions about the general presentation of information, as well as about specific metrics and display choices.

#### 4.3 Tool description

The tool contains an informational home page, several interactive tabs, and a methods and data page. The following section describes each tab's function and



content. The home page is an informational tab explaining the general purpose of the tool, along with interpretation guidance. Fig. 4.1 shows a portion of the “Intro” tab, where a user can find information about how to interpret the analysis and display of a particular OAH property derived from the ensemble of downscaled projections.

Info
OAH Change
Thresholds
Sanctuaries
Methods and Data

## Welcome to the UCSC ocean acidification and hypoxia online tool!

### Overview

This interactive online tool was developed by researchers at the University of California, Santa Cruz to disseminate ocean acidification and hypoxia (OAH) projections for California coastal waters, based on regionally downscaled climate models at 1/30° resolution (~3 km). This tool allows users to visualize the future progression of OAH at spatial scales relevant to marine resource management, and for biologically-relevant pH, aragonite saturation state and oxygen thresholds.

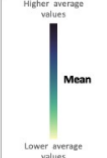
### How to use

—‘OAH change’ Tab: Explore maps and time series of pH, oxygen and aragonite saturation state. Select a variable, depth level, and 10-year time period of interest.

**Maps**

(Left) 10-year ensemble mean value  
(Right) Difference ( $\Delta$ ) between ensemble mean for 10-year projected period selected, and the historical 2000-2020 mean. Data is obscured by grey shading in locations where the model uncertainty (model spread) exceeds the magnitude of natural variability.


Higher average values



Mean

Lower average values

Smaller  $\Delta$  from historical conditions (2000-2020 avg.)



Difference


Larger  $\Delta$  from historical conditions (2000-2020)

**Time series**

Annual average value (black), ensemble spread of annual average values (blue shading), averaged 20km offshore from the first data point to shore.

**Ensemble spread**

Model predictions more similar to one another (higher confidence)



Model predictions less similar to one another (lower confidence)

Figure 4.1 Info tab. A portion of the “Info” tab, showing interpretation guidance for the “OAH Change” tab, such as what the color scales represent, how the data was averaged, and how to interpret ensemble spread.

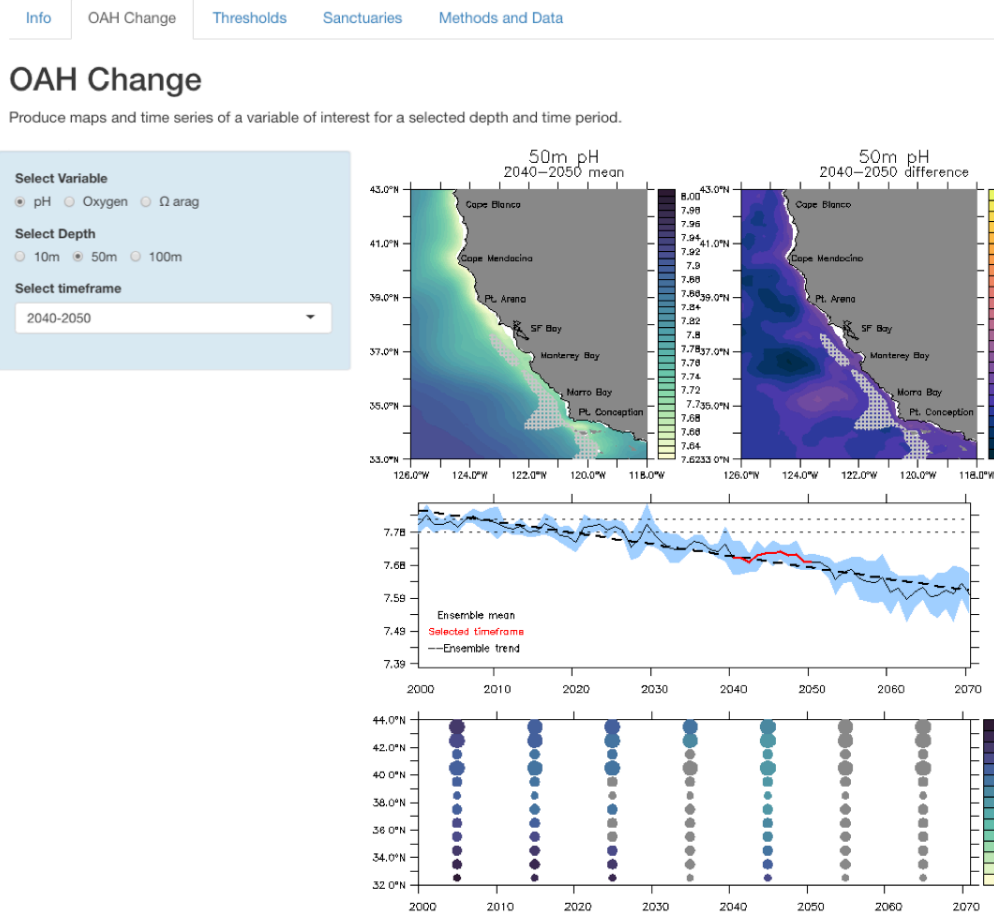


Figure 4.2 “OAH Change” tab.

The “OAH Change” tab (Fig. 4.2) allows users to visualize overall changes in pH, oxygen, and  $\Omega_{arag}$  over the entire model domain and throughout much of the 21<sup>st</sup> century. The user can select a variable, depth level (10m, 50m or 100m), and a 10-year timeframe. Two maps will appear, showing the mean value of the variable for the selected 10-year time period, and the difference between the mean for the selected 10-year time period and the historical (2000-2020) mean. Hashing is overlaid on the maps in locations where the model uncertainty exceeds the natural variability. Here,

“model uncertainty” corresponds to the ensemble spread defined as the standard deviation across the three mean values for the selected 10-year period from each projection, while “natural variability” represents the temporal standard deviation for the 10-year period combined across all three projections. A time series below the maps shows the ensemble mean for the chosen variable (solid black line) from 2000-2070, with the selected 10-year period highlighted in red. All values shown in the time series represent nearshore averages, which is defined here as a 0-20 km cross-shore average, with 0 representing the grid cell closest to shore with data (as this varies depending on depth). The shading around the ensemble mean denotes the ensemble spread and the thick dashed line represents the trend calculated from the ensemble mean. The thin horizontal dashed lines indicate the historical range of variability defined as the ensemble mean  $\pm$  one standard deviation based on 2000-2020 (i.e., the “historical” period). The final element of the “OAH Change” tab is a plot showing 10-year average values from the ensemble mean for 2000-2070 and binned by 1° of latitude. The color of the circle corresponds to the ensemble mean value, while the size of the circle corresponds to the magnitude of the trend at that latitude relative to other latitudes. This was quantified by computing trends at each latitude, which were then sorted into quartiles. Latitudes with trends in the upper quartile are plotted with a larger circle and indicate a stronger trend, Latitudes with trends in the lower quartile are plotted with a smaller circle and indicate a weaker trend. Latitudes in between are plotted with a medium circle. This display allows for comparison of values and trends across alongshore locations. Similar to the time

series, the values displayed in the bottom plot represent 0-20 km cross-shore averages. Grayed-out circles represent locations and decades for which the model uncertainty exceeds the natural variability.

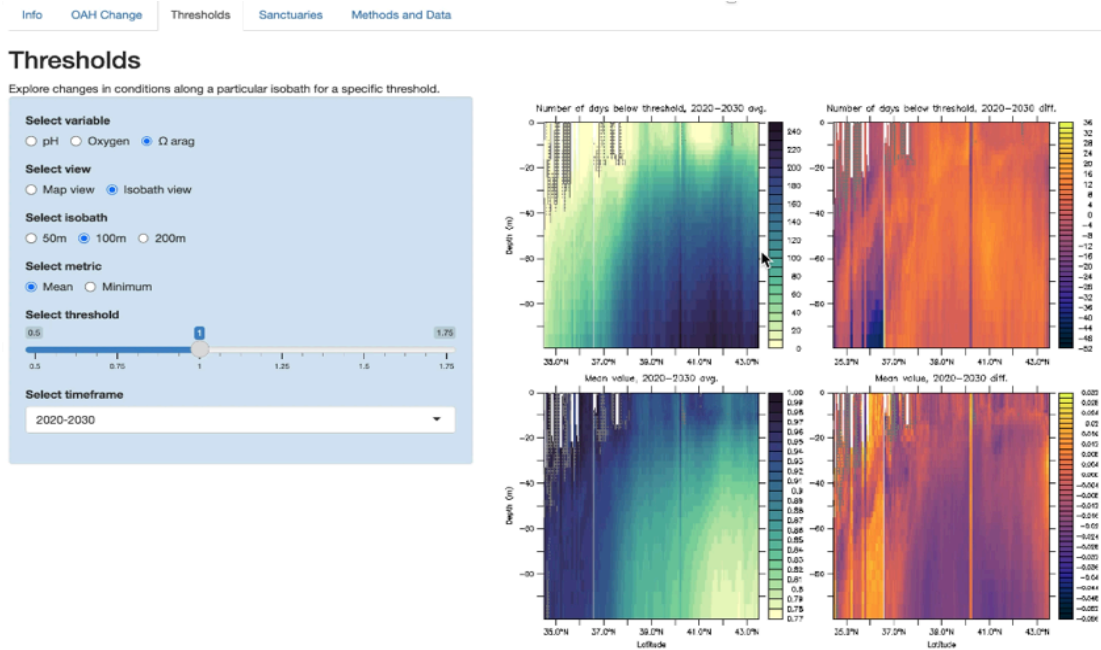


Figure 4.3 “Thresholds” tab in “isobath view”.

The “Thresholds” tab (Fig. 4.3) provides a different perspective on the data by allowing users to explore the projections based on specified thresholds for pH, oxygen, and  $\Omega_{arag}$ , if the user selects “isobath view.” After selecting an isobath and a time frame, latitude vs. depth plots will appear and show the average number of days per year during which conditions are below the selected threshold (top left), the difference between the average number of days per year below the selected threshold for the selected timeframe and the historical (2000-2020) average (top right), the mean value for the selected variable during days when conditions were below the

selected threshold (bottom left) and the difference between the mean values for the selected time period and the historical average (bottom right). White areas indicate that conditions did not drop below the specified threshold at that location and depth for the chosen decade. Gray hashing indicates latitudes and depths where model uncertainty exceeds natural variability.

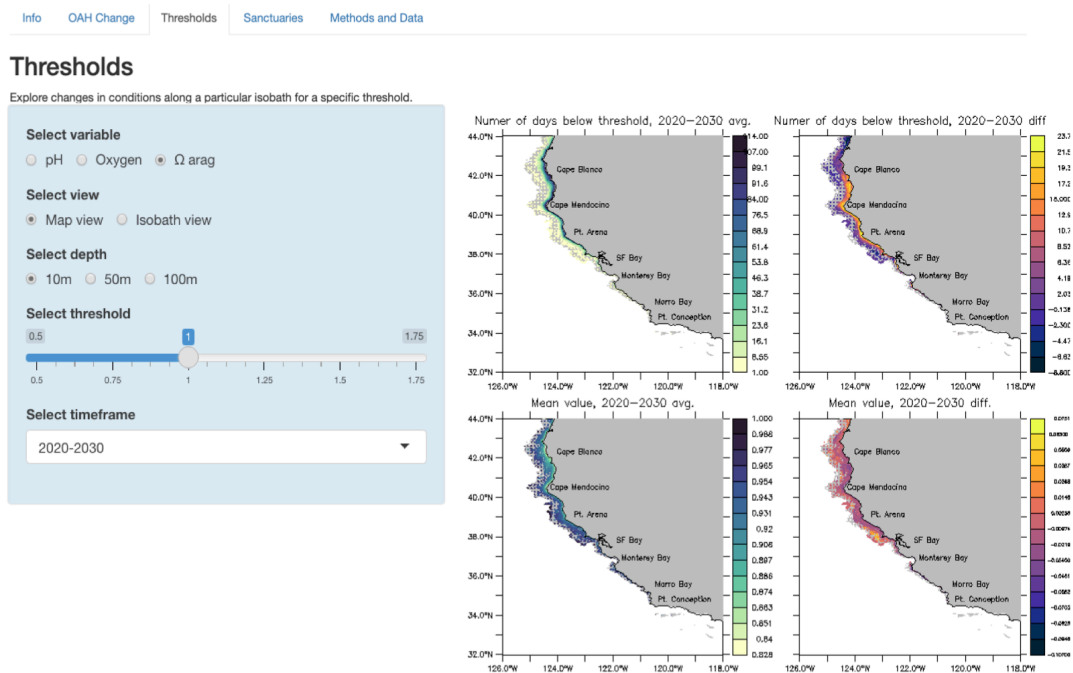


Figure 4.4 “Thresholds” tab in “map view”.

In “map view” (Fig. 4.4), users still select a variable, threshold, and decade, but can chose a depth instead of an isobath. The same metrics that are displayed in “isobath view” are available in “map view”, but plotted for a single depth as a function of longitude and latitude. Gray hashing indicates locations where model uncertainty exceeds natural variability.

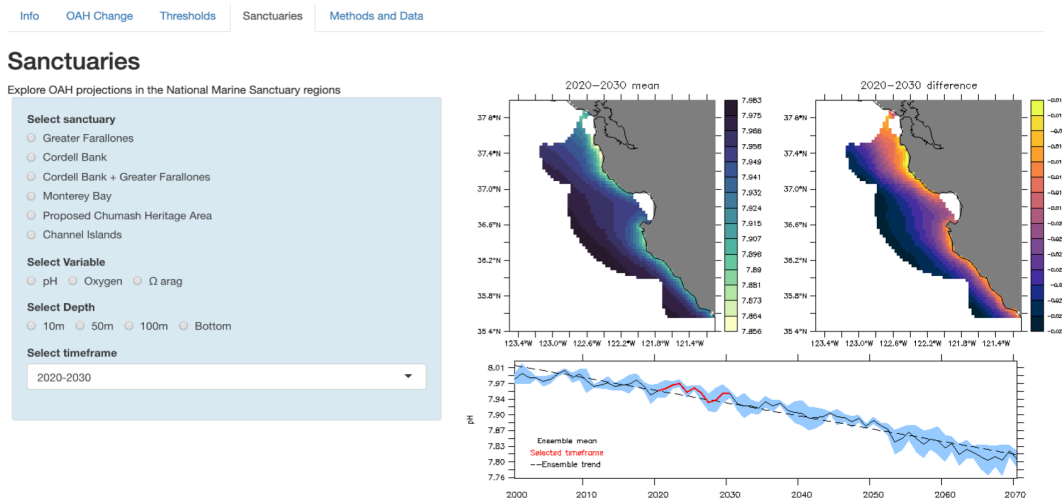


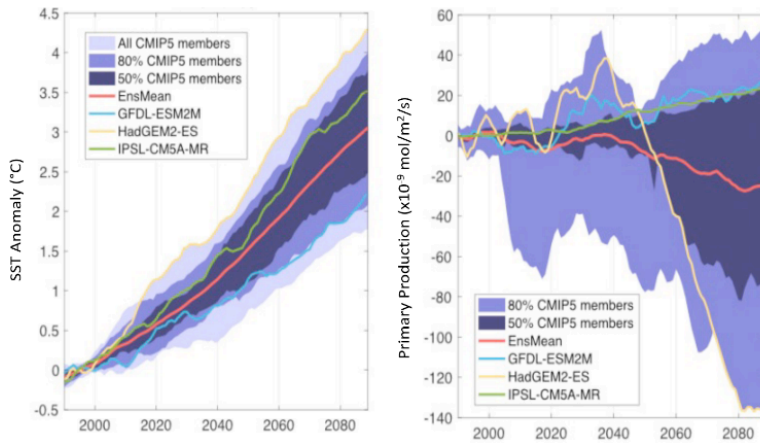
Figure 4.5 “Sanctuaries” tab.

The "Sanctuaries" tab (Fig. 4.5) allows users to explore the same metrics displayed in the “OAH Change” tab, but specifically calculated and display within the boundaries of California’s National Marine Sanctuaries. Two maps will appear, showing the mean value for the selected 10-year period, and the difference between the mean for the selected 10-year time period and the historical (2000-2020) mean. Hashing is overlaid on the maps in locations where the model uncertainty exceeds the natural variability. A time series below the maps shows the ensemble mean for the variable selected (solid black line) from 2000-2070, with the chosen decade highlighted in red. All values shown in the time series are spatially averaged within the boundaries of the sanctuary. is the shading around the ensemble mean represents the ensemble spread (defined here as the standard deviation of the three-member projections), and the thick dashed line denotes the trend calculated from the ensemble

mean. The thin horizontal dashed lines represent the historical range of variability, defined as the ensemble mean  $\pm$  one standard deviation for the 2000-2020 period.

### Regional Climate Projections

The downscaled regional projections were produced using three global earth system model solutions — GFDL-ESM2M, IPSL-CM5 and Hadley-GEM2-ES — run under the RCP 8.5 (business as usual) emissions scenario. These three GCMs were selected for their inclusion of marine biogeochemical fields, and to represent the spread of the CMIP5 ensemble mean (GFDL = low rate of warming; IPSL = rate of warming close to ensemble mean; Hadley = high rate of warming).



Pozo Bull. et al. 2021

The earth system model solutions were dynamically downscaled to 1/10° (~10 km) resolution for the broader California Current region, and further nested into a high-resolution domain for California to produce OAH projections at 1/30° resolution (~3 km).

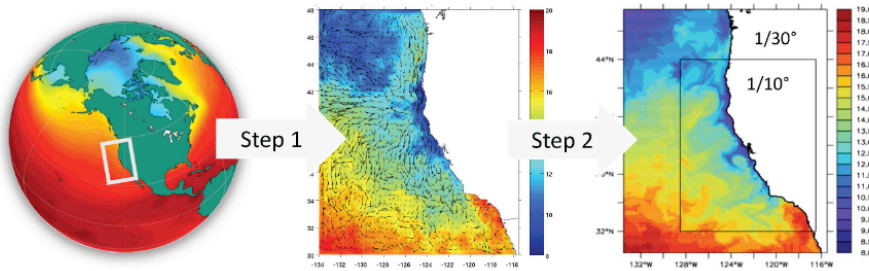


Figure 4.6 “Methods and data” tab. A portion of the methods and data tab, describing the Earth System Model selection and downscaling processes.

The Methods and Data tab includes information about the selection of earth system models and the downscaling process. Fig. 4.6 provides a snapshot of a portion

of this tab. Also included is a brief description of the physical-biogeochemical model nested within the downscaled regional projections.

#### 4.4 Incorporation of feedback from OAH community

The OAH community engagement process yielded valuable comments, some unique to each sector, but many overlapping across potential user groups. Figure 4.7 highlights key takeaways from the meetings. Significant changes to the web tool based on feedback include: (1) changing values from representing 20-year means to representing 10-year means, (2) standardizing plots and color palettes across tabs to improve ease of interpretation, (3) adding plots of the difference between the selected time period and the historical period, and (4) adding language and schematic to provide enhanced interpretation guidance. Some feedback applied to the web tool in general, and therefore two changes were changed in each tab:

- 1) Originally, the user could select from a list of 20-year time periods ranging from 2000-2100. Model uncertainty grows relative to natural variability towards the end of the century, and OAH community feedback suggested that showing low-confidence data is not useful. Therefore, the tool is now restricted to 2000-2070 and offers shorter 10-year periods from which the user can choose from.
- 2) OAH community members suggested adding language to explain jargon, and more interpretation guidance. Instead of overloading each tab with information, there is now dedicated space with language and schematic on the home page (“Info” tab).



Figures 4.8-4.10 and the text that follows illustrate specific changes made to each tab beyond the two outlined above.



Figure 4.7 Venn diagram summarizing feedback from OAH community. Comments provided by representatives from the management (green), observing (blue), and research (yellow) user groups.

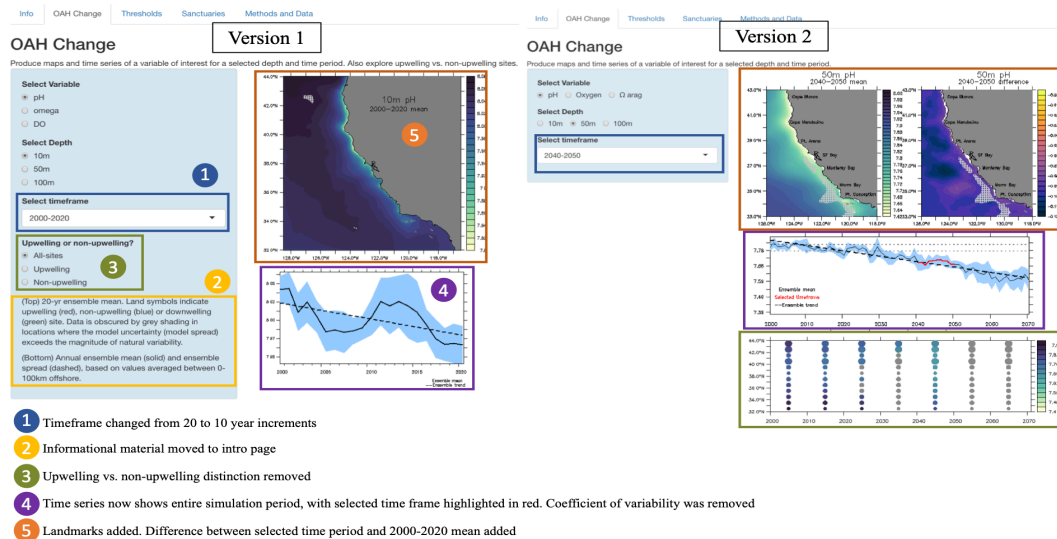


Figure 4.8 Changes made to “OAH Change” tab. (Left) Content of “OAH Change” tab prior to OAH community feedback (Version 1). (Right) Content of “OAH Change” tab post OAH community feedback (Version 2).

- 3) Originally, the time series on the “OAH Change” tab were averages either along the entire coast, within “upwelling regions” or within “non-upwelling regions”. Upwelling vs. non-upwelling regions were categorized based on correlations between temperature and pH. The goal was to provide an opportunity for comparison across alongshore locations. However, feedback suggested that upwelling vs. non-upwelling may not be intuitive or particularly useful. Therefore, this distinction is no longer displayed on the “OAH Change” tab and has been replaced with a plot showing 10-year mean values in 1° of latitude bins, with circle size providing information about the magnitude of the trend at that location relative to other alongshore sites.
- 4) A common theme across OAH community members was that showing future data is more valuable when it can be compared to historical baselines.

Therefore, time series now display data for 2000-2070, with the chosen decade highlighted in red, so that the user can more easily interpret the selected data within the context of the entire projection period. Furthermore, the historical range of variability (horizontal dashed lines) was added to contextualize the projected values.

5) In the same vein as item #4, a second map was added to display the difference between the mean from the selected time period and the mean from the historical (2000-2020) period. Landmarks were also added to the maps to help orient the user.

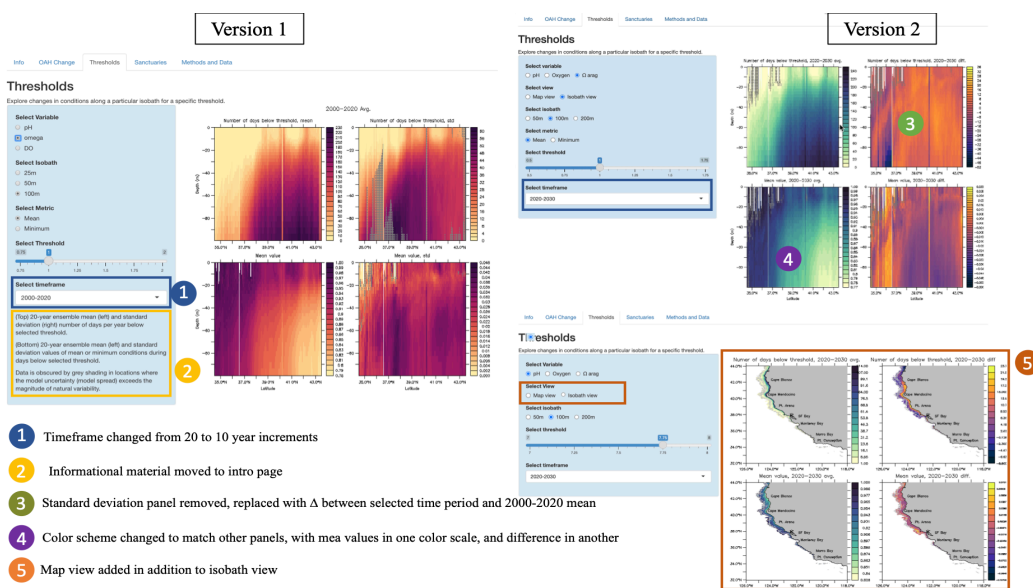


Figure 4.9 Changes made to "Thresholds" tab. (Left) Content of "Thresholds" tab prior to OAH community feedback (Version 1). (Right) Content of "Thresholds" tab post OAH community feedback (Version 2).

- 3) The original "Thresholds" tab displayed the average number and standard deviation of days per year during which conditions were below the selected threshold. Feedback suggested that the standard deviation may not be a particularly meaningful metric. Furthermore, it introduced a metric that was not present in the other tabs. Therefore, the standard deviation plots were replaced with the difference between the mean value for the selected decade and the mean historical (2000-2020) value. This provides continuity across the web tool tabs and contextualizes the data for the selected time period based on the historical values.
- 4) An additional change made to improve continuity across the tool was to maintain consistent color palettes across tabs. Now, plots of mean values are all in the same color palette across tabs, and plots of the difference from the historical period are all in the same color palette across tabs. This way, the user can orient themselves to the first tab, and apply the same understanding throughout the tool.
- 5) OAH community members pointed out that looking at latitude vs. depth plots may be confusing or difficult to interpret for some users. Furthermore, the concept of an isobath may not be intuitive to all users. However, it was also brought up that the isobath view could be quite useful for users in the research space. Therefore, the isobath view was kept, but an additional "map view" option was added. The same metrics are displayed in both view modes, but in one the user selects an isobath to display the data in latitude vs. depth space,

while in the other the user selects a depth to display the data in longitude vs. latitude space.

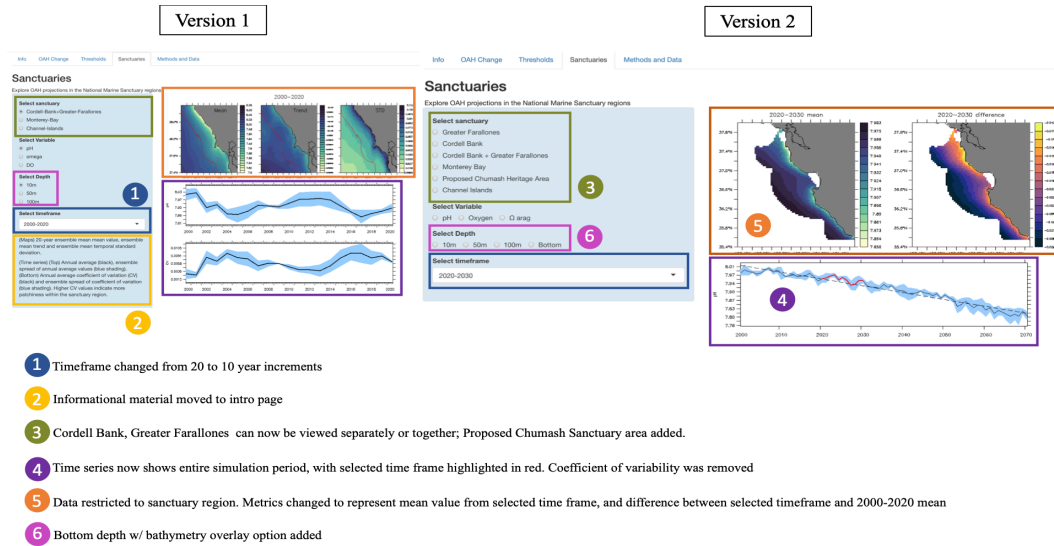


Figure 4.10 Changes made to “Sanctuaries” tab. (Left) Content of “Sanctuaries” tab prior to OAH community feedback (Version 1). (Right) Content of “Sanctuaries” tab post OAH community feedback (Version 2).

- 3) The National Marine Sanctuaries representatives suggested that allowing the user to view the Cordell Bank and Greater Farallones regions separately and together would be useful because some management decisions are made for the sanctuaries independently, while others are made for the two combined. The proposed Chumash Heritage Sanctuary was also added, but because the boundaries have not yet been determined, the tool only displays the general proposed region.
- 4) A common theme across meetings with OAH community members was that showing future data is more valuable when it can be compared to historical

baselines. Therefore, time series now display data from 2000-2070, with the chosen decade highlighted in red, so that the user can more easily interpret the selected data within the context of the entire projection period. Furthermore, the historical range of variability (horizontal dashed lines) was added to contextualize the projected values.

- 5) The data is now restricted to the sanctuary boundaries, and the time series represent averages from within these boundaries.
- 6) National Marine Sanctuary representatives brought up that providing bottom data would be useful for the management of benthic species, particularly because this is a data-poor region. A bottom depth option was added, with bathymetry overlaid.

#### 4.4 Lessons learned

The OAH community engagement process undoubtedly led to a more useful and streamlined product, but it also offered important lessons in designing scientific communication tools and conveying information about future change. The main thematic take-aways from the process include:

- 1) Identify and refine the targeted audience early on in the process. The model output contains a wealth of information and it is tempting to show as much as possible to meet the needs of every interested party. However, it became clear through this process that it is a better use of time to make a tool that is highly

suitable and applicable to one targeted audience, than to build an overly-complicated tool that may not serve the needs of any particular group.

- 2) Think about continuity across the tool. Orienting the user to one particular style of presenting data and then carrying that style throughout the tool will allow for more successful communication and usability, rather than the user consistently having to re-orient to new ways of displaying information.
- 3) Future change should be compared to a historical baseline. Future values are useful, but not necessarily meaningful without an understanding of the historical mean or range of variability. This is particularly important in an upwelling region like the California Current System, where natural variability plays an important role in characterizing the progression of anthropogenic change.

#### 4.5 References

Chang W, Cheng J, Allaire J, Sievert C, Schloerke B, Xie Y, Allen J, McPherson J, Dipert A, Borges B (2023). *shiny: Web Application Framework for R*.  
<https://shiny.posit.co/>, <https://github.com/rstudio/shiny>.

## Conclusion

Prior to the completion of the research summarized in the present dissertation, the body of knowledge surrounding the drivers of alongshore and interannual variability in exposure to corrosive and oxygen-poor conditions in the central California Current System was relatively limited. A synoptic survey in 2007 documented an alongshore pattern in exposure to corrosive conditions on the shelf along the US west coast, which was connected to variability in the strength of upwelling (Feely et al. 2008). However, this synoptic survey took place over the course of two months, meaning that the documented spatial pattern likely represents the effect of multiple upwelling events. Furthermore, it was debatable whether this pattern was representative of the long-term mean conditions, as it includes data from a single upwelling season. Data from nearshore stationary time series along the US West Coast indicated that exposure to low pH conditions is episodic in nature, with events lasting from days to weeks (Chan et al., 2018). This temporal variability in exposure was related to upwelling-favorable wind events followed by periods of relaxation. However, the results presented in Chan et al., 2018 only included data from 2013, leaving unanswered questions about the interannual variability of these events. This dissertation aimed to fill gaps regarding the physical and biogeochemical processes shaping alongshore and interannual variability in historical and future ocean acidification and hypoxia by employing high-resolution coupled physical-biogeochemical simulations.



Chapter 1 provided the first comprehensive, mechanistic characterization of the physical and biogeochemical processes shaping the long-term alongshore exposure to low pH and oxygen conditions in the central California Current System. The results identify an alongshore succession of minima and maxima in pH and oxygen conditions, resulting from a complex interplay between upwelling intensity and primary production, modulated by the alongshore and cross-shore regional circulation. Chapter 2 details the biophysical drivers of interannual variability in corrosive events at the depth of upwelled source waters. The results demonstrate that interannual variability in the severity of exposure to corrosive conditions is driven by combination of high-frequency (interannual) changes in upwelling intensity and low-frequency (decadal) modulation of the dissolved inorganic carbon (DIC) content of upwelled source waters. Together, Chapters 1 and 2 provide a historical baseline of the physical and biogeochemical processes shaping the alongshore and interannual patterns of exposure to corrosive and low-oxygen conditions. Chapter 3 builds on this work by employing downscaled regional climate projections to characterize where and when hot spots and refugia for pH and oxygen will emerge. The results suggest that where and when hot spots and refugia for pH and oxygen emerge depends on the metrics used to quantify them. If one is managing for OAH and cares about where and when conditions become distinct from their historical range ( $ToE_{clim}$ ), projected hot spots correspond with areas of historically weak upwelling due to their lower interannual variability. If one is managing for OAH and cares about where and when conditions will drop below specific biological thresholds ( $ToE_{thresh}$ ), projected hot

spots are located in places with historically strong upwelling due to their lower pH and oxygen baseline values. Chapter 4 documents the development and functionality of an online interactive management tool, where users can engage with the projections based on their region or species of interest.

As a whole, the four chapters of this dissertation provide a mechanistic description of the physical and biogeochemical drivers of alongshore and interannual variability in current and future exposure to reduced pH and oxygen conditions, while disseminating this information to marine resource managers in an accessible and interactive format. The results highlight the complexity of characterizing change in a dynamic coastal upwelling system, and stress the need to consider and account for multiple different spatial and temporal scales when describing the drivers of natural variability and anthropogenic change in the nearshore California Current System.

Further avenues of research based on the findings presented here could include investigation of the differences between downscaled climate projections; for example, why does GFDL, with the lowest rate of warming as compared to the other ensemble members, have the most dramatic declines in pH through the end of the century? It would also be useful to understand if the patterns and drivers of alongshore variability in pH and oxygen will change in the coming decades. This would have biologically-important consequences, as changes in the magnitude of variability may differentially impact populations adapted to their local environment. Lastly, it would be interesting to investigate how future changes in basin-scale

variability will impact upwelled source water properties, and in turn, how this may affect the severity of exposure in the nearshore environment.